A new generation experiment for the study of strongly interacting Fermi gases

Shuwei Jin

PSL UNIVERSITÉ PARIS

THÈSE DE DOCTORAT
DE L'UNIVERSITÉ PSL

Préparée à l'École Normale Supérieure

A New Generation Experiment for the Study of Strongly Interacting Fermi Gases

Une Expérience de Nouvelle Génération pour l'Étude des Gaz de Fermi en Interaction Forte

Soutenue par

Shuwei JIN

Le 19 décembre 2019

Ecole doctorale n° 564

Physique en Île-de-France

Spécialité

Physique Quantique

Composition du jury:

Prof. Dr. Stefan Kuhr	***Président***
University of Strathclyde (Glasgow)	*Rapporteur*
Dr. Giacomo Roati	
LENS (Florence)	*Rapporteur*
Prof. Dr. Bruno Laburthe-Tolra	
Université Paris XIII (Paris)	*Examinateur*
Dr. Leticia TARRUELL	
ICFO (Barcelona)	*Examinatrice*
Dr. Christophe SALOMON	
Laboratoire Kastler Brossel (Paris)	*Directeur de thèse*
Dr. Tarik YEFSAH	
Laboratoire Kastler Brossel (Paris)	*Membre invité*

ENS ÉCOLE NORMALE SUPÉRIEURE 1794 PSL RESEARCH UNIVERSITY PARIS

Département de Physique **Laboratoire Kastler Brossel**

École Normale Supérieure

Thèse de Doctorat de l'École Normale Supérieure

Spécialité : Physique Quantique

présentée par

Shuwei Jin

pour obtenir le grade de docteur de l'École Normale Supérieure

---

A New Generation Experiment for the Study of Strongly Interacting Fermi Gases

Une Expérience de Nouvelle Génération pour l'Étude de Gaz de Fermi en Interaction Forte

---

Soutenue le 19 Décembre 2019
devant le jury composé de :

M. Stefan Kuhr	. . . . .	Rapporteur
M. Giacomo Roati	. . . . .	Rapporteur
M. Bruno Laburthe-Tolra	. . . . .	Examinateur
Mme. Leticia Tarruell	. . . . .	Examinatrice
M. Christophe Salomon	. . . . .	Directeur de thèse
M. Tarik Yefsah	. . . . .	Membre invité

Contents

Chapter 1

Introduction

1.1 Context

Strongly-correlated fermions are ubiquitous in nature, from the quark-gluon plasma of the early universe to neutron stars, they lie as well at the heart of many modern materials such as high-temperature superconductors and giant magneto-resistance devices [1, 2]. While being a pressing issue covering a wide range of fundamental and technological scopes, the understanding of strongly-correlated fermions constitutes an ongoing challenge of modern physics. Solid-state materials can host a vast variety of strongly correlated states of matter but their intrinsic complexity renders an experimental interpretation difficult. The contribution of ultracold gases experiments [3] in this outstanding quest resides in the ability to set fermions in a well-characterized environment, where one can add a single ingredient at a time (spin mixture, interactions, lattice, etc.) with a high degree of control, allowing for an incremental complexity, which represents an ideal playground for a direct comparison to many-body theories. A prominent example, where ultracold Fermi gases were shown to be useful testbeds, is found in the recent measurements of the equation of state of the unitary Fermi gas [4, 5].

The system of interest here is a two-component Fermi gas with tunable interactions, where two hyperfine states can be mapped onto the Zeeman projection of a spin-1/2 particle. The inter-particle interactions are characterized by a single length scale, the scattering length a. We stress that such simple description of interactions is not for convenience[(a)] - as used to be the case for helium systems, for instance - but reflects the actual behavior of the system in our experiments with high accuracy. Indeed, due to the extreme diluteness and low temperature of the gas, collisions only occur at short-distance and in an isotropical manner. Formally, one refers to those as s-wave contact interactions, which is the generic case in quantum gas experiments where the atomic species or molecules under study do not feature a significant permanent magnetic moment or induced electric moment. A direct consequence of this type of interactions for Fermi gases is the fact that they can only occur between a spin $\uparrow$ and spin $\downarrow$, collisions between atoms of identical spins being forbidden by Pauli's exclusion principle [6].

By means of a Feshbach resonance [7, 8], we can experimentally tune the strength and sign of the scattering length a. Formally, when $1/a$ is tuned from "$-\infty$" to "$+\infty$", the system evolves

[(a)] Even though the benefit for comparison to many-body theories is obvious.

from a Fermi gas with attractive interactions to a gas of tightly bound bosonic molecules[(b)]. At sufficiently low temperature, the former limiting case corresponds to the celebrated Bardeen-Cooper-Schrieffer (BCS) superfluid[(c)] state [9, 10], where a Fermi sea is altered by a fraction of long-range weakly attractive Cooper pairs. In the latter limiting case, the assembly of molecules would form a Bose-Einstein Condensate (BEC). In fact, a remarkable property of this system is that, at sufficiently low temperature, the system is superfluid not only in these two limiting cases but also for any (non-zero) interaction strength, hence the name of "BEC-BCS crossover". The observation of this crossover in the early 2000 was only possible with the advent of ultracold Fermi gases [3], which allowed to confirm for the first time a 20 year old prediction [11, 12].

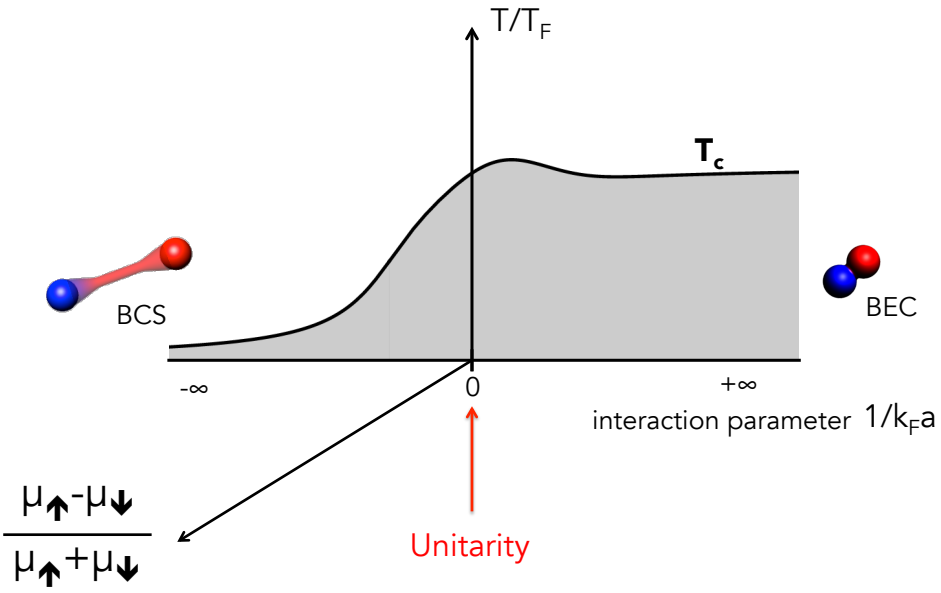

Figure 1.1: Spin–1/2 system with tunable interactions and spin imbalance. At sufficiently low temperature the system is superfluid throughout the crossover. The unitary point, where the scattering length a diverges, corresponds to a regime of strong correlations and represents one of the biggest challenges of many-body physics [13].

Besides the fact that they can be continuously connected, the two limiting cases discussed above are not of high interest from the many-body perspective, as they are both in a well understood mean-field regime. Instead, in between, as we move away from the two $a \to 0$

[(b)]Note that a more natural way to picture this transformation is to think in terms of interaction potential. The interaction potential is always negative (despite the change in the sign of a). From the two-body perspective, this picture is incomplete as the binding energy is only non-zero on the $a > 0$ side and reaches zero when $1/a \to 0^+$. However, taking into account the many-body effects, the binding energy always remains finite and approaches asymptotically to zero when $1/a \to -\infty$. Hence, when $1/a$ is tuned from "$-\infty$" to "$+\infty$", the attractive potential continuously evolves from shallow to deep. A $\uparrow + \downarrow$ pair therefore evolves from weakly to deeply bound. On the other hand, the description in terms of the scattering length a renders the singularity at the unitary point more evident as $1/a = 0$.

[(c)]The constituents being electrically neutral in our case.

limits, the system's behavior tends to be more and more dominated by interactions. A natural measure of this degree of correlation is the interaction parameter $1/k_{\mathrm{F}}a$, which compares the the inter-particle spacing $\sim 1/k_{\mathrm{F}}$ (k_{F}, being the Fermi wavevector) to the scattering length. It is also equivalent (within a power of 2) to compare the Fermi energy $\hbar^2 k_{\mathrm{F}}^2/2m$ to the effective binding energy $\hbar^2/(2ma^2)$. The regime where $|k_{\mathrm{F}}a| \geq 1$ is referred to as the strongly-correlated regime and has been the subject of intense theoretical and experimental efforts over past two decades [13].

1.1.1 The unitary Fermi gas

In the strongly-correlated regime, the point where $1/k_{\mathrm{F}}a = 0$ is referred to as the unitary limit[(d)] and plays a special role. On this point lies the Feshbach resonance, where the scattering length diverges $a \to \infty$. There, as the interactions do not introduce any explicit length scale anymore, the only length scales are the $1/k_{\mathrm{F}}$ and the de Broglie wavelength λ_{dB}. Or, in terms of energy scales, we are only left with the Fermi energy E_{F} and the thermal energy $k_{\mathrm{B}}T$. This fact has crucial implications and leaves a door open to understand the unitary Fermi gas, which is notoriously difficult to tackle theoretically.

This advantage becomes evident when it comes to investigating the ground-state energy of a unitary Fermi gas. For example, a simple dimensional analysis shows that the ground state energy of a unitary Fermi gas E^0_{Unitary} is proportional to the energy of the non-interacting Fermi gas E^0_{Free}:

$$E^0_{\mathrm{Unitary}} = \xi_{\mathrm{B}} \cdot E^0_{\mathrm{Free}},$$

where ξ_{B} is a universal constant called the Bertsch parameter, in honor of the G. Bertsch who first identified that the challenge of calculating E^0_{Unitary} is only reduced to determining ξ_{B} [14, 15].

The ground-state results can be generalized to finite temperature:

$$E_{\mathrm{Unitary}} = \xi_{\mathrm{B}} \cdot E_{\mathrm{Free}} \cdot f\left(\frac{T}{T_{\mathrm{F}}}\right),$$

where f is now a universal *function* of dimensionless ratio T/T_{F} (where $T_{\mathrm{F}} = E_{\mathrm{F}}/k_{\mathrm{B}}$ is the Fermi temperature). In fact, the existence of only two energy scales implies that any thermodynamic quantity has to be a universal function of the ratio T/T_{F} .

The universal character of the unitary Fermi gas will not only reflect on the thermodynamics, but also dynamical properties [16] and microscopic properties [17, 18], which we do not discuss here in detail. However, we want to stress that this property renders the unitary gas of interest from a very broad perspective. Indeed, the universality of the unitary Fermi gas means that any two-spin fermionic matter, independent of its size, density, temperature range or constituents, is governed by the same equations as long as the interactions with the particles are s-wave,

[(d)] This name has a somewhat indirect origin. While this point corresponds to the diverging scattering length, formally there is a bound set by quantum mechanics on the modulus of the scattering amplitude $f(k)$. Applying the optical theorem to the problem describing the scattering of two opposite-spin fermions via s-wave interactions - so that $f(k)$ depends only on the modulus of the relative momentum k - one can show that $|f(k)| \leq 1/k$. The optical theorem, being a consequence of the unitarity of the quantum evolution operator, this limit is called the unitary limit.

short-range and "infinite". For instance, the knowledge that we can acquire in our laboratory at the nK range is relevant for neutron stars in the outer-space where the temperature is on the order of 10^9 K [19].

Figure 1.2: Neutron Star. False color radiation emission from Pulsar PSR B1509-58 [20]. The inner crust composed of neutrons can be described as a unitary Fermi gas. Temperature is in the order of $T = 10^9$ K and densities of $n = 10^{38}$ at/cm^3, corresponding to a $T_\mathrm{F} = 10^{11}$ K. Despite several order of magnitude in absolute temperature and density, the ratio $T/T_\mathrm{F} = 0.01$ is on the same order of values reached in our lab.

1.1.2 Spin-imbalanced Fermi gases

Besides the tunabilty of interactions and temperature, ultracold Fermi gas experiments also offer the ability to vary the spin population imbalance. This knob should not be seen as a practicality but a unique opportunity to understand the behavior of strongly interacting fermionic matter. In fact, the question of the behavior of spin-imbalanced Fermi gases was raised only a few years after BCS theory. In 1962, Chandrasekhar [21] and Clogston [22] addressed this issue in the context of superconductors. More precisely, the question was to determine whether the superconducting state could survive the presence of a magnetic field, as the magnetic field tends to align spins in the same direction while pairing occurs between opposite spins. They found that the superconducting state breaks down above a critical magnetic field h_c - corresponding to a critical spin-imbalance P_c. This "Clogston-Chandrasekhar limit" marks the point where pairing breaks down in favor of a normal state. In 1964, Fulde and Ferell [23], as well as Larkin and Ovchinnikov [24] investigated the possibility of an inhomogeneous phase featuring a spatially modulated superfluid fraction. Their findings show that before turning into a normal state, the superconductor can host a certain amount of excess spins, trapped in the nodes of a spatially oscillating order parameter that can be either standing (FF) or traveling (LO). This exotic superconducting phase is referred to as the FFLO phase and has not been observed since its prediction.

Interestingly, for decades the question of superfluidity and spin-imbalance was essentially an academic question as the Meissner effect [25] expels magnetic fields from the bulk of a superconductor, preventing the experimental study of the effect. However, about 15 years ago, spin-imbalanced exotic superconductors were discovered [26]. Other realization of spin-imbalanced Fermi gases are found in nuclei and possibly the core of neutron stars where quark superfluids with unequal quark populations are expected to exist. The experimental

investigation of these systems nevertheless comes with a number of difficulties, and is often faced with limited probing capabilities and the absence of tunability.

With the advent of ultracold Fermi gases, where the spin-imbalance can be varied at will by simply picking the population of (hyperfine) spin states, a whole avenue for experimental studies opened up.

1.2 State of the art in short

Since the achievement of the first degenerate Fermi gas in 1999 [27], the studies on ultracold Fermi gases have produced a great number of results, ranging from the experimental realization of the BEC-BCS crossover [13] to the observation of Mott-insulating [28–31] and anti-ferromagnetic states [30, 32] of the Hubbard model. In the following we provide a short overview of the research carried out on the BEC-BCS crossover in 3D.

1.2.1 Qualitative results

Between 1999 and 2001, the collisional properties of ideal Fermi gases were studied. In 2002, several groups managed to optically confine a two-component mixture in the vicinity of a Feshbach resonance [33–36]. The tunability of interactions led to the observation of hydrodynamic behavior [37, 38] and the creation of Feshbach molecules [39–41]. Shortly afterwards, BCS fermion pair condensates were observed [42].

A number of studies on this new crossover superfluid were performed, in terms of thermodynamic measurements [38, 43], collective excitations [44, 45], and RF spectroscopy [46]. However, all of these early studies on the BEC-BCS crossover were only consistent with superfluid behavior but did not unambiguously demonstrate it. Finally, in 2005, phase coherence and fermionic superfluidity were adequately demonstrated through the excitation and observation of quantized vortices and vortex lattices [47]. More recently, the experimental realization of a Josephson junction of Fermions have demonstrated the phase coherence of a fermionic superfluid across the whole BEC-BCS crossover region [48].

1.2.2 Quantitative results

In the recent past years, several groups have demonstrated that thermodynamic observables can be precisely measured within the local density approximation [4, 5, 49]. These types of measurements rely on a well characterized inhomogeneous trapping potential and an accurately determined density. These techniques have led to the measurement of the ground-state equation of state (EoS) of the two component Fermi gas in the whole BEC-BCS crossover [4, 50] (Fig. 1.3). At finite temperature, the equation of state has only been measured for the spin-balanced unitary gas. The measurement of the critical temperature across the BEC-BCS crossover remains an open challenge.

Beyond the investigation of thermodynamic quantities, the measurement of correlations has also been initiated. In the BEC-BCS crossover context, only short range density-density correlations, characterized by the contact C [17, 18, 51], have been investigated. Various techniques

have been employed to quantitatively determine C, including RF spectroscopy [52–54], Bragg spectroscopy [55, 56] and three-body losses [57]. The advent of quantum gas microscopy has opened up the possibility to probe correlation functions. While there is a considerable amount of results on correlations in Hubbard lattice models, bulk gases have never been explored under a quantum gas microscope.

1.3 Objectives of the new experiment

The extensive studies carried on BEC-BCS Fermi gases over the past ten years have significantly improved our understanding of strongly interacting Fermi gases. However, as we have seen previously, very little is known about the correlation functions or the nature of these correlations. Furthermore, it is also unclear how these correlations build up upon crossing the superfluid transition and what the corresponding critical exponents are.

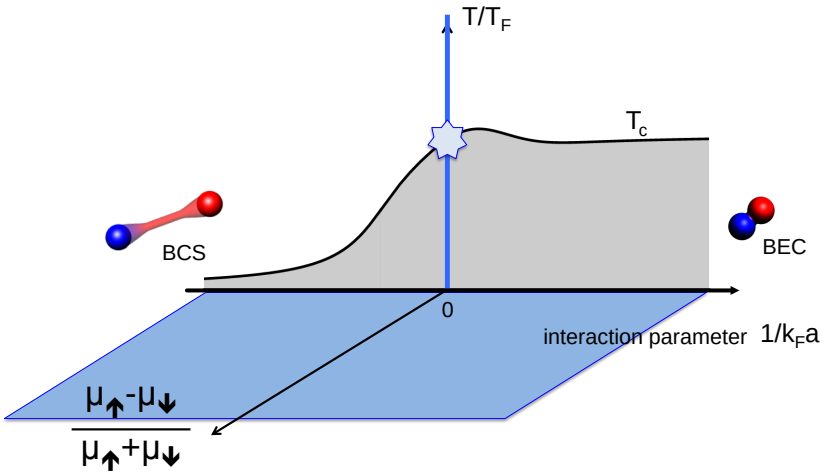

Figure 1.3: Phase diagram of a two-component Fermi gas versus the interaction strength ($1/k_{\mathrm{F}}a$), the spin imbalance and the temperature. The EoS has been measured in the ground state [50] (blue-shaded plane) and at finite temperature for the spin-balanced unitary Fermi gas [4, 5] (blue solid line). This leaves large parts of the phase diagram uncharted.

Many open questions also remain even concerning our knowledge of the phase diagram (Fig. 1.3). For example, the critical temperature has only been measured at unitarity, while the rest of the BEC-BCS crossover remains uncharted territory. Moreover, past experiments have devoted a large part of their efforts to probing and understanding ultracold Fermi gases in the deep superfluid regime, well below the critical temperature T_{c}. However, the state of matter in the critical region (around T_{c}) remains poorly understood, and is subject to a vivid debate [13].

Our new generation experiment aims at pursuing the effort towards answering these questions. For that purpose we will use cutting edge techniques, such as quantum gas microscopy [58–64] and tailored potentials [65–68], in order to provide a microscopic and highly quantitative perspective on strongly-interacting Fermi gases.

So far, most experiments performed with ultracold Fermi gases used inhomogeneous traps, typically harmonic potentials. While such potentials were proven to be extremely useful and

well suited for some thermodynamic studies, they constitute at the same time the main obstacle to quantitatively accessing other crucial observables. Indeed, as a consequence of the trap inhomogeneity, any probe addressing the whole cloud yields a trap-averaged, biased, response. For instance, radiofrequency-photon spectroscopy, typically used to obtain the single-particle excitation spectrum of a Fermi gas, leads to a blurred response in the case of a harmonically trapped sample, and instead, benefits significantly from the use of a homogeneous potential [67].

The use of tailored optical potentials [65–68] will be combined with single atom detection in a quantum gas microscope, which has been under rapid development in the last ten years. Quantum gas microscopes relies on fluorescence imaging and require long-interrogation times in which the atoms should not move. The atomic motion is inhibited by the use of deep optical lattices that pin or freeze atoms to the potential wells. This technique can yield impressive signal-to-noise ratios, with near unity fidelity. Since the first realization of single atom resolved imaging [58, 59], this technique has enabled numerous studies of phase transition [58, 59], correlations [69–71], spin-interactions [72], quantum magnetism [73], long-range interactions using Rydberg atoms [74–76] and entanglement [77, 78]. Since the more recent realizations of fermionic quantum gas microscopes [60–64], this powerful technique has provided an excellent way of studying fermionic many body systems [32, 79–85]. While quantum gas microscopes have only been used so far to probe the physics of fermions in a lattice, we propose in our setup to extend the scope of this technique to the study of a *bulk* gas of strongly-interacting fermions. By probing the atom distribution at the single atom and single spin level, we will be able to access directly density and spin correlations, from the scale of neighboring atoms to the size of the whole sample. This opens truly fascinating perspectives, from the direct observation of the build-up of correlations near the superfluid phase transition in various interaction regimes, to the possibility of revealing unambiguously the long sought after FFLO state, where it exists.

Thesis outline

This thesis describes the design and characterization of a second generation quantum gas experiment dedicated for the study of strongly interacting Fermi gases. It includes 6 additional chapters:

- Chapter 2 describes the experimental setup. The various subsystems, including the vacuum manifold, the 671 nm laser setup to laser cool ^{6}Li atoms and the magnetic field generation are presented.
- Chapter 3 presents the results of laser cooling on ^{6}Li, in particular the characterization of the MOT and the performance of the D_1 gray molasses.
- Chapter 4 focuses on the description, characterization and performance of the high power infrared laser setup, and operation of the experiment near the Feshbach resonance. In particular, we characterize the optical transport, the radio-frequency transfer, as well as the evaporative cooling in the science cell.

- Chapter 5 describes the creation and characterization of a degenerate Fermi gas produced in the strongly interacting regime. We are able to precisely characterize the degree of degeneracy of our Fermi gas using measurements on the equation-of-state and we present also proof of superfluidity of our gas.
- Chapter 6 presents the design of the setup dedicated to the imaging of ^{6}Li clouds at the single atom level.
- Chapter 7 summarizes the work and gives the perspective on future developments of the experiment.

Chapter 2

Experiment overview

The main part of this PhD work is dedicated to the design and setup of a new experiment for studying strongly interacting Fermi gases, which poses many technical challenges. In this chapter we first present some relevant properties of ^{6}Li. Then we describe the experiment hardware, in particular the vacuum manifold, and the laser system to laser cool ^{6}Li and the magnetic field generation to address the Feshbach resonance of ^{6}Li. The high power laser setup for the evaporative cooling of ^{6}Li is presented in more detail in chapter 4.

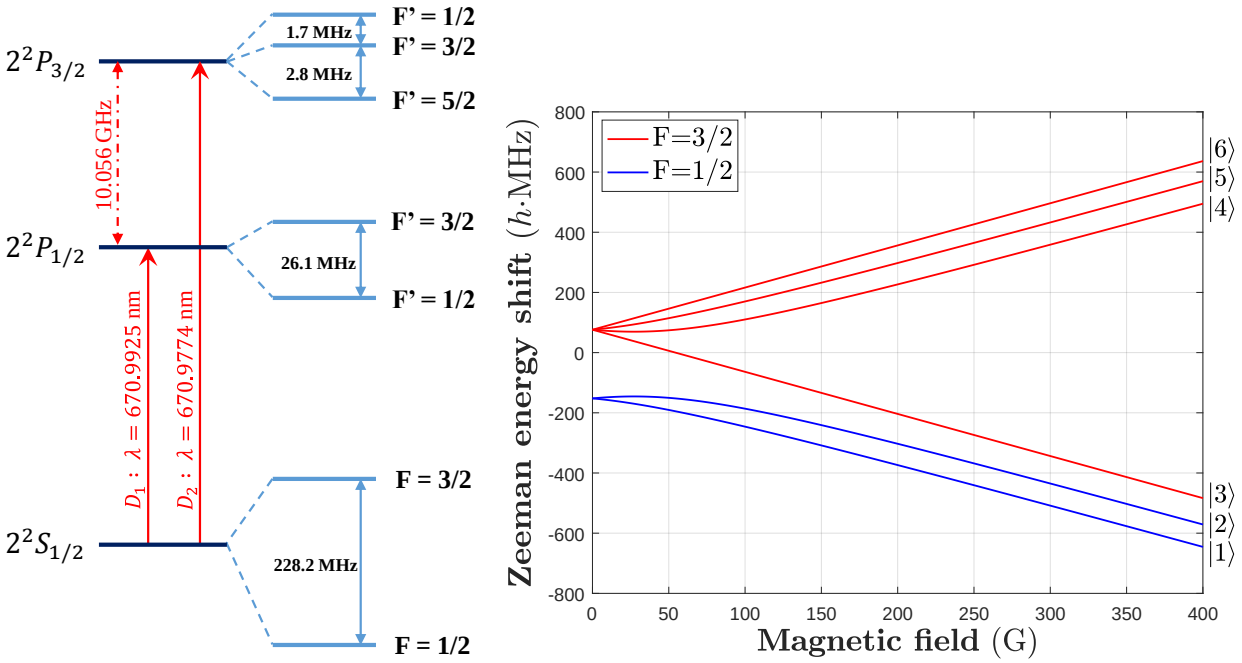

Figure 2.1: Left: The D_1 and D_2 transitions of ^{6}Li. Right: Zeeman energy shift of the ground states $2^2S_{1/2}$.

2.1 Atomic source: Properties of ^{6}Li

Here we briefly recall some basic properties of ^{6}Li. In particular, we mention the relevant optical transitions (D_1 and D_2) for laser cooling and the Feshbach resonances between the three lowest

high field seeking energy states. For more details on the properties of ^{6}Li the reader can refer to [86].

2.1.1 Level structure of ^{6}Li

An overview of the relevant optical transitions is shown in Fig. 2.1. The D_1 and D_2 transitions at 671 nm have a natural linewidth of $\Gamma = 2\pi \times 5.87\,\mathrm{MHz}$ and have a difference in frequency of approximately 10 GHz only [86].

The ground state hyperfine energy splitting of ^{6}Li is only $E_{\mathrm{HFS}} = h \cdot 228.205\,\mathrm{MHz}$ at zero magnetic field, which is small compared to the other alkali elements. This means that for relatively small magnetic field, ^{6}Li enters the Paschen-Back regime already. In the right graph of Fig. 2.1, we show the Zeeman splitting of ^{6}Li calculated using the Breit-Rabi formula. We see that the energy differences between the high field seeking (resp. low field seeking) Zeeman sublevels become already comparable to the hyperfine splitting for a magnetic field of ∼200 G.

We also notice the hyperfine splitting of the excited levels is very small. For $2^2P_{3/2}$ the hyperfine splitting is only a few MHz, which is less than the linewidth of D_2 transition. This prevents the standard sub-Doppler cooling of ^{6}Li with the MOT beams. The gray molasses cooling on D_1 transition hence is introduced to cool down the atoms further.

2.1.2 Feshbach resonance of ^{6}Li

^{6}Li possesses broad Feshbach resonances. Each pair of the high-field seeking states possesses one resonance with a width of several hundreds of gauss (Fig. 2.2). For conventional reasons, the Zeeman states counting from the lowest energy level to the highest energy levels are noted as $|1\rangle$, $|2\rangle$, ..., $|6\rangle$. In our experiments, we only use the mixture of states $|1\rangle$ and $|2\rangle$. The center of the Feshbach resonance for $|1\rangle$ and $|2\rangle$ lies at 832 G and it has a width of approximately 300 G.

2.2 Vacuum manifold

The ultrahigh vacuum manifold provides the environment where the experiment takes place. Its design is based on and closely related to the cooling techniques and the goal of the experiment, which is to achieve a high resolution single atom imaging apparatus.

An overview of the experiment is shown in Fig. 2.3. We can find the standard elements of an cold atom eperiment of ^{6}Li, more specifically:

- the oven (1) heated to ∼500 °C to ensure a sufficient Lithium vapor pressure,
- the shutter (2) that allows to block the atomic jet,
- the differential pumping section (3) that isolates the high pressure in the oven section to ensure a low pressure in the rest of the experiment,
- the Zeeman slower (4) to slow down the atomic jet,
- the main chamber (5) to achieve a MOT and to perform gray molasses cooling,

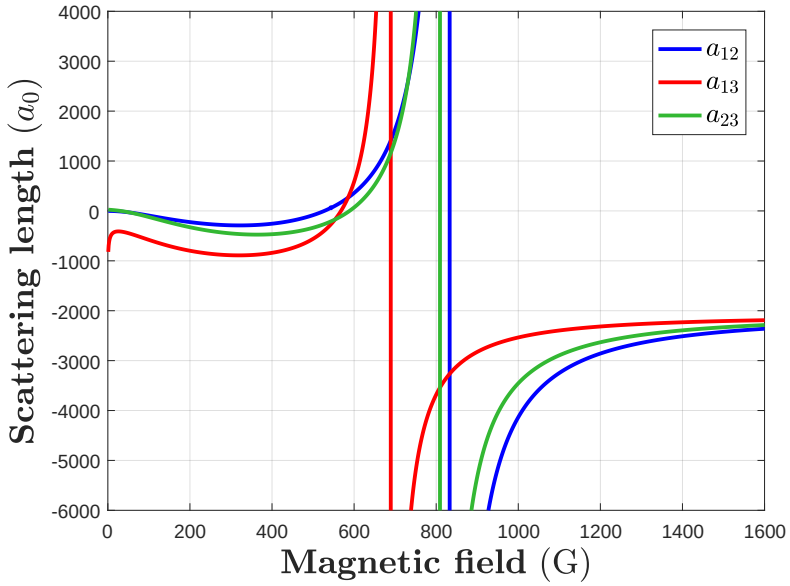

Figure 2.2: The Feshbach resonances between the three low-field seeking spin states of ^{6}Li: $|1\rangle$, $|2\rangle$ and $|3\rangle$.

- the science cell (9) where we transport the atoms to perform further evaporative cooling and achieve degeneracy.

2.2.1 Main components of the vacuum system

Lithium oven

The oven is a small container which we fill with lithium samples. We have filled the oven with approximately 1 g of natural Lithium and 1 g of enriched pure ^{6}Li. Since the natural abundance of ^{6}Li is only 7.5%, we thus have approximately equal amount of ^{6}Li and ^{7}Li in the oven.

The structure of the oven has one particular perk. The horizontal tube as shown in Fig. 2.4 has an inner diameter of 5 mm and a length of 7.5 cm. We fill the oven from the top and this horizontal tube not only collimates the atom jet but also serves as a first differential pumping tube.

During operation, we heat up this tube to higher temperatures than the bottom to avoid clogging the tube. We also inserted a sheet of metallic grid inside this tube to facilitate the recycling of lithium [87].

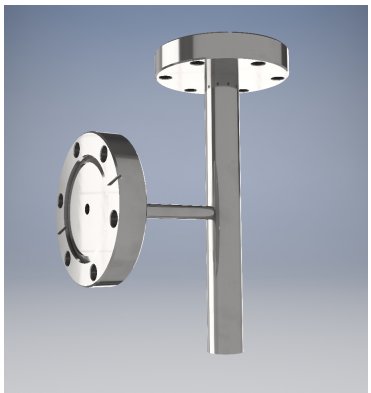

Figure 2.4: Li oven.

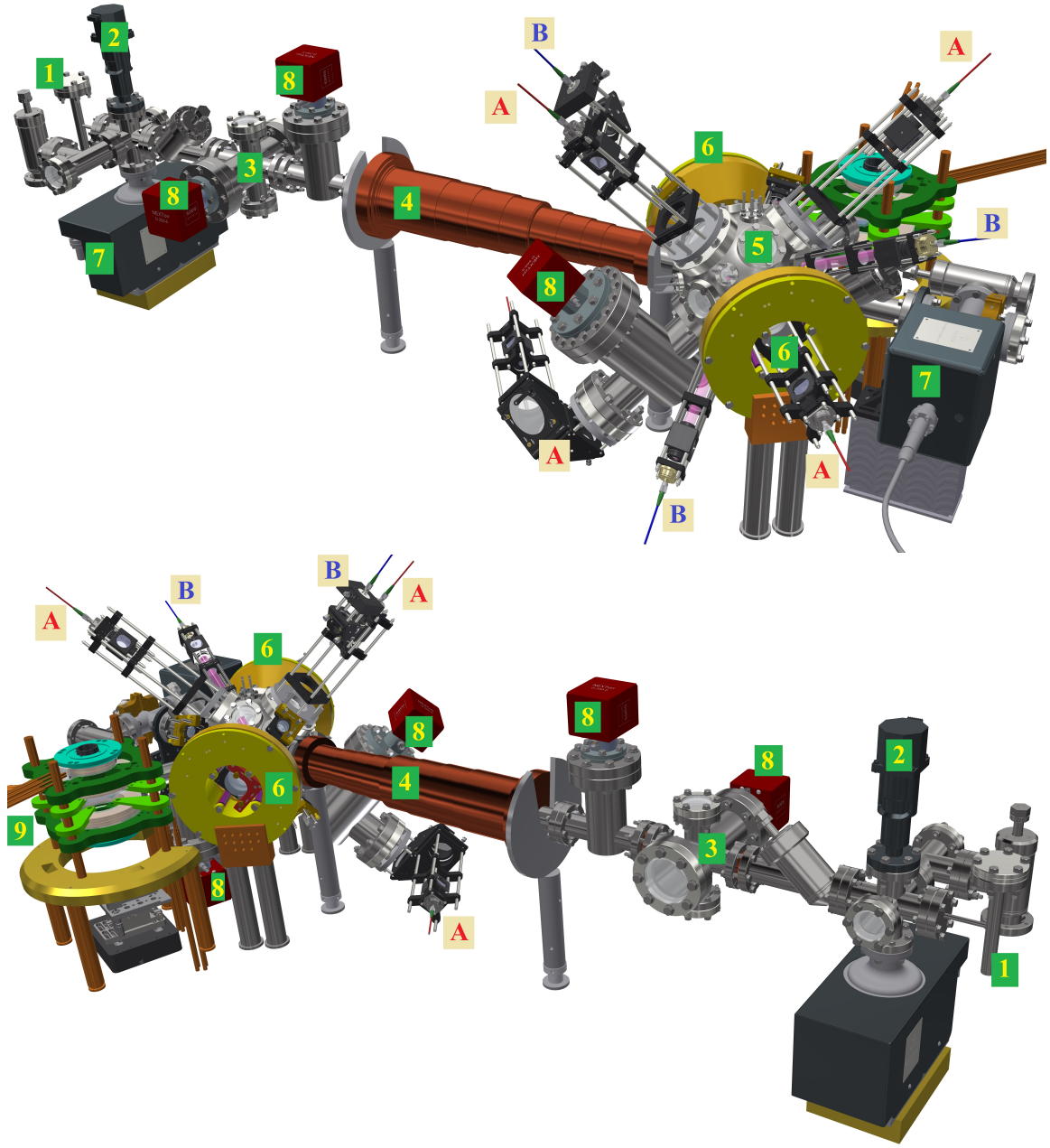

Figure 2.3: Overview of the experiment: 1) lithium oven. 2) atomic beam blocker. 3) differential pumping section. 4) Zeeman slower. 5) main chamber. 6) MOT coils. 7) ion pumps. 8) SAES getter pumps. 9) science cell section with Feshbach & curvature coils around. A) MOT beams. B) gray molasses beams.

Differential pumping

Lithium has a very low vapor pressure at room temperature, which requires heating to typically around 500 °C to achieve an atomic jet with large atomic flux [86]. At this temperature the oven not only generates an atomic jet with strong flux but also outgases non-desired elements like nitrogen or hydrogen, which increases the background gas pressure and decreases the cold atoms gas lifetime. For typical operational temperatures of the Lithium oven, the pressure inside the oven can be as high as 10^{-4} Torr, which is way too high for the required vacuum pressure for the experiment, typically 10^{-11} Torr.

One way to solve this issue is to isolate the oven part (high-vacuum part) of the experiment from the rest of the experiment (ultrahigh-vacuum part) where we trap the cold atoms, by introducing differential pumping tubes. They are simply metal tubes having a small diameter of several millimeters inserted between two flanges. According to the actual pumping capacities on both sides of the differential pumping tube, vacuum pressure can be reduced up to two or three orders of magnitude from one side to the other.

In our experiment, the dimensions of the tubes are based on the calculation and design in [88]. The collimation tube of the oven serves as a first vacuum differential pumping tube, with a length of 7.5 cm and an inner diameter of 5 mm. The second differential tube has a length of 10 cm and an inner diameter of 5 mm. The third one has the same length of 10 cm, but a larger inner diameter of 10 mm.

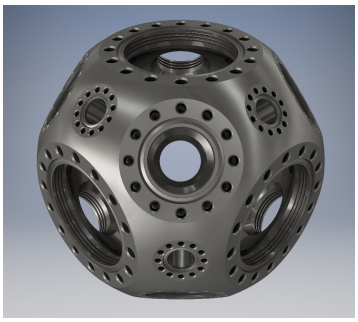

Figure 2.5: Main chamber.

We have in total two ion pumps: one with 40 L/s pumping speed[(a)] close to the oven and another 20 L/s[(b)] close to the Zeeman window. The main pumping capacity of the experiment, however, is assured by four ion-getter pumps. They have inside a stack of Getter materials installed to absorb the residual gas, in particular hydrogen, in the system. These pumps have significantly higher pumping capacities than the conventional ion pumps. In our experiment, we installed three Getter pumps of 200 L/s[(c)] and one of 500 L/s[(d)] installed close to the main chamber.

With the aforementioned pumping capacities, the evaluated pressure inside the science cell, when the pressure inside the oven is $\sim 1 \times 10^{-4}$ Torr, is seven orders of magnitude lower, i.e. $\sim 1 \times 10^{-11}$ Torr.

Main chamber

The main chamber is the place where we implement the laser cooling. We have chosen a spherical cube[(e)] (Fig. 2.5) because it has a large number of viewports and hence guaranties

[(a)] Agilent Technologies VacIon Plus StarCell 40
[(b)] Agilent Technologies VacIon Plus StarCell 20
[(c)] NexTorr D 200-5
[(d)] NexTorr D 500-5
[(e)] Kimball Physics MCF450-SphCube-E6C8A12

a good optical access. In total it possesses 6 CF63 viewports, 8 CF40 viewports and 12 CF16 viewports.

The MOT beams are sent through the CF63 viewports. The Zeeman slower is connected to the CF40 flanges and the gray molasses light are sent through the CF16 viewports. The imaging in the main chamber can be performed through CF40 viewports in three independent directions.

Science cell

The science cell in our experiment is a ColdQuanta glass cell made of Shott Borofloat 33, AR-coated for 671 nm and 1064 nm, with a wall thickness of 3 mm. The inner dimension of the cell is $20\times20\times60\,\mathrm{mm}^3$. The material Borofloat is a relatively new material available on the market. Compared to the standard materials like fused silica, Borofloat is easier to be AR-coated and can be joined at low temperature. Fused silica, on the contrary, can be joined only at high temperature that is susceptible to damage the AR-coatings. For this reason, most glass cells in fused silica have AR-coatings applied only on the exterior surfaces, once only after the cell is assembled. Glass walls of Borofloat, in comparison, can be first AR-coated on both sides and then joint at low temperature.

The disadvantage of Borofloat is the higher likelihood to show thermal effect when exposed to high power lasers. Systematic data for Borofloat is still difficult to come by. But thermal lensing effect on Borofloat cell with 5 mm wall thickness has been observed [89].

2.2.2 Assembly and baking

In order to achieve the low pressure, it is necessary to bake the vacuum system upon assembly.

Once the vacuum system is assembled, we use two turbo pumps connected to both sides of the main experiment and start pumping. We wrap heating tapes around the whole experiment to heat up to 180 °C gradually in several hours. One must take special care to the vacuum viewports while increasing the heating temperature and have to make sure the heating rate does not exceed the specification[(f)]. Once the pressure drops below 10^{-7} Torr, we switched on the ion pumps. We have kept the experiment continuously in 180 °C during one month. At the very end of this pumping, the pressure reduced to 10^{-9} Torr at 180 °C. At this time, the heating of the whole vacuum system is stopped and the Getter pumps are activated. In the end, the final pressure provided by the Getter ion pumps' current is below nano Ampere, which corresponds to a pressure scale of less than 10^{-12} Torr.

There are several elements in the experiment that require supplementary baking in addition to the aforementioned standard baking procedure.

To start with, the Zeeman slower tube needs to be baked before winding. We baked at 380 °C and evacuated to pressure as low as 5×10^{-8} Torr before decreasing the temperature. Once the Zeeman slower is wound and assembled, we use the first layer of heating wires, as we will see more in detail in the following, to bake at 180 °C together with the rest of the vacuum system.

[(f)] Typically less than 2 °C per minute.

The oven also needs to be baked prior to integration into the main vacuum system. After the oven is filled with lithium, we connect it directly to a turbo pump and a vacuum gauge using nickel gaskets and heat up to 600 °C. We use nickel gaskets since lithium is corrosive at high temperature so that standard copper gasket would develop leaks. We bake the oven at relatively high temperatures, between 600 °C and 700 °C, since the operating temperature of the oven is typically 400 °C to 500 °C. For the oven baking the pressure decreased to 10^{-7} Torr at 600 °C at the end.

The last part that requires special attention is the differential pumping tubes. Since they are fabricated in the machine shop, they are first cleaned with ultrasonic bath and then carefully wiped with acetone. Then they are enclosed in a container of stainless steel and baked at 600 °C. And we stopped baking at a similar pressure as for the oven baking, i.e. 10^{-7} Torr before taking them out.

2.3 Laser cooling setup overview

Laser cooling is the first step of a cold atom experiment. Frequency stabilized lasers need to be applied at different instants to address given optical transitions in order to trap and cool atoms.

One of the disadvantages of Lithium is that the conventional laser diodes lack power at the relevant transition wavelength (671 nm). Many developments have been made for designing a solid state lasers [90, 91] at this wavelength, being able to deliver power of more than 1 Watt, but commercial choices capable of this power level are still limited. For our experiments, we opt for the diode lasers from Toptica and TA chips from Eagleyard to perform the laser cooling and the detection of ^{6}Li.

On the one hand, there are laser beams that require much power for laser cooling, such as the Zeeman slowing beam, the MOT beams and the gray molasses beams. More specifically, the operation of a MOT requires the intensity of each MOT beam to be on the order of several I_{sat}, whereas the operation of a gray molasses requires each beam to be around $10\, I_{\mathrm{sat}}$ [92]. Here $I_{\mathrm{sat}} = 2.54\,\mathrm{mW/cm^2}$ is the saturation intensity of D_2 transition[(g)]. For these beams, we use hence tapered amplifier chips to amplify the power.

On the other hand, laser beams for optical pumping and detection require much less power. For example, absorption imaging requires that the imaging beams have intensities such that $I/I_{\mathrm{sat}} < 0.1$. Optical pumping also requires intensity on the same order of magnitude. For the detection and optical pumping at zero magnetic field, we derive light directly, using AOMs, from the same master laser for the laser cooling on the D_2 line. For detection at high field around 832 G where lies the Feshbach resonance, we use an independent laser DL Pro having an output of 25 mW, and we implement an offset lock of approximately 1.2 GHz with the D_2 master laser [93]. A schematic of the 671 nm laser setup is shown in Fig. 2.6.

[(g)]Note that for conventional reasons, although the gray molasses for ^{6}Li is operated on D_1 transition, people use the saturation intensity of D_2 to indicate the intensity of the molasses beams.

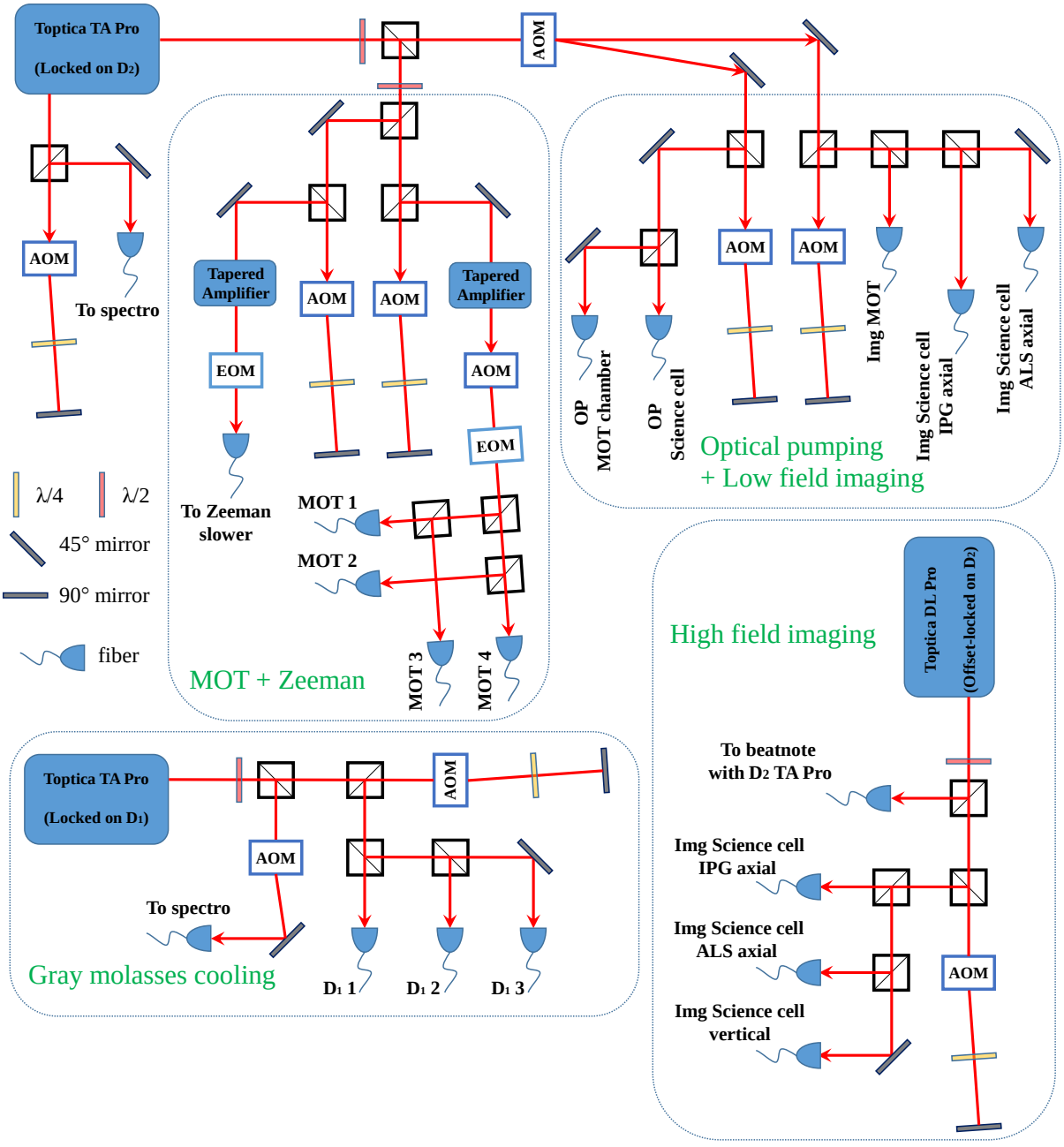

Figure 2.6: Simplified schematic of the laser setup at 671 nm for laser cooling, optical pumping and detection.

2.3.1 ^{6}Li spectroscopy

The laser frequencies need to be stabilized using spectroscopic signals. We send laser light through a spectroscopy cell, which consists of a long tube of ∼40 cm with CF40 flange ends. Lithium atoms are in the center region, which we heat up to 300 °C to ensure a sufficient high lithium vapor pressure. However, should the lithium vapor reach the vacuum viewports at the two ends, it can coat the viewports through deposition. To avoid that, we introduced Argon in the cell as buffer gas on the one hand, and installed water-cooling pipes at the two extremities of the spectroscopy cell on the other hand.

The optical setup around the spectroscopy cell is shown in Fig. 2.7. We use the modulation transfer spectroscopy technique [94], which has two advantages over the standard saturation spectroscopy. Firstly, the error signal generated in this case does not contain an offset depending on the intensity of the beam. Secondly, the absence of a linear background absorption leads to a lower sensitivity to beam intensity and cell temperature.

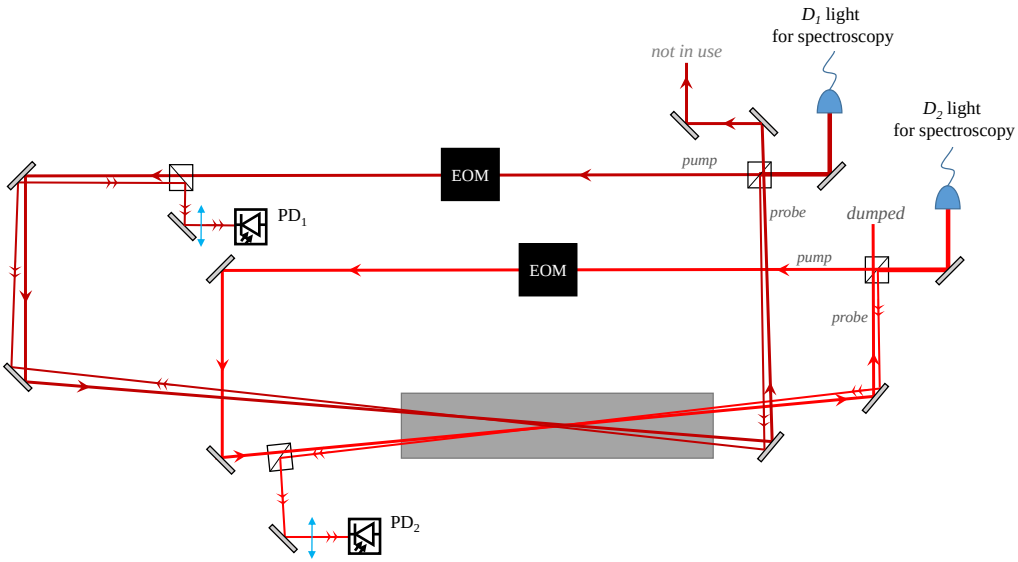

Figure 2.7: The laser set-up for the spectroscopy. The two laser setups go through the same spectroscopy cell.

The D_1 and the D_2 lights are sent through the same spectroscopy cell. The EOMs used for modulating the pump beams are modulated at 17 MHz using the PDD110 modules from Toptica.

For the D_2 laser we lock on the transition $F = 3/2 \rightarrow F'$. And for the D_1 laser we lock on the crossover between the transitions $F = 3/2 \rightarrow F'$ and $F = 1/2 \rightarrow F'$. The linewidth of the locked laser, after being locked, is typically sub-MHz, which is sufficiently stable for implementing laser cooling.

2.3.2 Zeeman slower

The Zeeman slower [95] is one of the ways to decelerate the atomic jet from several hundreds of m/s to several tens of m/s. Simply speaking, it creates a spatially dependent magnetic field

to compensate the Doppler effect of the atoms due to deceleration. The optimal profile of the magnetic field of a Zeeman slower is a parabola.

There are in total three different kinds of Zeeman slowers according to their magnetic field profiles: increasing field Zeeman slower, decreasing field Zeeman slower and spin flip Zeeman slower. The increasing (resp. decreasing) field Zeeman slower is such that the magnetic field increases (resp. decreases) in amplitude as a function of the distance in the direction of the atomic jet. A spin-flip Zeeman slower is such that the magnetic field crosses zero and changes sign at a certain point along the trajectory of the atoms. All these three types have their advantages and disadvantages. For increasing/decreasing field Zeeman slower, since the magnetic field does not change the sign along the trajectory, only one cooling beam frequency is needed. Whereas for the spin-flip Zeeman slower, as its name rightfully indicates, the atoms can eventually fall to the wrong Zeeman sublevels while crossing the magnetic field zero, hence the necessity of a repumping frequency in addition to the cooling frequency. However, a spin-flip Zeeman slower consume less electrical power than its other two counterparts, since the magnetic field changes sign and hence results in less driving current overall.

Zeeman slower field The Zeeman slower in our experiment is a spin-flip Zeeman slower. It has a length of 60 cm, wound with in total 24 layers of copper wires of different lengths to create a appropriate magnetic field.

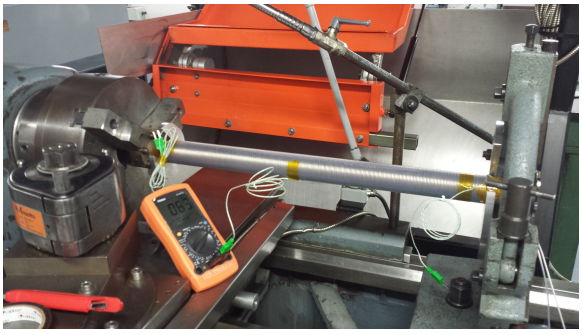

(a) First layer of heating tape.

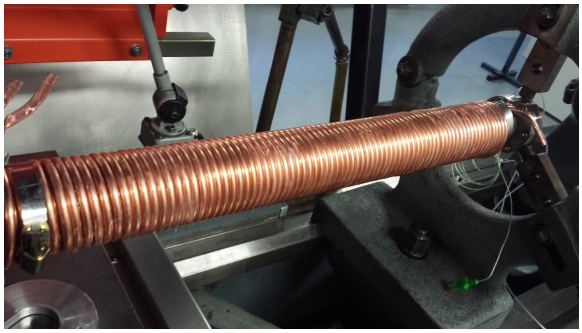

(b) Two layers of cooling tubes.

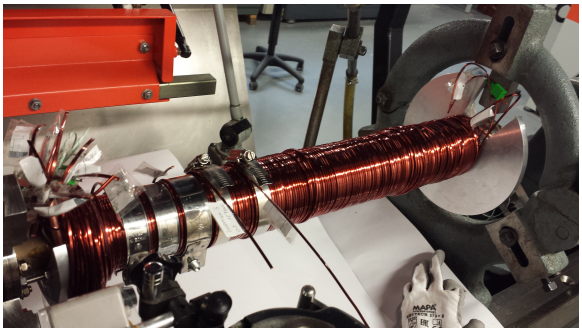

(c) Electric wires with different lengths.

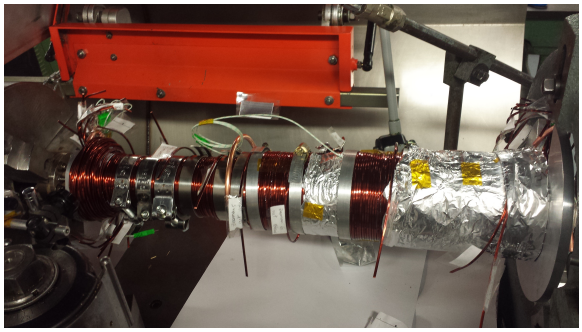

(d) Almost finished winding

Figure 2.8: Zeeman slower during winding procedure.

The Zeeman slower is wound in the mechanical workshop. The winding of the Zeeman slower must take into consideration several practical aspects: Apart from the multiple layers of electric wires to produce the appropriate magnetic field, we will need some heating capacity

installed directly around the vacuum tube to allow to bake the Zeeman slower tube once it is integrated into the vacuum system. After that, some cooling capacity is also needed, in that a power consumption on the order of several hundreds of Watts to one kilowatt is estimated during operation. For these requirements, we install three types of wires.

A first layer of *heating tapes* are wound directly around the CF40 tube and then covered with a layer of Kapton tape to protect from the rest of the layers. We then wind two layers of *hollow copper tubes* along the whole length of the tube for cooling purposes. After that, we wind multiple layers of *electric wires* with appropriate lengths according to prior calculations, using a wire with rectangular section ($2.5 \times 1.6\,\mathrm{mm}^2$). A third layer of cooling tubes are added between the 4th and the 5th layer of electric wires.

Zeeman light The light for the Zeeman slower derives directly from a TA chip, and has a power of 200 mW at the output. After fiber coupling the output is around ∼80 mW at the experiment. We enlarge the beam diameter with a waist of approximately 1 cm at the entrance of the CF40 window and we converge the beam approximately at the position of the oven. The repumping frequency is derived from the cooling frequency with a resonant EOM[(h)] at 228 MHz. A quarter waveplate is placed directly in front of the vacuum window to produce a σ^+ polarization.

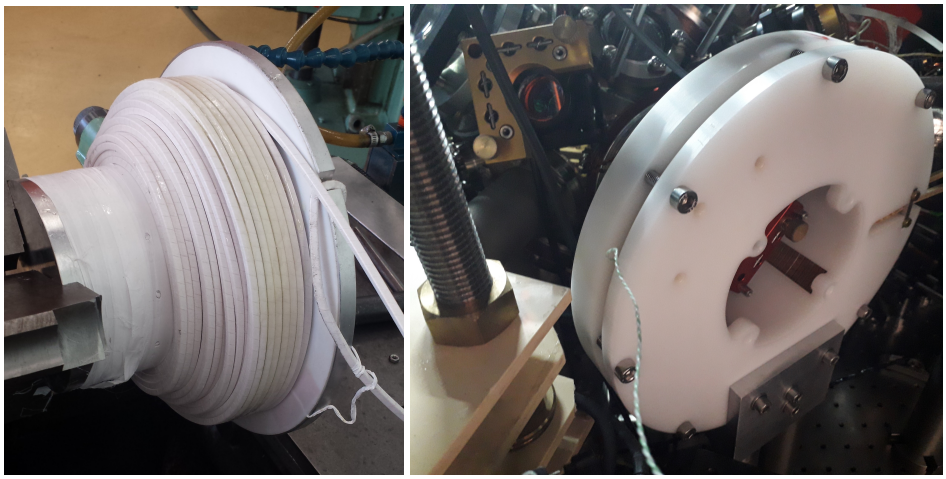

Figure 2.9: MOT coils during the winding process (left) and after being integrated on the main experiment (right).

Realization The measured magnetic field of the Zeeman slower compared to the calculation are presented in Fig. 2.10. We see a globally very good agreement between the calculated field and the realistic field.

Using the measured magnetic field, we can also estimate the velocity evolution of atoms with different incoming velocities. We see that the Zeeman slower can capture atoms up to velocities up to around 830 m/s.

[(h)] Qubig EO-Li6-M3

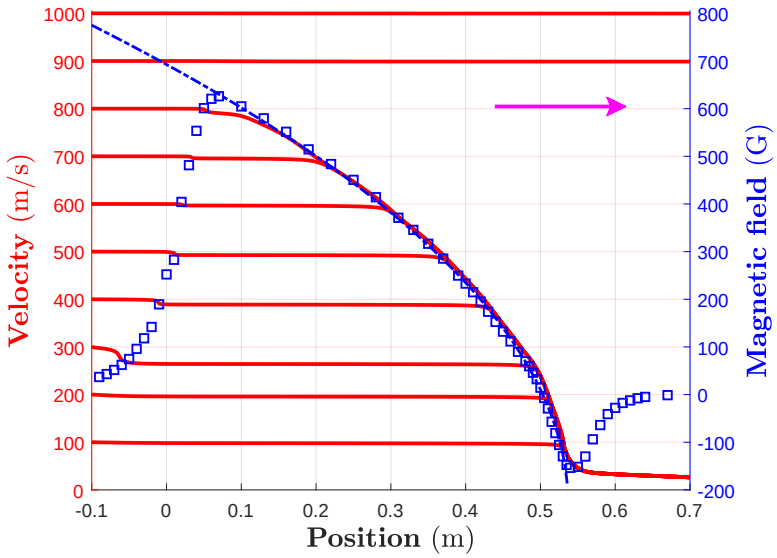

Figure 2.10: Magnetic field of the Zeeman slower (blue) and the velocity evolution for different incoming velocity groups. The dashed line is the calculated magnetic field and the square points are the measured field after realization, which shows excellent agreement. The velocity evolution is calculated using the measured data, for an atom in stretched state, with a laser detuning of $\sim -300\,\mathrm{MHz}$ and with a saturation parameter of $s_0 \approx 20$. We see that all atoms having velocities smaller than $\sim 830\,\mathrm{m/s}$ are slowed down to around $50\,\mathrm{m/s}$, which is the typical capture velocity of a lithium magneto-optical trap.

2.3.3 Magneto-optical trap

After the deceleration of the atomic jet through the Zeeman slower, the atoms are captured in a Magneto-Optical Trap (MOT).

MOT coils Two identical coils are needed to produce a gradient on the order of $10^1\,\mathrm{G/cm}$ for the MOT. Since the main chamber is relatively large, the distance of the magnetic coils from the center of the chamber cannot be smaller than 10 cm. This in turn limits the minimal size of the MOT coils to be comparable to this value. Such a large diameter will very likely block the adjacent vacuum viewports. A compromise is then to have conical shaped coils to ensure the optical access (Fig. 2.9).

MOT beams Like the Zeeman beams, the MOT beams are derived directly from a TA with a total output of ∼300 mW (Fig. 2.6). Differently from the Zeeman slower beam though, it is necessary to switch off the MOT beams quickly with an AOM. The output light is then split in four and coupled into four different fibers and fed through the main chamber. In two of the three mutually perpendicular directions, the MOT lights are retro-reflected (Fig. 2.3). For each MOT beam we have a waist of roughly 7 mm and a power of ∼10 mW. This gives an intensity of $I \sim 5\,I_{\mathrm{sat}}$ per beam.

2.3.4 Gray molasses cooling

Gray molasses implemented on the D_1 line of ^{6}Li allows to efficiently reach sub-Doppler temperatures. Compared to previous techniques such as sympathetic cooling using another atomic species [96–98] or loading into an optical cavity [99, 100], gray molasses is simple to implement and efficient in cooling performance. In the new experiment we intend to apply this technique for reaching sub-Doppler temperatures for ^{6}Li.

D_1 gray molasses light The experimental realization of the D_1 molasses necessitates high intensity. We have a Toptica TA Pro uniquely dedicated to this purpose (Fig. 2.6). The gray molasses beams are combined in one direction with the MOT beams and separate beams in the two other directions. All beams in three directions are retro-reflected. For the two directions that are not mixed with the MOT beams, we have 18 mW with a beam waist of 4 mm. And in the direction combined with the MOT beam, we have 77 mW with a beam waist of 8 mm. This yields an intensity of $\sim 30\, I_{\mathrm{sat}}$ in each of the three directions.

The repumping frequency is derived from the cooling frequency using an EOM. Since the gray molasses requires good coherence between the cooling frequency and the repumper frequency, we use a DDS, which has a linewidth of 20 Hz, as the RF driver source for the EOM.

Magnetic field compensation The magnetic field during the D_1 gray molasses must be well compensated in order to reach the lowest temperatures. For this purpose, three pairs of magnetic field compensation coils are installed around the main chamber in the same directions of the MOT beams. They are mounted directly around the CF60 viewports and have 17 turns each. With a current of several Amperes, each pair can provide an offset magnetic field of several Gauss easily.

2.3.5 Optical pumping and imaging

The detection of the atomic cloud is done with absorption imaging. In the experiment the atoms are detected both at low field and at high field (~ 832 G).

For the low field imaging we use the transition $F = 3/2 \rightarrow F'$. This light is derived from the same master laser used for the Zeeman and the MOT beams. However, at different stages of the experiment, it is possible that the atoms are not all in the $F = 3/2$ hyperfine states. In order to count all the atoms at low field, before we shine the imaging pulses, we shine an optical pumping pulse which lasts for $\sim 5\,\mu$s, detuned to $F = 1/2 \rightarrow F'$ to optically transfer the atoms from $F = 1/2$ to $F = 3/2$.

For the high field imaging around 832 G, the Zeeman shift makes the imaging frequency about 1 GHz red detuned from the transition at low field. This energy difference cannot be easily covered using an AOM. Our solution is to dedicate a DL pro laser for performing the high field imaging and the frequency is offset-locked with the D_2 laser based on the beatnote between them. Details of the offset-lock setup can be found in [93]. The frequency of this laser is also on the sub-MHz level, sufficiently small compared to the linewidth for imaging purposes.

2.4 Magnetic field in the science cell

The science cell is separated from the main chamber by 31.5 cm. The main evaporation in the science cell happens with a magnetic offset field at 832 G, where lies the Feshbach resonance between state $|1\rangle$ and state $|2\rangle$. This requires at least one pair of coils, hereafter named Feshbach coils, to be placed around the science cell in the Helmholtz configuration to create a homogeneous field up to this value.

In practice, we add furthermore another pair of coils, hereafter named curvature coils, to also create a curvature in the horizontal plane to provide some additional magnetic trapping.

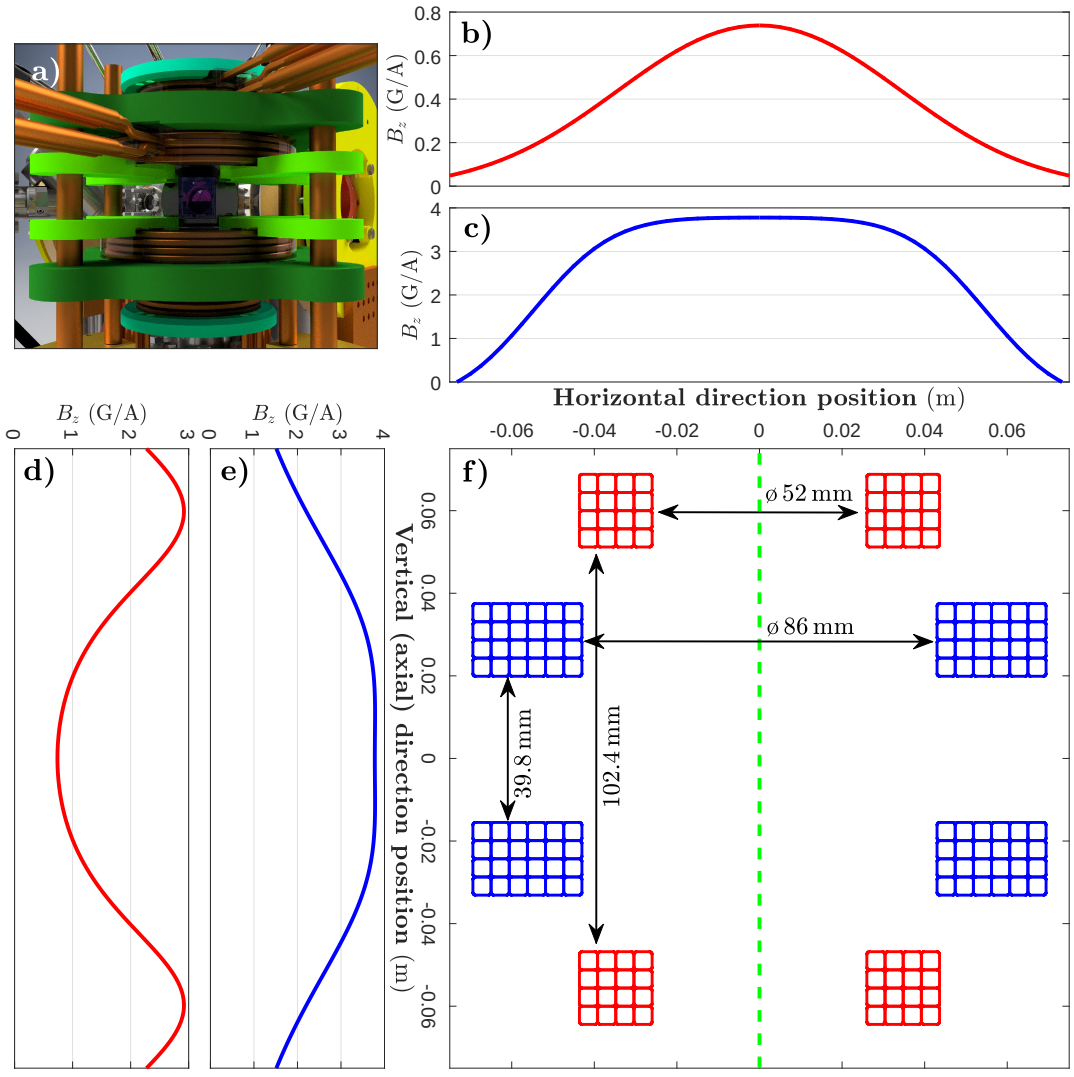

Figure 2.11: The magnetic field and the positioning of the two pairs of coils around the science cell. a) View along the science cell, with two Feshbach coils placed close by and two (smaller) curvature coils placed further. b) The magnetic field created in the median horizontal plane by the curvature coils. c) magnetic field created in the median horizontal plane by the Feshbach coils. d) The magnetic field created in the vertical axial direction by the curvature coils. e) The magnetic field created in the vertical axial direction by the Feshbach coils. f) Simplified view of the coils' arrangement. The green dashed axis denotes the coils' axial direction.

In Fig. 2.11, we show the designed magnetic field created by these coils in the axial (vertical) direction and in the horizontal plane. The Feshbach coils are designed to create only an homogeneous offset field. Whereas the curvature coils generate rather a curvature with a small offset.

With the dimension shown in Fig. 2.11, the Feshbach coils can create an offset field of 3.78 G/A. The curvature coils can create an anti-confining curvature of 0.124 G/cm^2/A in the vertical direction and a confining curvature of 0.062 G/cm^2/A in the horizontal plane, which is half the value in the vertical direction[(i)]. Also the current in one of these two pairs of coils can be inverted and create a gradient at the position of the atoms. For the Feshbach coils, the gradient created in the vertical direction is 0.033 G/cm/A and for the curvature coils 0.011 G/cm/A.

2.5 Experiment control

The experiment machine is controlled by two National Instruments PXI systems connected to a control computer. For our application, digital cards and analog cards are used to output logic signals (0 or 3.3 V) or continuous outputs (-10 V to 10 V). The analog cards we use have a resolution of 12 bits.

The software for controlling the experiment is developed by Aviv Keshet at MIT [101] to operate the NI-system. A very user-friendly and easy-to-manipulate interface is provided for editing the experimental sequence. Once the sequence is edited, buffers are generated and uploaded onto the NI-system which output the set values inside each clock cycle. The timing of the sequence is ensured by an external FPGA with variable clock speed, which allows for different time resolution during different timesteps and hence allows for longer experiment sequences.

Most of the experiment control signals are opto-coupled. This is to, on the one hand, protect the feedback to the control computer from the experiment side (high current power supplies for example), and, on the other hand, provide enough current to the devices to prevent current drain from the outputs [102].

2.6 Summary

In this chapter we have presented an overview about the whole experiment and the essential hardware to control and perform laser cooling on atomic ^{6}Li and to reach the Feshbach resonance at 832 G. In the next chapter we will present results of the laser cooling on the atoms of ^{6}Li.

[(i)] Note that the curvature in the vertical axial direction and in the horizontal plane, according to Maxwell's law, have opposite sign. Hence if in one direction the trap is confining in the other direction the trap is anti-confining.

Chapter 3

Laser cooling results

In this chapter we show the results of laser cooling on ^{6}Li atoms. In particular we show the realization and characterization of a large MOT of ^{6}Li and the sub-Doppler cooling of ^{6}Li by implementing a gray molasses on the D_1-line. With these laser cooling strategies, we achieve an atomic sample of 7×10^8 atoms at a temperature of $\sim 50\,\mu$K in less than 2 s.

3.1 Oven and Zeeman slower

In this section we show some preliminary but very interesting results of laser cooling before having the MOT, including the characterization of the atomic jet flux and the operation of the Zeeman slower using spectroscopic measures.

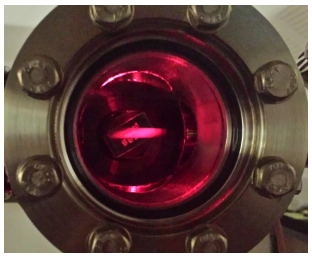

Figure 3.1: The atomic jet out of the oven illuminated with a perpendicular beam.

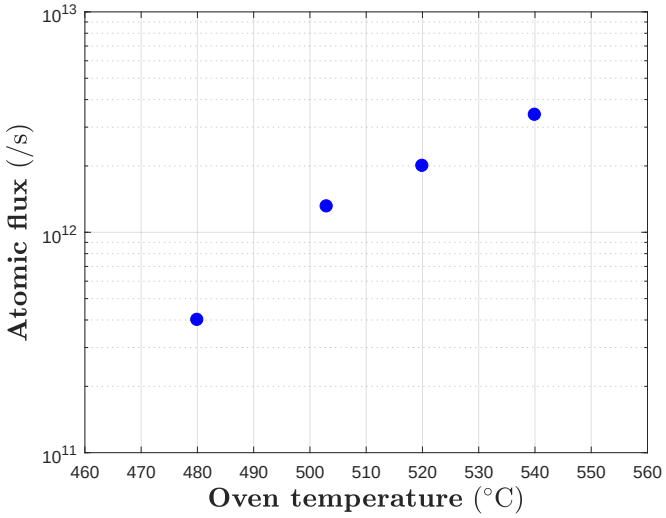

Figure 3.2: The atomic flux as a function of the oven temperature.

3.1.1 Oven flux

The oven flux can be measured by collecting the fluorescence of the atomic jet illuminated by a beam, shining perpendicularly to it. We can collect this fluorescence using a lens, and by taking into account the solid angle defined by the collecting lens and the sensitivity of the photodiode we can evaluate the number of fluorescence photons per unit of time. With this we can deduce the atomic flux. When the oven is heated to 500 °C, the estimated atomic flux is about 10^{12}/s (Fig. 3.1).

We see that the atomic flux decreases by a factor of two for every 20 °C approximately.

3.1.2 Zeeman slower operation

The atoms coming from the oven are able to be slowed down by the Zeeman slower from several hundreds of m/s to around 50 m/s as we have seen in chapter 2.

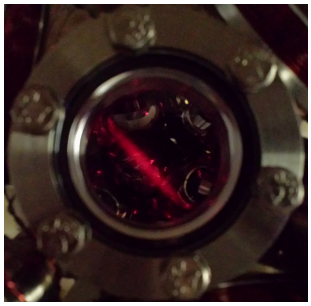

Figure 3.3: The atomic jet in the main chamber illuminated with an inclined beam.

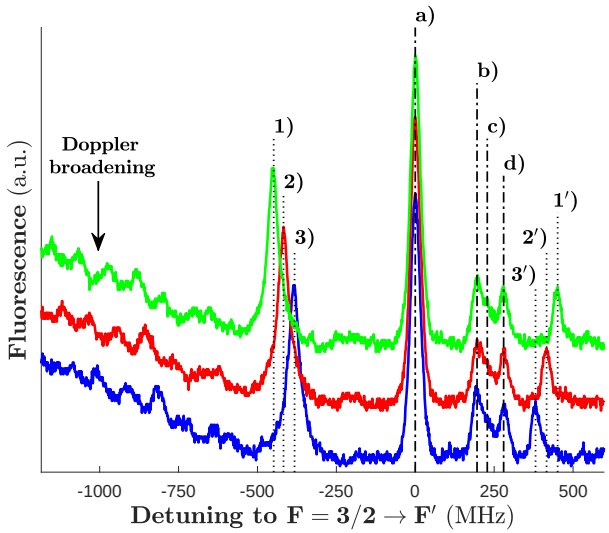

Figure 3.4: The Zeeman slower while functioning with current $I = 16.7$ A. The lines resulting from the perpendicular beam: a), b), c) and d). The angle between the perpendicular beam and the atomic jet gives the calibration ratio for detuning and speed $v/\delta = 0.82\,(\mathrm{m/s})/\mathrm{MHz}$. From the green line to the blue line, the exit velocity of the atomic jet decreased by 55 m/s.

One way to test the functioning of the Zeeman slower, without having a MOT, is to send a laser beam with an angle different from 90° to the atomic beam [103]. By scanning the laser frequency, we can probe the velocity distribution of the atomic beam. Depending on whether the Zeeman slower is operational, this velocity distribution also varies. More specifically, when the frequency of the Zeeman slowing beam is changed, we are able to see the velocity distribution of the atoms going through the Zeeman slower evolve accordingly.

In practice, we send not only the aforementioned beam with an angle but also another beam perpendicular to the atomic jet. This perpendicular beam does not see the velocity distribution and hence serves as a reference for zero velocity. The intensity between these two beams are

very different: The angled beam has a high intensity since it is resonant only with the atoms with the right velocity and consequently shows a weaker fluorescence, while as the perpendicular beam is resonant with all the atoms. In practice, the angle beam is sent with an angle of 35° to the atomic beam and has a power of 24 mW with a waist of approximately 4 mm, which gives an intensity of 40 I_{sat}. On the contrary, the perpendicular beam has the same waist but only a power of 100 μW.

The fluorescence of these two beams are collected on a photodiode. The representative results are shown in Fig. 3.4, the lines a), b), c) and d) are the peaks due to the perpendicular beam. The peaks 1), 2) and 3) represent the different velocity groups of atoms when we change the Zeeman beam frequency. For different frequencies of the Zeeman beam, we see this peak approaches the peak a), which is the peak correponding to the atoms having zero velocity.

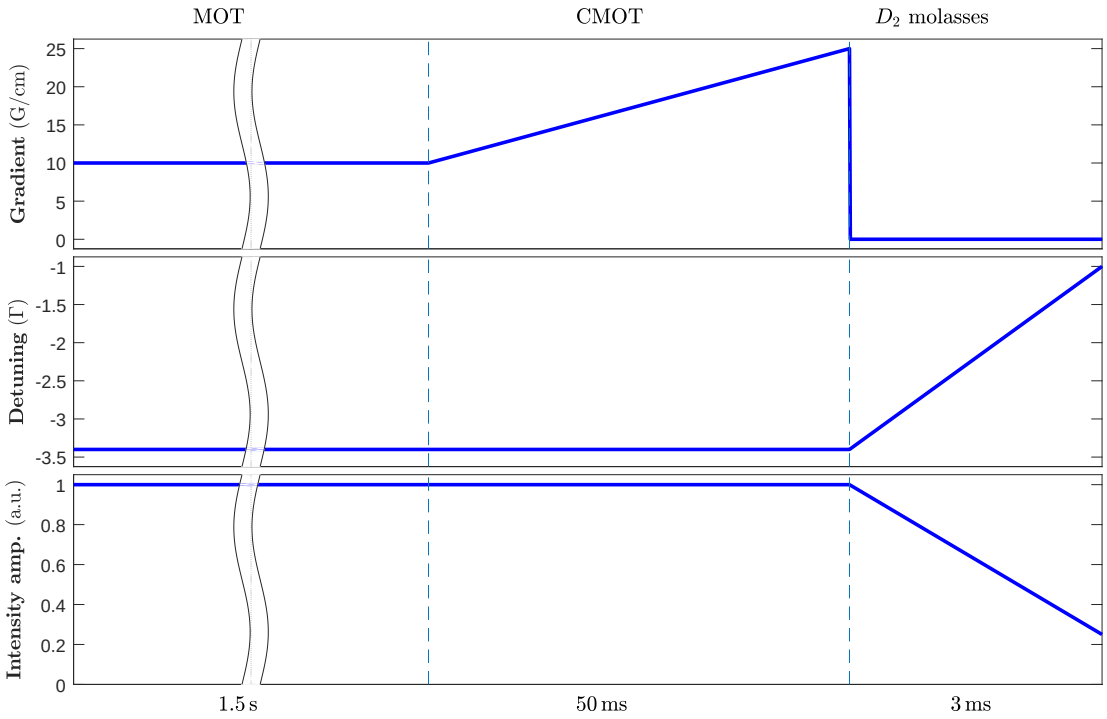

Figure 3.5: The sequence of MOT loading, CMOT and D_2 molasses.

The three peaks 1′), 2′) and 3′) are the three mirror symmetric peaks of 1), 2) and 3) respectively with respect to a). Their presence is due to the reflection on the outgoing windows and hence the atoms having the same velocity in the inverse direction, giving rise to a peak on the other side.

3.2 MOT and compressed MOT

3.2.1 Overview

After the atoms are slowed down by the Zeeman slower, they are captured in the main chamber by the magneto-optical trap (MOT) as shown in Fig. 3.6.

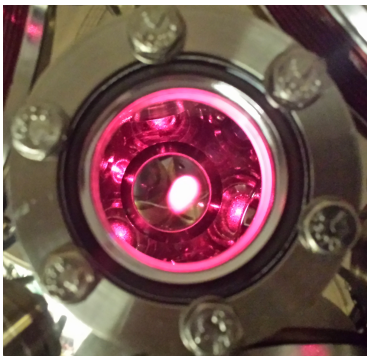

Figure 3.6: Operational ^{6}Li MOT, showing the fluorescence of the trapped lithium atoms.

The MOT loading sequence is shown in Fig. 3.5. During 1.5 s the slowing beams and the magnetic field gradient are switched on, where we can trap up to 10^9 atoms. On a daily basis, more than 8×10^8 atoms are trapped in the MOT when loaded in $1.5 \sim 2$ s. After that, we increase the magnetic field gradient from 10 G/cm to 25 G/cm during 50 ms to compress the MOT. The cloud after compression is only about 1 mm in radius and has a temperature of $1 \sim 1.2$ mK. This size is optimum for the following gray molasses cooling since the gray molasses beams have only a waist of several millimeters. Before implementing the gray molasses, we perform a D_2 molasses with a duration of 3 ms, where we switch off the magnetic field gradient, while at the same time approach the resonance from $-3.4\,\Gamma$ to $-\Gamma$ and decrease the MOT beam intensity by 25%. The role of this D_2 molasses step is two fold: Firstly, the MOT coils induce non negligible eddy current when switched off. This eddy current decays to zero on a timescale of approximately 2 ms, during which time the D_1 molasses does not work due to strong transit magnetic field present. The implementation of this D_2 molasses during this period keeps the atoms in position and prevents the cloud to expand. Secondly, we found also that by performing this step, the temperature of the cloud slightly decreases from 1.2 mK to 900 μK without apparent atom loss.

3.2.2 Detection method

In order to be able to quantitatively evaluate the atom number and the temperatures of the atomic cloud, we perform the standard absorption imaging technique. Here, we recall very briefly the principles of absorption imaging.

We send a laser light pulse with intensity I_0 on an atomic cloud along the z axis. The light is absorbed by the cloud and the intensity through the cloud is given by

$$I = I_0 e^{-n(x,y)\sigma}, \tag{3.1}$$

where $n(x, y)$ is the column density of the cloud and σ the cross section given by

$$\sigma = \frac{\sigma_0}{1 + I_0/I_{\text{sat}} + (2\Delta/\Gamma)^2}. \tag{3.2}$$

with σ_0 the cross section on resonance given by $\sigma_0 = \hbar\omega\Gamma/(2I_{\text{sat}})$. Here Δ is the detuning of the laser from the atomic resonance, Γ the natural linewidth, and I_{sat} the saturation intensity.

The optical density (OD) is defined as

$$OD(x, y) = n(x, y)\sigma, \tag{3.3}$$

and can be experimentally measured by measuring the intensity of the incoming and outgoing intensities of the light pulse. In practice, taking into account the dark currents of the camera and the stray light, the optical density can be measured by taking three pictures: A first picture with the atomic cloud and absorbed imaging beam (I_{atoms}), the second without atomic cloud, hence only the imaging light (I_{light}), and the third a dark picture without the imaging pulse (I_{dark}). The measured optical density is given by:

$$OD = \ln \frac{I_{light} - I_{dark}}{I_{atoms} - I_{dark}}, \tag{3.4}$$

Note that this value is already integrated in the imaging direction along z axis.

Atom number The atom number of the probed atomic cloud then can be obtained by integrating in the imaging plane (x, y):

$$N = \int_{-\infty}^{\infty}\int_{-\infty}^{\infty} n(x, y)\mathrm{d}x\mathrm{d}y = \frac{1}{\sigma}\int_{-\infty}^{\infty}\int_{-\infty}^{\infty} OD\mathrm{d}x\mathrm{d}y. \tag{3.5}$$

Temperature The temperature of the cloud is measured using the time-of-flight expansion technique. For an ensemble of atoms with different velocities, the free expansion of the size is governed by:

$$\sigma(t) = \sqrt{\sigma_0^2 + \overline{v}^2 t^2} \tag{3.6}$$

where the averaged velocity of the ensemble can be associated with the temperature $T = m\overline{v}^2/k_{\mathrm{B}}$.

Hence the temperature can be obtained by fitting the measured sizes of the cloud at different TOFs.

Phase space density The phase space density of the cloud $\mathcal{D}$ depends on the density and the temperature and is defined in the most general case, as

$$\mathcal{D} = n\lambda_{\mathrm{dB}}^3, \tag{3.7}$$

where λ_{dB} is the thermal de Broglie wavelength $\lambda_{\mathrm{dB}} = \sqrt{2\pi\hbar^2/(mk_{\mathrm{B}}T)}$. The density n at the center of the cloud can be evaluated via the atom number and the cloud size.

3.2.3 Dependence on the laser detuning

We show in Fig. 3.7 the dependence of the MOT loading as a function of the detuning of the Zeeman slower beam frequency and the MOT beams frequency.

In these graphs we observed minor dependence on the Zeeman slower beams and the optimum loading in terms of atom number was found around $-3.4\,\Gamma$ for the MOT beams. The temperature of the cloud for large detuning is found to be lower, probably due to the lower

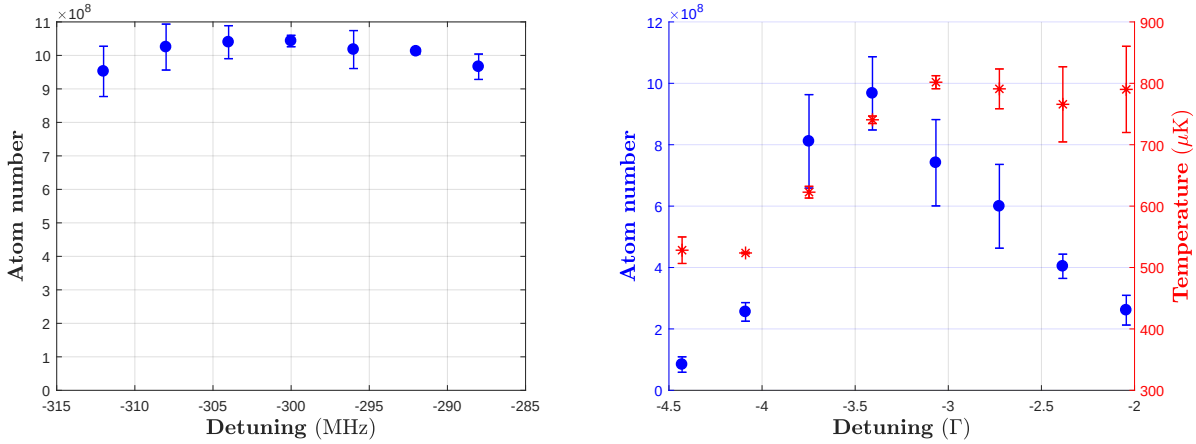

Figure 3.7: The dependence of the atom number in the MOT as a function of the frequency of the Zeeman slower beam (left) and the MOT beams. We did not observe strong atom number dependence on the Zeeman slower beams. Optimum atom number is obtained around $-3.4\,\Gamma$ for the MOT beams.

number of atoms. When we approach the transition however, the atom number decreases, while as the temperature is found to be the same, due to stronger light assisted collisions in this regime.

3.2.4 Dependence on the ratio between repumper and cooler

The repumping frequencies of the MOT beams and the Zeeman beam are generated both with resonant EOMs and sent to a Fabry-Perot cavity to measure and monitor the power ratio between these two frequencies. The dependence of the power ratio between them on the MOT loading is reported in Fig. 3.8.

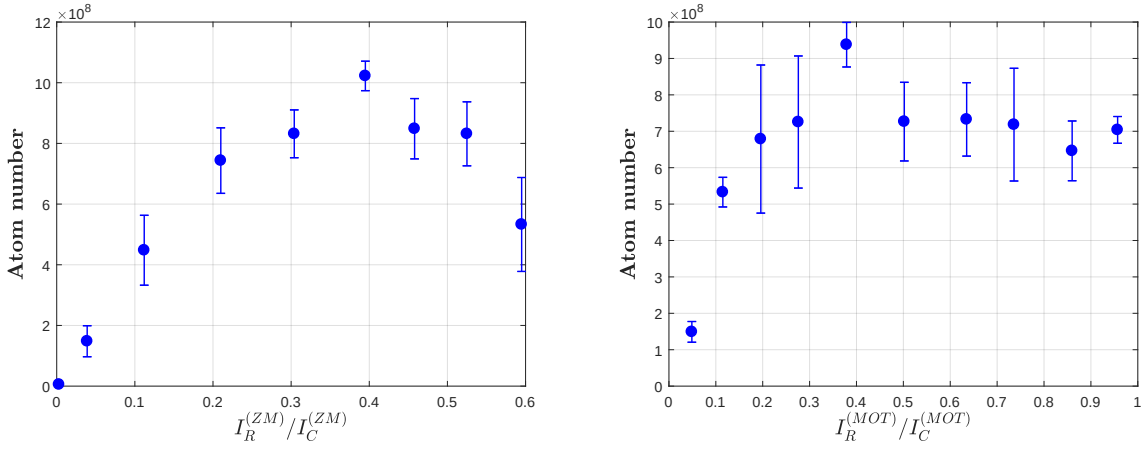

Figure 3.8: The dependence of the atom number in the MOT as a function of the ratio between the repumper and cooler frequencies, for the Zeeman beam and the MOT beams respectively.

Optimum loading is found to be around $I_R/I_C \approx 0.4$ for the Zeeman beam as well as the MOT beams.

3.3 D_2 molasses

The D_2 molasses, as we mentioned previously, allows the cloud to expand diffusively instead of ballistically. In particular, we have found that the frequency of the beams at the end of the ramp (Fig. 3.5) has an important effect on the density of the cloud and we report this dependence in Fig. 3.9.

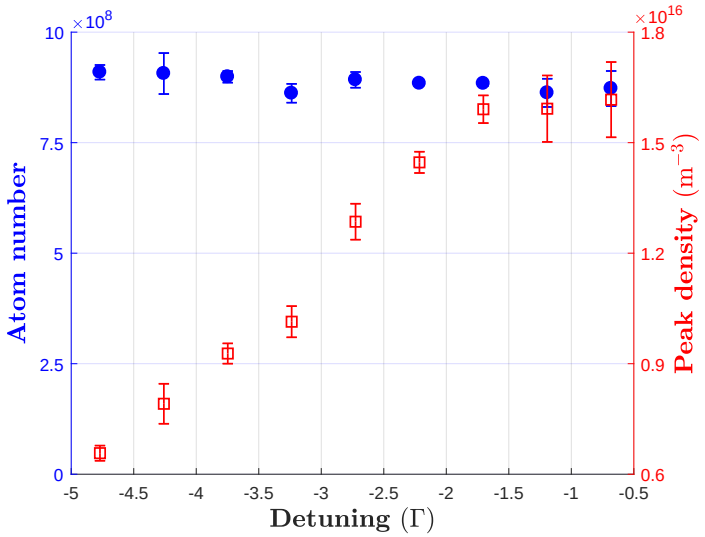

Figure 3.9: The dependence of the atom number and the density of the cloud as a function of the final detuning of the D_2 frequency ramp. Data measured with 1 ms TOF.

We found that by approaching the resonance, we increase the peak density of the cloud. The density of the cloud reaches peak value for a frequency ramp up to $-1.7\,\Gamma$ and stays constant. We hence choose the final frequency of the ramp to $-\Gamma$.

Keeping such a high density is favorable. Because on the one hand, the atom number staying constant, a higher density means a smaller volume. This can help the D_1 gray molasses capture more atoms. On the other hand, the density of the cloud during D_1 gray molasses is determined by the density of the cloud at this stage and a higher density would benefit also the later loading into an optical dipole trap.

3.4 Performances of D_1 gray molasses

After the D_2 molasses the atoms are captured by the D_1 gray molasses. The sub-Doppler cooling of ^{6}Li has always been complicated until several years ago, since the hyperfine splitting of D_2-line of ^{6}Li is badly resolved. In 2012, sub-Doppler cooling has been achieved first on the D_1-line of ^{40}K [104], later also on ^{7}Li [105] and on ^{6}Li [92]. Up till recently, the D_1 gray molasses has been widely implemented and has become a popular tool to reach sub-Doppler cooling temperatures for alkali atoms [106–108].

3.4.1 Principle of operation

The principle of, as well as thorough theoretical and experimental studies on gray molasses are well explained in [109] and in [110]. Here we will only briefly mention the essential working mechanism for completeness.

The principle ccoling mechanism of the gray molasses is the combination of Sisyphus cooling and VSCPT (Velocity-Selective Coherent Population Trapping). Historically, Sisyphus cooling have been implemented on alkali species ^{87}Rb and ^{133}Cs on the D_2 line in the form of bright molasses. Sisyphus cooling makes use of a light polarization gradient in place to cool the atomic cloud below the Doppler limit. The handwaving explanation for its working principle is as follows: Two counter-propagating and red detuned beams create a spatially periodic modulation of the polarization. As a result, a spatial dependent Zeeman shift is created and the atoms see a sinusoidal potential shape in real space. When it is at a potential maximum, the atom is more likely to be excited to the excited state. Therefore an atom "climbs" the potential hills before getting pumped back to the lower energy lying state in a repetitive way, until it does not possess enough energy anymore to climb the energy hill.

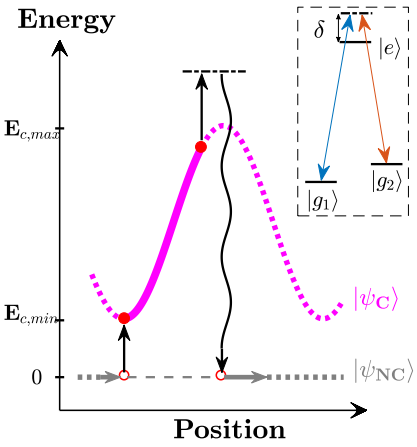

Figure 3.10: Principles of working of the gray molasses.

In *gray* molasses, the use of two pumping frequencies allows to pump the atom in a "dark" state, not coupled to the light. The probability to leave this non-coupled state for a coupled state is the highest at the bottom of a potential energy hill for the coupled state, which then allows Sisyphus cooling.

For ^{6}Li, since the D_2 lines are not well resolved at all, the bright molasses of ^{6}Li leads to heating and atom loss. Instead, blue detuned light on the D_1 transition, together with appropriate magnetic field compensation, leads to efficient cooling.

3.4.2 Realization and sequence

The D_2-MOT beams and the D_1 gray molasses beams go through different viewports, apart from in one direction where they are combined. Therefore it is very important to assure a good spatial overlap between the two molasses. In practice, we tune the D_1 beams on resonance and shine individually in the three directions of the molasses and we make sure the light destroy the D_2 molasses. Once the cloud can be captured by three pairs of D_1 beams with the correct detuning, we change finely the current values in the three pairs of compensation coils to optimize the atom number and the temperature of the captured cloud.

The sequence of the gray molasses is as depicted in Fig. 3.11 and consists of three steps. The gray molasses beams are first switched on at maximum power during 3 ms to capture the atoms from the D_2 molasses as we described previously. The compensation coils in three mutually orthogonal directions are switched on at the beginning of this step. The current in the three

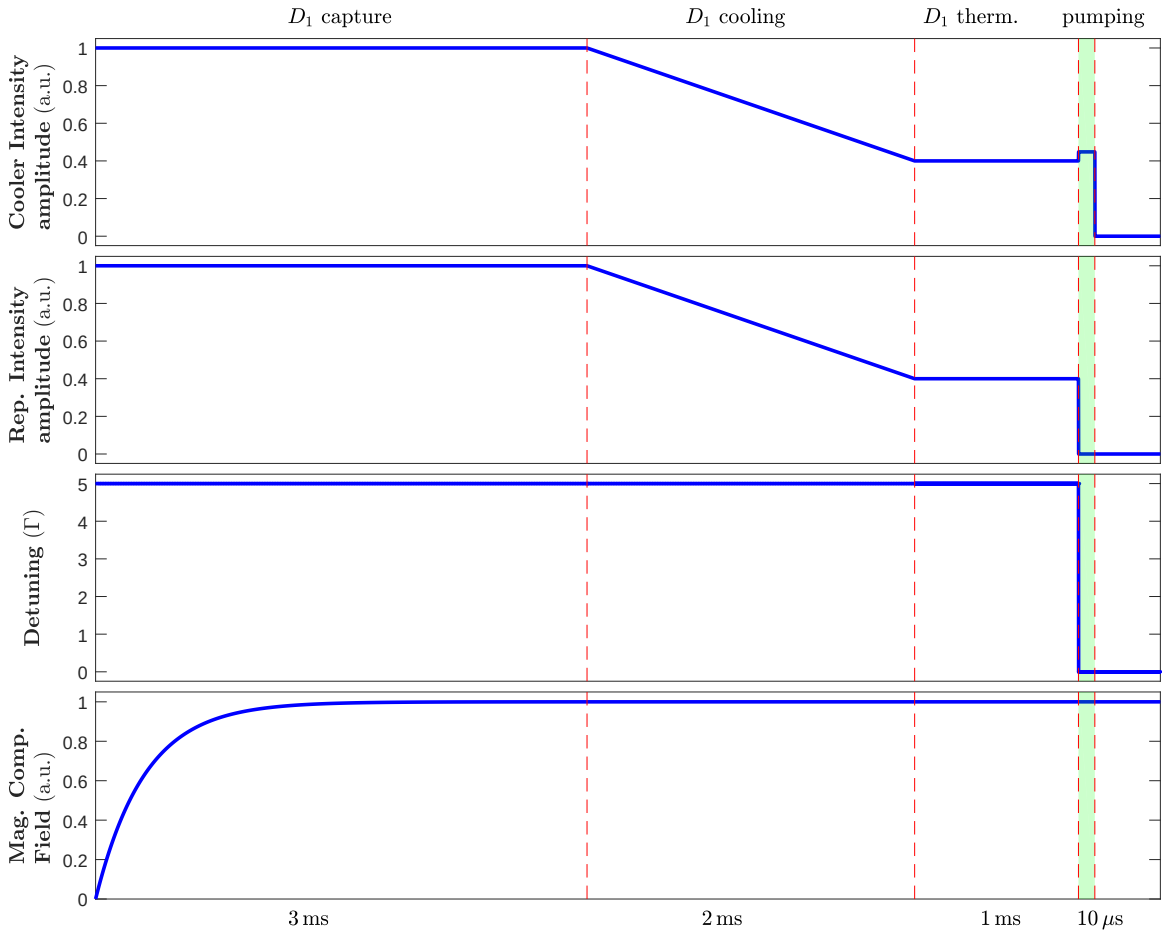

Figure 3.11: The sequence of D_1 gray molasses. Three different phases are included in the cooling process: A first capture phase, where the intensity of the beams are output at maximum, a subsequent cooling phase, where the intensity of the beams are decreased to about one half of the initial maximum value, and a final thermalization phase where the intensity of the beams are hold at the decreased value. A short pulse on the cooling frequency of 10 μs allows most of the atoms to be optically pumped to $F = 1/2$.

pairs of compensation coils reach stationary values in $1 \sim 1.5$ ms due to the limitations of the power supply we use[(a)]. But we found that this transitory magnetic field establishment did not have a strong impact on the temperature decrease on the atomic cloud as we will see later more in detail. Once the temperature of the cloud reaches stationary value, we decrease the intensities of the D_1 gray molasses beams to about 50% of its original value over 2 ms and hold at this final value for 1 ms, to decrease further the temperatures of the atomic cloud. This intensity ramp is found to be able to decrease the temperature by almost 30% without significant atom loss. Finally we switch off the repumper frequency of the gray molasses beams to let all the atoms to fall to the hyperfine level $F = 1/2$. In this way the atoms are automatically in the state $|1\rangle$ and state $|2\rangle$ when going to high magnetic field, which serves as a good starting point for evaporation that we will present in detail in chapter 4.

3.4.3 Magnetic field compensation

The compensation of the residual magnetic field is done by scanning the current values in the three pairs of compensation coils. In the left plot of Fig. 3.12, we show the dependence of the temperature on the applied magnetic field. Here the temperatures are measured after 3 ms of gray molasses capture so that the temperature already reached equilibrium (Fig. 3.12 right). We see that the minimum in temperature also corresponds to the maximum in atom number.

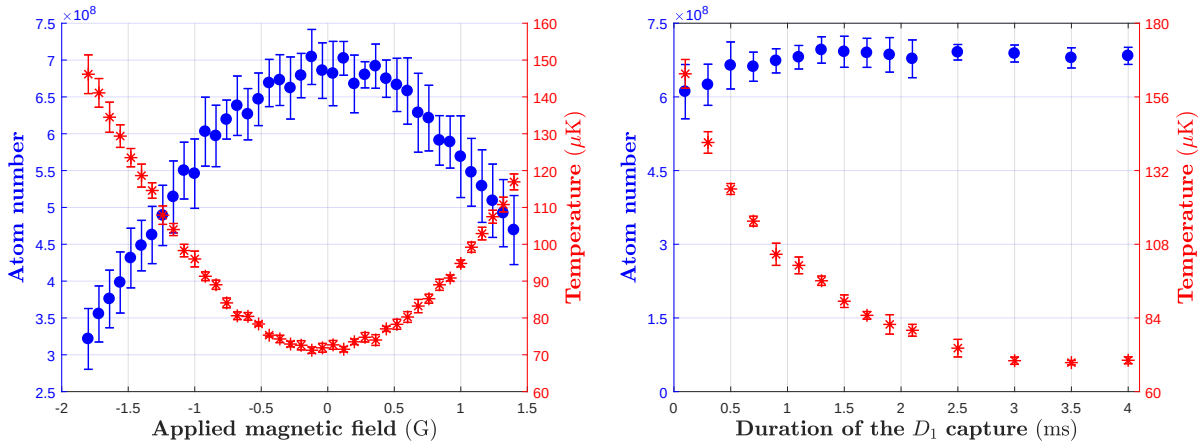

Figure 3.12: Left: magnetic field for optimizing the temperature and the atom number in the gray molasses. Right: Temperature and atom number as a function of the duration of the gray molasses.

3.4.4 Cooling efficiency

The D_2 molasses having a temperature of approximately 900 μK, the D_1 gray molasses proves to be extremely efficient in terms of cooling: The cloud are cooled down to ~100 μK in approximately 1 ms and reaches the equilibrium temperature of 70 μK in merely 3 ms (Fig. 3.12).

[(a)] Delta-Elektronika ES 015-10

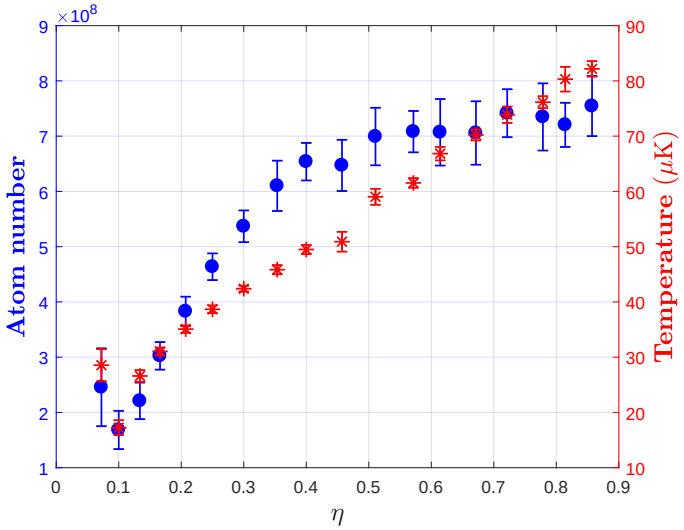

Figure 3.13: The performance of the D_1 molasses cooling as a function of η, which is the ratio of the final intensity value to the initial intensity value. From the graph we see that for $\eta \gtrsim 0.5$, the temperature decreases whereas the atom number stays the same. For $\eta \lesssim 0.5$, the temperature continues to drop whereas the atom number also begins to decrease. For very small $\eta \lesssim 0.1$, the molasses cannot hold the atoms anymore and we observe heating.

3.4.5 Ramp optimization

Like the D_2 molasses, an intensity ramp of the molasses beams allows to decrease the cloud temperature even further. We have optimized the end value of the intensity ramp and we show this result in Fig. 3.13.

In the graph, the parameter η is defined as the intensity ratio between the final value of the intensity ramp and its initial (maximum) value. We see a clear optimum around $\eta \approx 0.5$ where we have a maximum amount of atoms while the cloud can be cooled to a temperature of around 50 μK.

3.4.6 Capture efficiency

The capture efficiency of the D_1 molasses from the D_2 molasses is determined principally by the overlap of the beams, due to the small beam diameters of the D_1 beams. Compared to experiments where the MOT beams are mixed together with the D_1 beams [92, 111] where the gray molasses capture efficiency from a D_2 cloud reaches unity, in our case we reach only about 70% to 80%. On a day-to-day basis, we can capture 5×10^8 to 7×10^8 atoms in the D_1 gray molasses. Representative images of the cloud after D_2 and D_1 molasses are shown in Fig. 3.14.

Although the capture efficiency is lower in our case, it has little or next to no influence on the following experimental step, which is loading into an optical dipole trap. As we will see in the following chapter, the low loading efficiency of an optical dipole trap from an atomic cloud makes the less-than-unity efficiency of the gray molasses less critical. As long as the gray molasses captures most of the atoms from the D_2 molasses and efficiently cools the cloud to sub-Doppler temperatures with high density, it will be largely enough for the dipole trap

loading.

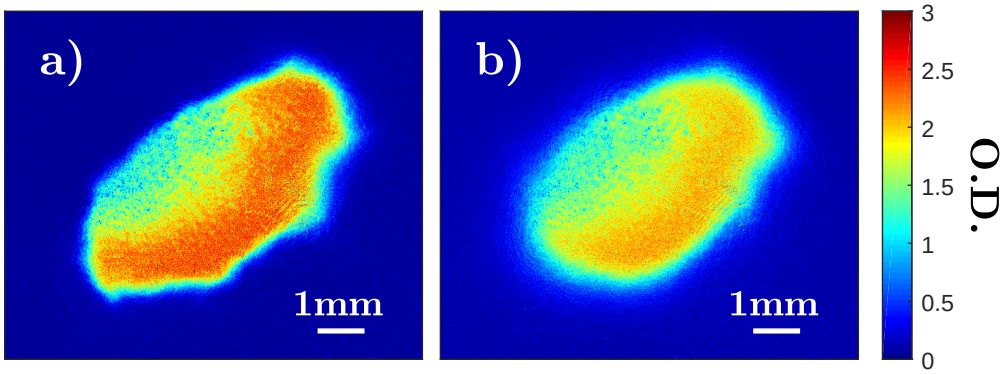

Figure 3.14: The *in situ* images of the D_2 molasses and the D_1 molasses.

3.5 Summary

In this chapter we have shown the main results of the laser cooling on ^{6}Li atoms. By implementing a standard red MOT and applying the gray molasses cooling on the D_1 line, we achieve, on a daily basis, within two seconds an atomic cloud with up to 7×10^8 atoms with temperature as low as $50\,\mu$K. This serves as an excellent condition for loading into an optical dipole trap and perform further evaporation. The parameters for different steps of laser cooling, including the atom number, the temperature and the phase-space density (PSD) is summarized in Table 3.1.

Table 3.1: Summary of each steps of the laser cooling.

Stage	Atom number	Temperature	PSD
cMOT	$\sim 1 \times 10^9$	1.2 mK	5.5×10^{-7}
D_2 molasses	$\sim 1 \times 10^9$	800 μK	5.8×10^{-7}
D_1 molasses capture	$\sim 7 \times 10^8$	80 μK	1.8×10^{-5}
D_1 molasses cooling	$\sim 7 \times 10^8$	50 μK	5.2×10^{-5}

Chapter 4

Optical transport and evaporation

Once the atoms are cooled by the gray molasses to a temperature of about 50 μK, they are loaded into a high-power optical dipole trap in the MOT chamber and transported into the science cell for further evaporative cooling. In this chapter we will present the high power optical setup for the optical dipole traps, the performances of the optical transport, and finally the results of the evaporative cooling inside the glass cell.

4.1 Introduction

The optical dipole trap [112], together with magnetic trap, are the most widely implemented traps in cold atom experiments. Both have their advantages and disadvantages.

For the magnetic traps, they make use of electromagnets or permanent magnets to create the appropriate magnetic field profiles to trap the atoms. The trapping extension of magnetic traps are given by the dimension of the magnets, typically on the macroscopic scales, i.e. several centimeters. Together with the usual experimental curvature or gradient values, they give rise to a large trap depth to a scale of typically several hundreds of millikelvin. Compared to the standard size and the temperature of the atomic cloud, it is not surprising that with magnetic traps, near unity loading efficiency can be easily achieved. However, the functioning of the magnetic traps depends on the inner states of the atoms and usually requires the atoms to be in the appropriate Zeeman levels[(a)].

Optical traps on the other hand, make use of the dipole force of an off-resonant electromagnetic field on the neutral atoms and depend less strongly on the inner state of the atoms. However, compared to the magnetic traps, the extension of the optical traps are determined by the size of the optical beam waist, which is very often at least one order of magnitude smaller than the size of the atomic cloud. Moreover, the typical depth of an optical trap is only of millikelvin scale and requires high optical power on the order of 10 W to 10^2 W.

Although optical traps have such disadvantages, the trapping frequencies they provide are typically on the order of kilohertz range in the strongly confining direction. This is beneficial for the evaporative cooling, where a strong confinement results in a very high collision rate. Further

[(a)] In most of the cases the atoms are required to be in the appropriate *low field seeking* levels, as it is not possible to create a magnetic field maximum.

increase in trapping frequency can be achieved by crossing two optical dipole traps. Even at the low optical power, the trapping frequencies are typically several hundreds of hertz, which is still larger than the typical magnetic trapping frequencies.

In the spirit of having a quick repetition rate of the experiment, a short evaporation time is preferred. After taking into consideration all the aforementioned factors, we decided to implement a hybrid trap. More precisely, we use one optical trap to load the atoms in the main chamber and then we transport the atoms into the science cell. There we implement another dipole trap to cross with the first one. The trapping in the plane of the two laser beams is further reinforced by a pair of curvature coils.

4.2 Working principle

When the difference between the oscillation frequency of the laser ω and the atomic optical transition ω_0 defined by $\Delta \equiv \omega - \omega_0$, is much larger than the fine and hyperfine splittings of the atoms of interest, ^{6}Li in our case, the atom can be treated as a classical oscillator and the dipole potential seen by the atom can be derived and reads as follows in the case of weak saturation [112]:

$$\begin{aligned} U_{\text{dip}}(\mathbf{r}) &= -\frac{3\pi c^2}{2\omega_0^3}\left(\frac{\Gamma}{\omega_0-\omega}+\frac{\Gamma}{\omega_0+\omega}\right) I(\mathbf{r}) \\ &= \frac{3\pi c^2}{\omega_0^2}\frac{\Gamma}{\Delta(\omega_0+\omega)} I(\mathbf{r}). \end{aligned} \tag{4.1}$$

which is proportional to the laser intensity $I(\mathbf{r})$. Here Γ is the linewidth of the considered transition and c the speed of light.

From Eq. (4.1) we see that if the laser beam is red-detuned ($\Delta < 0$), the potential is attractive and the atoms are trapped at the intensity maxima. Inversely, if the laser is blue detuned then the trap is repulsive and the atoms are trapped at intensity minima.

For a Gaussian beam with a waist w_0 and a power P, the intensity profile in space reads:

$$I(r,z) = \frac{2P}{\pi w_0^2(1+z^2/z_R^2)} \exp\left[-\frac{2r^2}{w_0^2(1+z^2/z_R^2)}\right], \tag{4.2}$$

where r and z are the radial and axial coordinates, respectively. The quantity $z_R \equiv \pi w_0^2/\lambda_{\text{OT}}$ is the Rayleigh length of the dipole trap beam with wavelength λ_{OT}. Hence the largest intensity is achieved at the focus, where the beam has its smallest waist w_0. The depth of the optical dipole trap is given by:

$$U_0 = \frac{3\pi c^2}{\omega_0^2}\frac{\Gamma}{\Delta(\omega_0+\omega)}\frac{2P}{\pi w_0^2} = \frac{6c^2\Gamma P}{\omega_0^2\left(\omega^2-\omega_0^2\right)w_0^2}. \tag{4.3}$$

Close to the trap bottom, the atoms experience a quasi-harmonic potential according to the expansion of Eq. (4.2) around $r = 0$ and $z = 0$. The radial and axial trapping frequencies are

given by:

$$\omega_r \equiv \sqrt{\frac{4U_0}{mw_0^2}}, \tag{4.4a}$$

$$\omega_z \equiv \sqrt{\frac{2U_0}{mz_R^2}} = \frac{1}{\sqrt{2}\pi}\frac{\lambda_{\mathrm{OT}}}{w_0}\omega_r. \tag{4.4b}$$

Note that since the depth scales as $U_0 \propto P/w_0^2$ and the Rayleigh length $z_R \propto w_0^2$, the above frequencies scale as $\omega_r \propto \sqrt{P}/w_0^2$ and $\omega_z \propto \sqrt{P}/w_0^3$.

4.3 Transport trap

4.3.1 Setup

The setup of the transport trap is depicted in Fig. 4.1 a). The setup makes use of a high power laser of 200 W from IPG photonics[(b)] focused down to a designed waist of 62 μm. At maximum power we can have effectively 160 W on the atoms.

Since this setup needs to transport the atoms, which are trapped at the focus of the beam, from the main chamber into the science cell, two rectangular mirrors are mounted on a translation stage from Newport[(c)] that has a full travel range of 16 cm. The effective maximum travel range of the focus position is hence twice this value, i.e. 32 cm, which is slightly larger than the effective distance of 31.5 cm between the main chamber and the science cell center.

Once the focus of the beam is shifted into the science cell, we cross the beam with another dipole trap beam to perform evaporation. The power of the transport beam is controlled by a halfwaveplate mounted on a step-motorized rotational mount together with a high extinction ratio cube. This allows to ramp down the power of the beam from 160 W to 50 mW. Compared to the traditional way of using an AOM to control the power, this option allows us to avoid the thermal lensing issues induced by the AOM crystal. However, this means that we cannot modulate the power of the laser as quickly as an AOM. But since the evaporation is performed on the order of seconds, we do not need to ramp the power as quickly. The fact the power cannot be well controlled, due to the step-motor nature, in a continuous and smooth way, especially at low power, will influence the evaporation strategy as we see later.

4.3.2 Loading performance

During the D_2 molasses we switch on the optical dipole trap already. Then it is kept at maximum power all through the D_1 molasses.

[(b)] IPG YLR-200-LP

[(c)] Newport XMS160-S

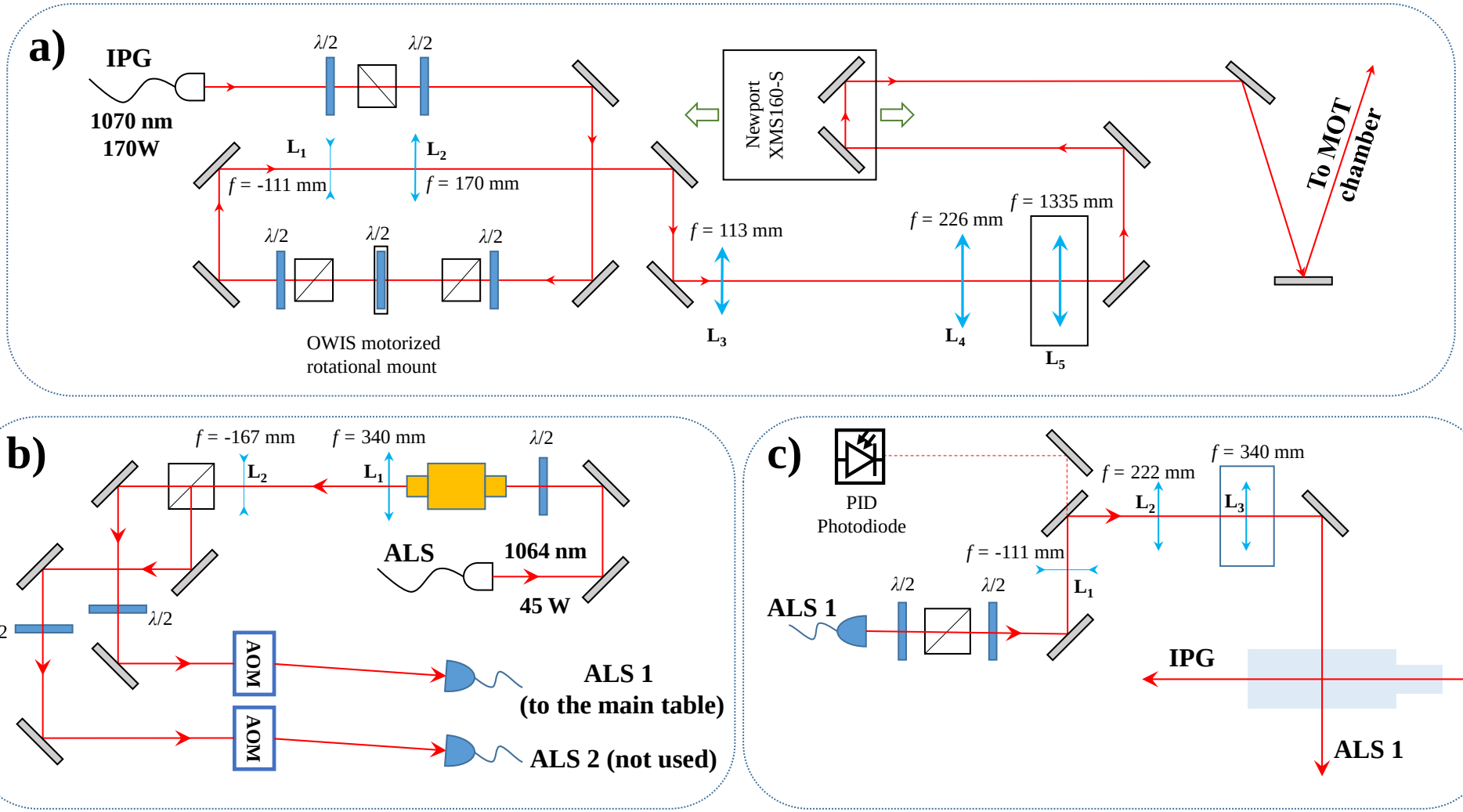

Figure 4.1: The simplified laser set-up. a) The optical setup of the transport trap. The trap is designed to have a waist of 62 μm at the position of the atoms. b) The optical setup of the crossed dipole trap with the ALS laser, designed to have a waist of 60 μm. c) The ALS setup on the main table. The spatial orientation of the beams as well as the imaging directions around the science cell is shown in Fig.4.8.

The loading of the dipole trap depends on the ratio of the trap depth and the cloud temperature $\eta \equiv U/k_{\mathrm{B}}T$, as well as the spatial overlap between the optical dipole trap and the atomic cloud. Mode matching between the cloud shape and the dipole trap shape can improve the trap loading [111]. In our case we did not try to extend the cloud to match the dipole trap's shape. Since the gray molasses beams go through the CF16 viewports and have small diameters, it is difficult to change the diameters of the beams. In fact, we have found that the trap loading depends more on the cloud density after the D_1 molasses rather than the absolute atom number. In the main chamber we have two independent observation axes, along which we can observe the dipole trap's positioning compared to the gray molasses. One of these observation axes is along the dipole trap. This direction is particularly useful because it integrates all the column density of the atoms loaded in the IPG. We can easily find a signal by looking in this direction to begin with. Once we have optimized the positioning along this direction we can switch to the other observation axis, which has an angle of approximately $60°$ compared to the IPG axial direction.

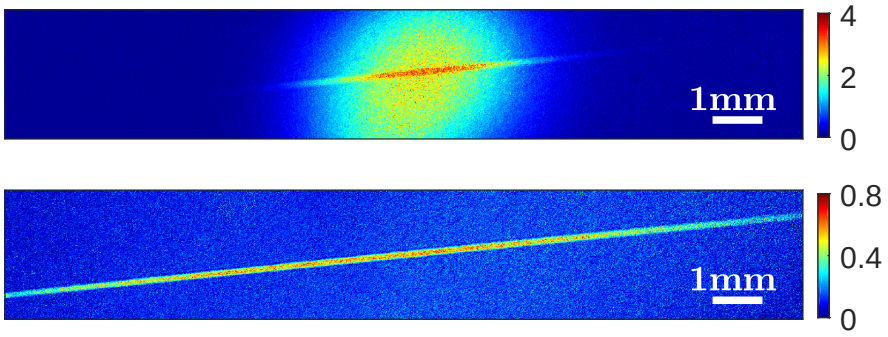

Figure 4.2: Atoms loaded in the IPG. Up: The atoms loaded in the IPG after 2 ms hold time from the D_1 gray molasses. Down: Atoms loaded in the IPG after 20 ms hold time. The atoms not loaded into the IPG are not visible and the loaded atoms are fully extended in the axial direction.

In Fig. 4.2 we show the process of the atoms loading from the gray molasses into the IPG. In the upper panel we show the *in situ* image of atoms in the IPG after having switched off the gray molasses light for 2 ms. The atoms not loaded into the IPG are effectively in time-of-flight expansion. In the lower panel we show the same figure but after having switched off the light for 20 ms. The atoms not loaded into the dipole trap have already flown away and the atoms loaded in the trap are fully extended in the axial direction.

Atom number

The atom number loaded in the IPG depends also on the position of the focus with respect to the cloud. We report the dependence in Fig. 4.3. The maximum atom number ever loaded in the IPG is 7.5×10^6. And on a daily basis, we work comfortably with more than 4×10^6 atoms in the IPG.

The loading of the dipole trap depends on two factors: The depth of the trap and the trapping volume. Both depends on the size of dipole beam waist. On the one hand, in order to achieve

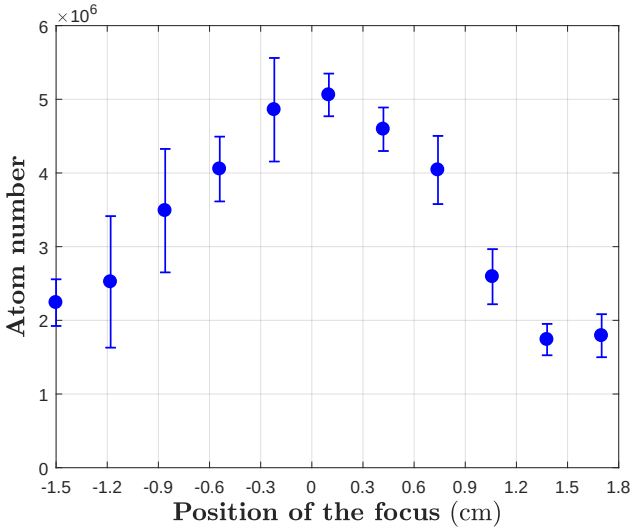

Figure 4.3: Scanning the axial position of the IPG.

efficient loading, the depth of the dipole trap needs to be deep enough, which requires a small waist size. On the other hand, the trapping volume grows as the waist size increases. The optimum loading is a compromise of this two parameters.

When scanning the axial position of the focus and counting the atoms loaded in the dipole trap, we observed a single maximum value. This means that the limiting factor in our case is mainly the depth of the optical trap. If the optical dipole trap is deep enough, while scanning along this direction we would observe two maxima, corresponding to a larger trapping volume away from the focus as shown in [113] for example.

Temperature

The temperature of the atoms loaded in the IPG after 20 ms of hold time is measured to be 120 μK using a time-of-flight technique, which is higher than the temperature of the cloud before loading ($\sim$50 μK). The actual increase of temperature can result from many factors. Generally speaking, in a more tightly confining optical potential forces the cloud has higher density. Since the gray molasses still works in presence of strong electromagnetic field, the photon scattering in the dipole trap is also stronger than in free space. Therefore the atoms loaded in the dipole trap have higher temperatures than the D_1 molasses in real space. Similar temperatures, however, of atoms loaded in the dipole trap from the gray molasses of ^{6}Li has been reported [111].

Before transporting the atoms, it is useful to understand the effects of the dipole trap at maximum power on the atoms when holding them in the main chamber. We plot the atom number and the measured temperatures for different hold times in the main chamber in Fig. 4.4.

This plot shows that the atom number drops in the first 100 ms after loading and stays the same afterwards. The temperature stays the same during the first 500 ms after loading and then increases linearly with a heating rate of $42 \pm 8\,\mu$K/s found by a linear fit.

This heating rate is very large compared to the heating rate induced by off-resonant photon

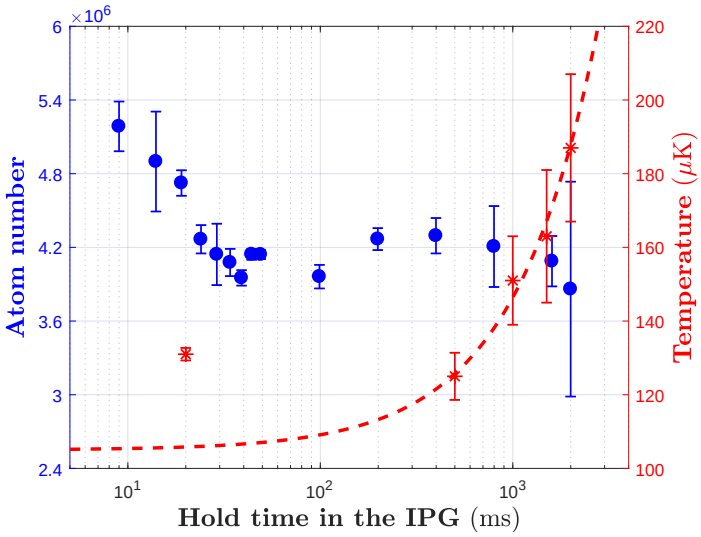

Figure 4.4: Number and temperature of atoms loaded in the IPG as a function of the holding time inside the IPG. The red dashed line is a linear fit of the measured temperature values (first red point not included), which yields a heating rate of $42 \pm 8\,\mu\mathrm{K/s}$.

scattering due to high intensity at the waist. In fact, the absorption occurs with a rate:

$$\Gamma_{\mathrm{sc}} = \frac{\Gamma}{\Delta}\frac{U_{\mathrm{dip}}}{\hbar}. \tag{4.5}$$

With a recoil energy E_{OT} due to the dipole trap light operating at $\lambda_{\mathrm{OT}} = 1070\,\mathrm{nm}$:

$$E_{\mathrm{OT}} = \frac{h^2}{2m\lambda_{\mathrm{OT}}} \approx k_{\mathrm{B}} \cdot 1.4\,\mu\mathrm{K}, \tag{4.6}$$

the heating rate due to off-resonant scattering can be calculated as:

$$\dot{T} = \frac{2}{3}\frac{\Gamma_{\mathrm{sc}} E_{\mathrm{OT}}}{k_{\mathrm{B}}} \approx 3.4\,\mu\mathrm{K/s}, \tag{4.7}$$

which is about one order of magnitude smaller than the measured heating rate. This means that apart from off-resonant photon scattering, there are probably other heating mechanisms, for example, intensity noise of the laser [114] in play.

Eventually, this measurement tells that although we observe significant heating after 2 s, it will not pose a problem if we transport the atoms at shorter timescale.

Trapping frequency measurement

Experimentally we can measure the trap frequency by radially exciting the oscillation through a quick switch-off-and-back-on experiment. Once the cloud is loaded in the trap, we quickly switch off the trap for 30 to 50 μs. This duration is determined by the expected radial frequency of the dipole trap. During this time the cloud slightly expands and we then switch back on the trap to recapture the atoms and record the cloud's radial size as a function of hold time in the dipole trap.

We show this result in Fig. 4.5. We measured an oscillation frequency of 7.93 ± 0.08 kHz, which corresponds to a dipole oscillation frequency of half this value in the limit of high temperature [115], hence 3.97 kHz. And from this frequency, together with the optical power (160W), we extract a waist of $85.6 \pm 0.4\,\mu$m.

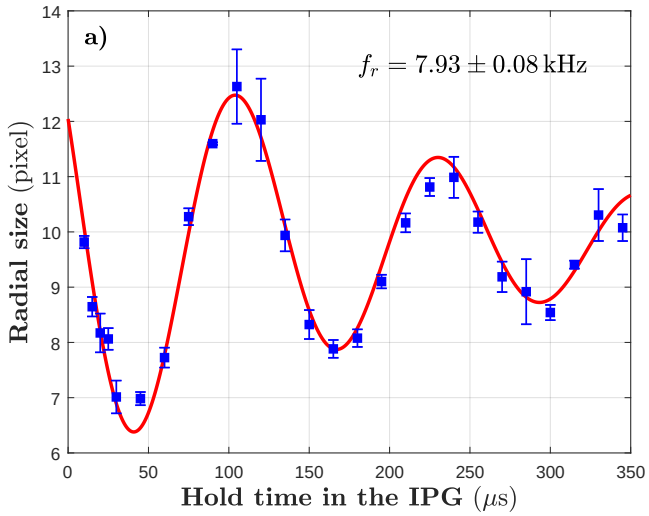

Figure 4.5: Radial oscillation measurement: The measured radial cloud size as a function of the duration held in the dipole trap after the quick switch (see text).

This waist value is larger than the designed value by 40%. There are two possible reasons for this discrepancy. Firstly, the two rectangular mirrors[(d)] used for the transport are relatively thin with a thickness of 5 mm, They are hence more susceptible to distortion due to the force exerted on them during installation. A small curvature due to installation can change the effective waist at the position of the atoms. Secondly, the optical window where the high power laser go through can have some thermal effects and hence changes the beam waist.

The more probable reason for this difference is the second one in our opinion. Since the atoms, when imaged along the transport direction, have a very nice and round shape. The curvature of the mirror surface due to the installation is hardly likely to preserve the cylindrical symmetry of the beam. The vacuum viewport, in contrary, is circular in shape and can indeed preserve the circular symmetry while only change the waist size.

The consequence of this large waist is that the axial trapping frequency of the IPG is only $\sim$8 Hz, which penalizes the evaporation as we shall see later.

4.4 Optical transport

The optical transport is realized by sending an analog signal from 0 to 10 V to the translation stage. Each given voltage correspond to one specific position. The optical dipole trap has to be moved in such a way to avoid axial sloshing. This means that the acceleration during transport

[(d)] Laseroptik L-15116 HR1064-1070 nm/45° 75×50×5 mm

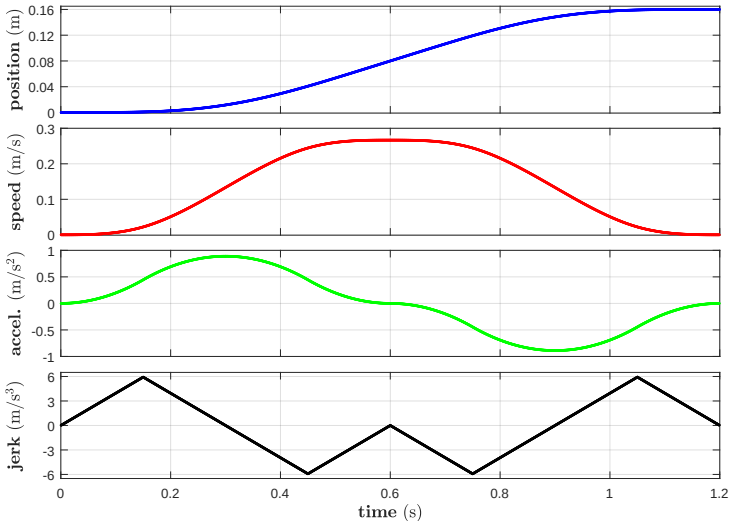

Figure 4.6: The position, velocity, acceleration and jerk (derivative of the acceleration) of the translation stage during transport.

needs to be varied smoothly to avoid sudden changes in the inertial force seen by the atoms. This inertial force also needs to minimally disturb the potential along the axial direction.

The actual curve of the transport that we chose is a quartic curve (fourth order of the time) as shown in Fig. 4.6. The jerk, defined as the time derivative of the acceleration, is a linear function of time. The chosen ramp duration of 1.2 s is a compromise between the heating timescale, the minimization of the inertial force, and the speed limitations of the translation stage.

4.4.1 Transport efficiency

The efficiency of the optical transport is measured using the back-and-forth method: The atoms are transported to different distances during 1.2 s and then back to the MOT chamber with the same duration. The efficiency ξ is the ratio between the number of atoms after the back-and-forth movement and before the transport.

The result of the back and forth transport efficiency measurement is shown in Fig. 4.7. Here we need to specifically notice that the atoms before the transport are counted right after loading into the dipole trap. In Fig. 4.4 we see that there are some atom losses during the first 100 ms after loading. The transport efficiency at 0 travel distance represent this atom loss.

Moreover, we see limited atom number decrease during the transport, with an efficiency ξ^2 going from 70% to 60%. This slow decrease could be due to the increasing inertial forces felt by the atoms for further distances traveled. From these data we can infer a single trip efficiency $\xi = 0.77 \pm 0.04$.

4.4.2 Temperature after transport

We measure the temperature in the science cell and we found similar temperature as indicated in Fig. 4.4, i.e. 150 μK. This indicates that the transport itself does not heat up the atoms more than the dipole trap itself.

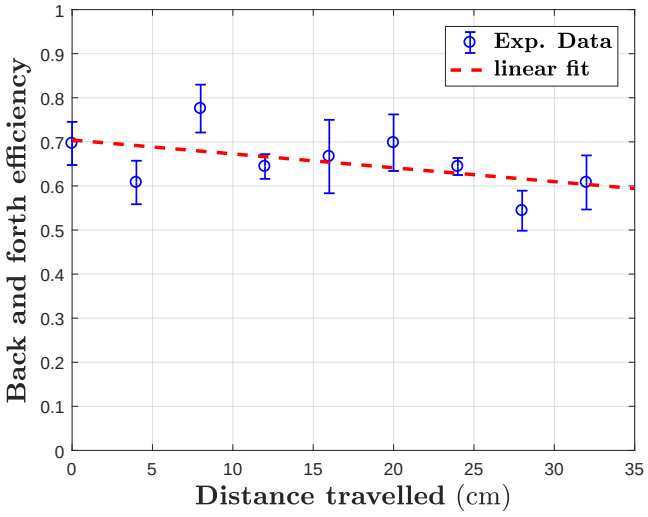

Figure 4.7: The back and forth transport efficiency.

4.5 Crossed dipole trap

4.5.1 Design considerations

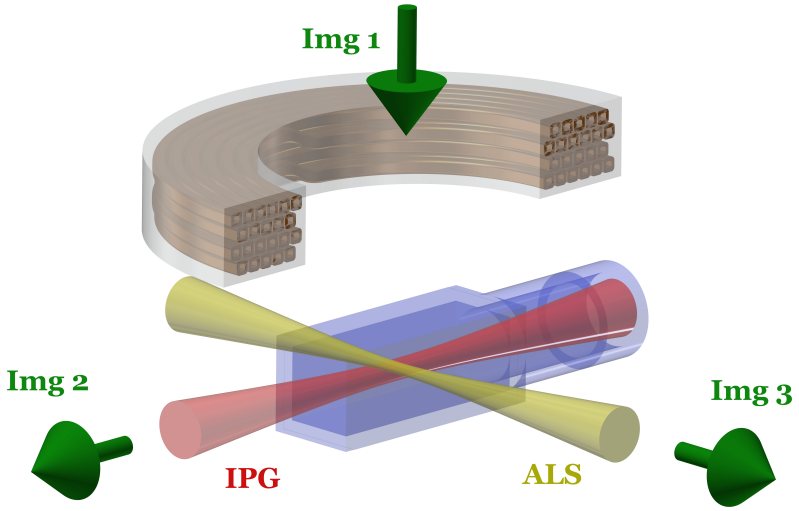

Figure 4.8: The crossed dipole trap in the science cell, composed of the transport beam (IPG) and the ALS beam, with an angle of 90° between them. The three green arrows indicate the imaging directions. One Feshbach coil is shown solely for spatial reference purposes.

As we have seen previously, the larger-than-expected IPG waist makes the axial trapping frequency only on the order of several hertz, which is quite low for providing a axial confinement. In order to perform evaporation efficiently, we decide to cross the IPG beam with another laser beam in order to provide stronger confinement in the aforementioned direction. However, the overlap between two optical traps decreases further the trapping volume of the crossed region and potentially further decreases the atom number.

In order to have a strong confinement and a large trapping volume, there are in general two ideas for designing crossed dipole trap setups, according to the crossing angle between the two dipole trap beams. For small crossing angles (less than 20°), the two dipole trapping arms provide already a relatively large trapping volume, the waists of the two dipole traps arms do not necessarily need to be large. For large crossing angles (close to 90°), it is rather more frequent to have one arm with a small waist ($< 60\,\mu$m) to provide tight confinement and the other a large waist ($> 90\,\mu$m) to increase the trapping volume.

In our experiment we have chosen a waist of $60\,\mu$m for the second arm of the crossed optical dipole trap. This second beam is derived from a high power continuous wave laser [(e)] with 45 W output. The setup of this trap can be found in Fig. 4.1 b) and c). The power of the laser is split into two paths, each controlled by an AOM, on the one hand for fast switching, and on the other hand for power regulation. The diffracted order is coupled into a high power fiber and has a maximum power of 18 W at the fiber output. On a daily basis, we work at about 85% of this power level, i.e. 15.4 W. With a designed waist of $60\,\mu$m, this beam alone yields a potential depth of $k_{\mathrm{B}} \cdot 150\,\mu$K.

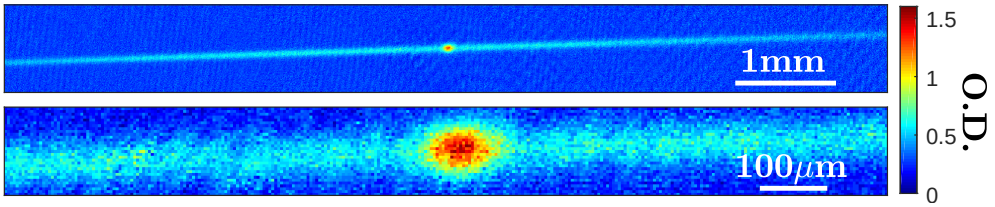

Figure 4.9: Optical dipole trap imaged in the direction of the ALS beam ("Img 3" direction in Fig. 4.8). The lower panel is a zoom of the upper panel in the center region.

The temperature of the gas arriving at the science cell being $\sim 150\,\mu$K, which is comparable to the ALS trap depth, we can already see the effect of the optical dipole trap on the atoms in the transport beam once we switch it on. In Fig. 4.9 we see the atoms in the ODT prior to any evaporation.

4.5.2 Trapping frequency measurement in the science cell

The same measurement as in section 4.3.2 can be taken in the crossed dipole trap to deduce the waist of the ALS beam. We ramp down the power of the IPG to have the atoms fully transferred to the crossed dipole trap (details can be found in the next section). We then switch off the ALS beam and the IPG beam very quickly for $50\,\mu$s and then back on to excite oscillations in the radial directions of the two beams.

Fig. 4.10 shows that from the measurement of the oscillation frequencies at different laser power levels one can deduce the waist of the two beams. The data in Fig. 4.10 yields $w_{\mathrm{ALS}} = 65.0 \pm 1.0\,\mu$m, $w_{\mathrm{IPG}} = 88.7 \pm 0.3\,\mu$m. In particular, the measurement of the IPG waist is in agreement with the previous measurement in the MOT chamber, and the measurement of the ALS waist is compatible with the designed value.

[(e)] Azur Light System ALS-IR-50-SF

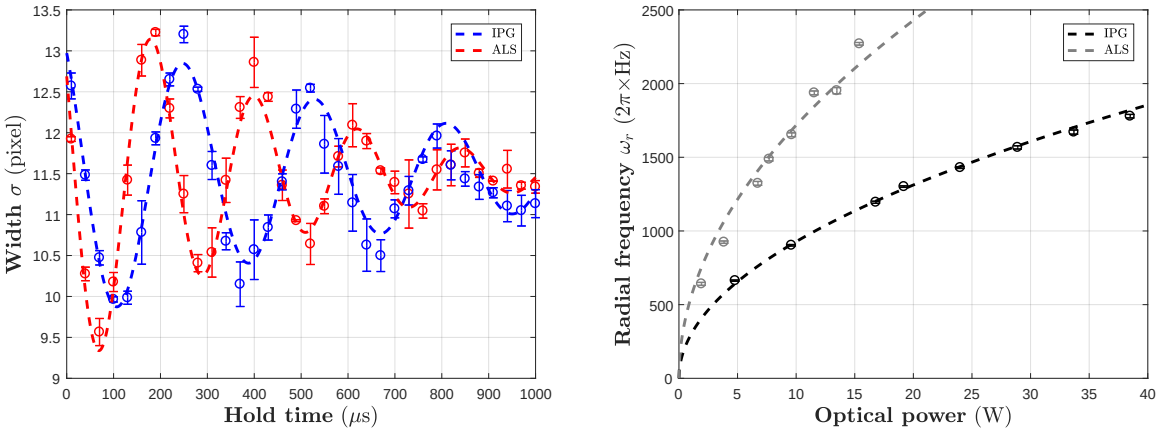

Figure 4.10: Left: Frequency measurements in the crossed dipole trap. Oscillations in the radial directions of the two traps are excited by quickly switching off the ALS and the IPG beams. Right: Measured radial frequencies of the two beams as a function of the beam powers. From the fit we can extract the waist of the two laser beams (see text).

4.6 Evaporative cooling

After the atoms arrive in the science cell, the atomic cloud is further cooled evaporatively. For a Fermi gas, the evaporation is most efficient when the population of the two spin states are equal. In the case of population imbalance, radio-frequency (RF) sweep is a standard technique for transferring atoms from one spin state to the other.

4.6.1 Radio-frequency sweep

At the end of the D_1 gray molasses cooling stage, we have all the atoms in the manifold $F = 1/2$ in he ground state. In the ideal case, the atoms are equally distributed in the two sub-Zeeman levels $m_F = \pm 1/2$. However, in practice we detect almost a factor of 1.5 between the populations of the two spin states. On a day-to-day basis, we have about 1.4×10^6 atoms in state $|1\rangle$ and 0.9×10^6 atoms in state $|2\rangle$ after optical transport.

Landau-Zener sweep

Let us consider two spin states $|1\rangle$ and $|2\rangle$. If all the atoms are in state $|1\rangle$, a RF sweep across the transition frequency allows one to adiabatically transfer all the atoms from state $|1\rangle$ to $|2\rangle$, if the sweeping speed is slow enough.

More quantitatively, the probability of transfer from state $|1\rangle$ to state $|2\rangle$ is given by the Landau-Zener formula [116, 117]:

$$P_{|1\rangle\to|2\rangle} = 1 - \exp\left(-\frac{\Omega^2}{4\dot{\Delta}}\right), \tag{4.8}$$

where Ω is the on resonance Rabi-frequency driven by the RF-transition and $\dot{\Delta}$ the RF frequency sweep speed. For a linear frequency sweep $\dot{\Delta} \equiv \delta\nu/t$, with $\delta\nu$ the swept frequency range and t the sweep duration.

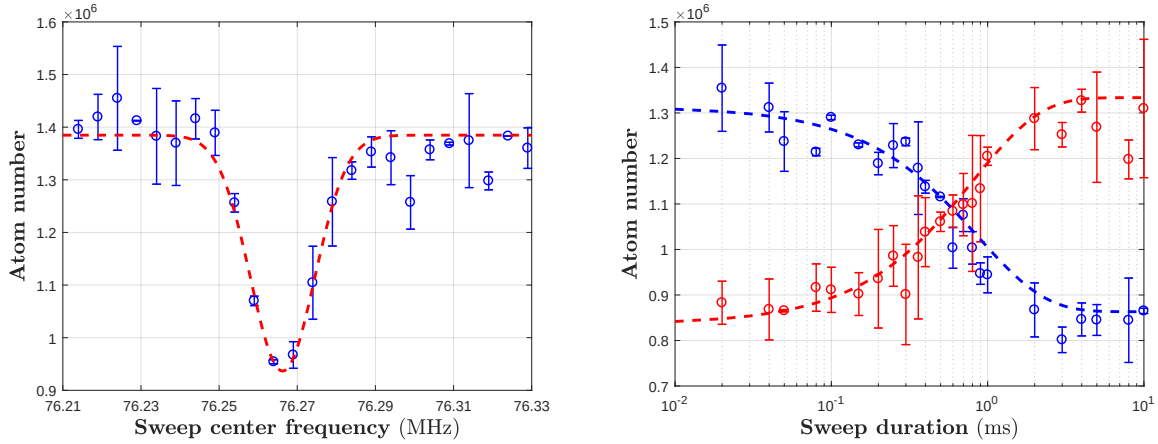

Figure 4.11: Left: central frequency scan for a fixed duration RF sweep with a duration of 20ms and a sweep range of 40 kHz: The start frequency is $f_c - 20\,\text{kHz}$ and the final frequency $f_c + 20\,\text{kHz}$. The fitted Gaussian curve gives a central frequency of 76.267 MHz, which corresponds to a magnetic field of 832 G. Right: the populations of the two hyperfine states after an RF sweep of variable duration centered on the frequency found on the left figure, with a sweep range of 400 kHz. The populations in the two hyperfine states are found to be inversed for long scan duration, which corresponds to an adiabatic transfer. The dashed lines are exponential fits (see text).

Implementation

In order to implement the radiofrequency sweep, an antenna adapted to the dimension of the science cell is made and placed as close as possible. The RF signal is generated from a high-precision RF generator[(f)] and amplified with a high power RF amplifier[(g)] of 50 W.

On-resonance Rabi oscillation

The precise RF transition frequency between the states $|1\rangle$ and $|2\rangle$ can be calculated using the Breit-Rabi formula. At 832 G, this frequency is calculated to be 76.267 MHz.

In order to find this resonance, we apply a sufficiently slow linear RF sweep, typically of 20 ms duration and with a sweep range of 400 kHz to begin with. When the RF transition frequency falls within the sweep range, the atoms in state $|1\rangle$ are adiabatically transferred to state $|2\rangle$ and vice versa. In order to more precisely pinpoint the transition frequency, we gradually decrease the sweep width. In the left plot of Fig. 4.11 the result of such a frequency scan is shown.

Once the resonant RF frequency is found, we can coherently drive the transition between state $|1\rangle$ and state $|2\rangle$ by applying an RF pulse at the resonance frequency. The population between this two states oscillate with a frequency Ω, which is the Rabi frequency as shown in Fig. 4.12.

[(f)] MXG ATE Analog Signal Generator N5161A
[(g)] Mini-Circuits LZY-1+

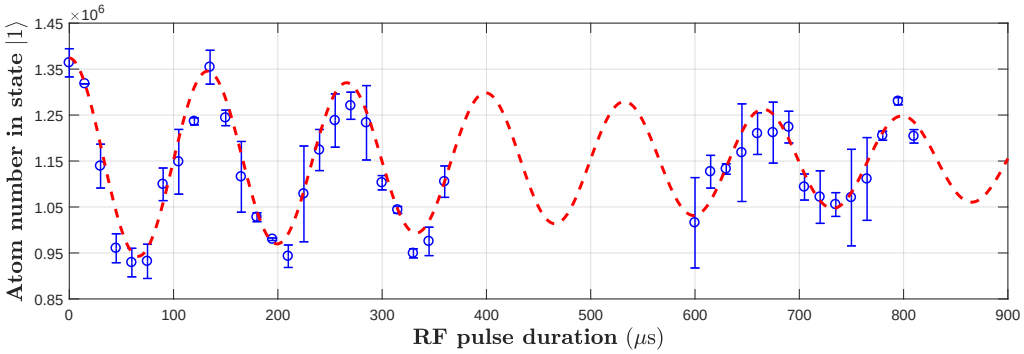

Figure 4.12: The Rabi oscillation observed with state $|1\rangle$. The measured Rabi frequency $\Omega = 2\pi \times (7.51 \pm 0.03)$ kHz. Note that the damping is due to trap inhomogeneity induced decoherence. The time constant for this decay, fitted by an exponential, is $\tau = 960 \pm 160\,\mu$s.

Spin balancing using non-adiabatic sweep

Since we want to balance the spin population of the two spin states, we need to sweep the RF pulse in a non-adiabatic way. By decreasing the duration of the RF sweep, the atom transfer will become more non-adiabatic. The appropriate sweep duration is such that the atom number in the two spin states are equal.

We apply a linear sweep with 400 kHz sweep range, centered on the resonance frequency $f_c = 76.267$ MHz we found previously. We gradually decrease the duration of the sweep and we measure the atom numbers in the two spin states. It is expected that for very quick RF sweeps, the atoms cannot be transferred between the two states and retains the initial number ratio before the RF sweep. For very long RF sweeps, the atoms in one state can always be adiabatically transferred to the other and the population should be inversed, as shown in the right plot of Fig. 4.11.

Since we perform a linear frequency ramp, the sweep speed $\dot{\Delta}$ in Eq. (4.8) can be very well known. As a matter of fact, the on-resonance Rabi frequency Ω is related to the measured exponential time constant τ of the curves in the right plot of Fig. 4.11 as

$$\Omega = 2\sqrt{\frac{\delta\nu}{\tau}}. \tag{4.9}$$

The extracted time constants of the two curves in Fig. 4.11 gives $\tau_1 = 0.86 \pm 0.08$ ms and $\tau_2 = 0.80 \pm 0.05$ ms. According the above expression, we can estimate the Rabi oscillation frequency to be $\Omega_1 = 2\pi \times (7.0 \pm 0.6)$ kHz and $\Omega_2 = 2\pi \times (7.3 \pm 0.3)$ kHz. Both values are in agreement with the direct measurement of the Rabi frequency through Rabi oscillation shown in Fig. 4.12.

As a result, in order to balance the population of the two spin states, we apply a single linear RF sweep of 400 kHz sweep range centered around 76.226 MHz during 550 μs to balance the population in the two spin states. The atom numbers after the RF sweep are typically 1.1×10^6 in each of the two spin states.

Note that after the RF sweep, a wait time of 300 ms is added before we begin evaporative cooing. This wait time, which is much longer than the decay time constant we measured in

the Rabi oscillation, ensures that the atoms are no longer coherent with each other and allow collisions between them.

4.6.2 Evaporative cooling: Principle and key parameters

Evaporative cooling is the major technique in quantum gas experiments to reach ultracold temperatures. The idea is to let the hottest atoms escape the trap and allow the remaining atoms thermalize at a lower temperature. The temperature decrease slows down the escaping process and hence the trap depth needs to be lowered accordingly. In the following we present some of the most important parameters to characterize the evaporative cooling.

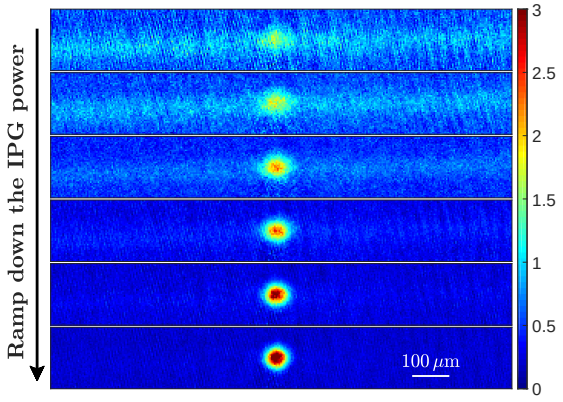

Figure 4.13: The first step of evaporation where the atoms in the IPG are transferred into the crossed dipole trap. In the fist picture we see clearly the atoms still in the IPG wings and in the last figure we see only ALS in the axial direction and the IPG wings are no longer visible. Images are taken in the "Img 3" direction in Fig. 4.8.

Collision rate Γ_{coll} The collision rate describes at which timescale the gas reaches equilibrium. In order to have an efficient evaporation, the collision rate should be as high as possible, ideally larger than $10^3\,\text{s}^{-1}$ in the case of ^{6}Li.

For a gas at unitarity with temperature T, in the high temperature limit ($T \gg T_F$), the collision rate is given by [118]:

$$\Gamma_{\text{coll}} = \frac{2N\hbar^2\overline{\omega}^3}{\pi(k_{\text{B}}T)^2}, \tag{4.10}$$

where $\overline{\omega}$ is the geometrical mean of the trapping frequencies in three directions in space and N the atom number per spin state.

Phase space density $\mathcal{D}$ The phase space density as we have introduced in Eq. (3.7), can be, for a harmonically trapped atomic gas, expressed in terms of the trapping frequencies:

$$\mathcal{D} = \left(\frac{\hbar\overline{\omega}}{k_{\text{B}}}\right)^3 \frac{N}{T^3} \tag{4.11}$$

The goal of evaporation is to achieve a degenerate Fermi gas. This means that the final phase space density $\mathcal{D} \sim 10^0$.

Evaporation efficiency γ The evaporation efficiency γ defined as

$$\gamma = \left|\frac{\ln(\mathcal{D}_{\text{fin}}/\mathcal{D}_{\text{ini}})}{\ln(N_{\text{fin}}/N_{\text{ini}})}\right|, \tag{4.12}$$

compares the orders of magnitudes the number of atoms lost to the increase in phase space density $\mathcal{D}$. For a good evaporation this value should be large.

4.6.3 Implementation and results

Power Stablilisation

The optical power of the evaporation usually can decrease from several tens of Watt all the way down to the mW scale. At such low power, any fluctuations in power would heat up the cloud and hence result in atom loss.

The optical power stabilisation in this regard is especially important for dipole traps at low power. The power of the ALS beam is regulated using the leakage light though a mirror and acting on the driving RF-power of the AOM as shown in Fig. 4.1. We can regulate the power of the ALS beam from 16 W to 25 mW reliably.

However, for the IPG beam, as we mentioned previously, since its power is not controlled by an AOM but with a halfwaveplate on the rotatable mount and a cube, feedback on the rotational mount actually induces noise and due to the mechanical nature of the rotational mount, the response of the PID is very slow (bandwidth on the hertz level). Hence the power of the IPG is not PID-regulated.

Power ramp

The power ramp of the two laser beams, as well as the manipulation of the magnetic field, is shown in Fig. 4.14.

Transfer from the IPG into the crossed dipole trap

Before we perform the evaporative cooling, we typically have a balanced Fermi gas with $N_1 = N_2 = 1.1 \times 10^6$ atoms at a temperature of $T = 150\,\mu$K.

A first evaporation ramp is performed by exponentially decreasing the power of the IPG beam until it provides almost the same trap depth as the ALS beam. At this moment, the cloud is almost all transferred in the cross dipole trap and no wings of atoms in the IPG can be seen (Fig. 4.13).

The power of the IPG is decreased by a factor of $\exp(-1.7) = 0.18$ from its maximum power of 156 W to 28.5 W during approximately 4.5 s. At this stage we have typically $1.7{\times}10^5$ atoms in each spin states with a temperature of $23.1{\pm}0.4\,\mu$K measured using a time-of-flight technique. From these data we can estimate the collision rate and the phase space density before and after this step of evaporation shown in Table 4.1.

Parameters	Initial	Final
Atom number (per spin)	2.2×10^6	3.4×10^5
Temperature	$150\,\mu$K	$23\,\mu$K
Phase space density	2.4×10^{-5}	2.7×10^{-2}
Collision rate	300	5.2×10^4

Table 4.1: Key parameters for the first step of evaporation.

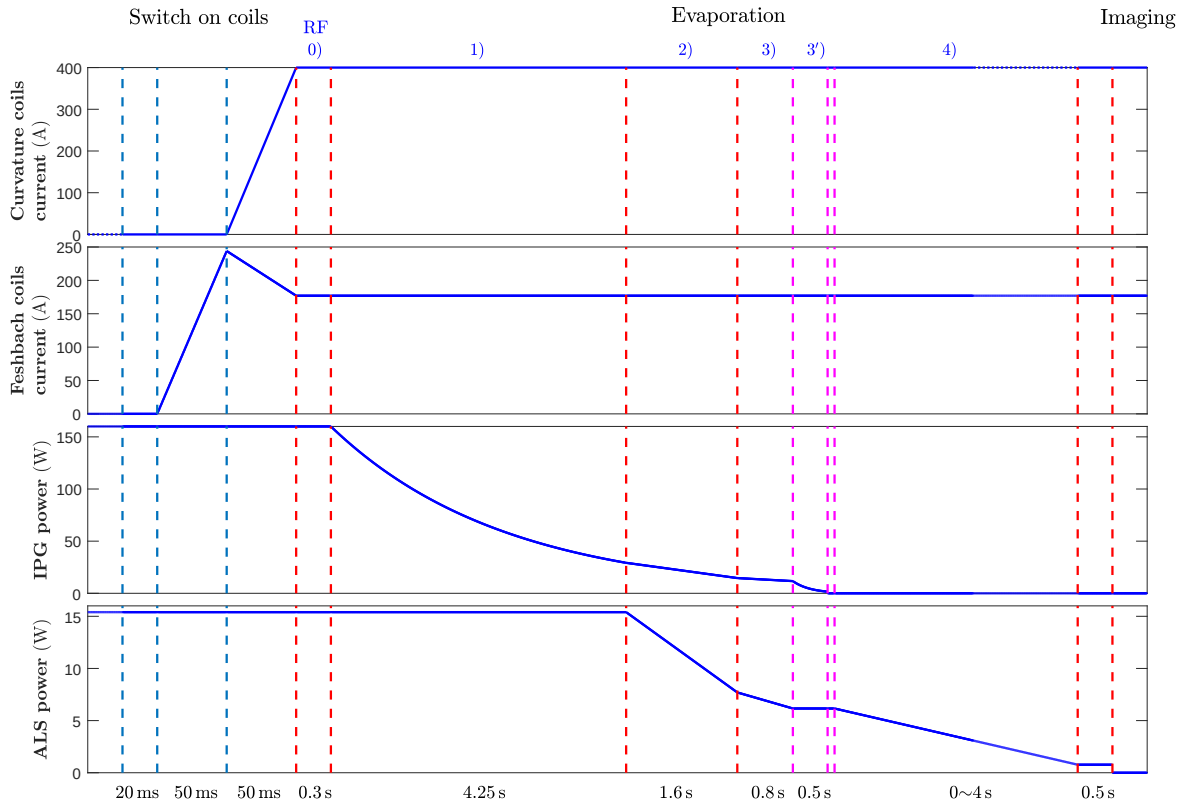

Figure 4.14: The sequence for the evaporation: After the optical transport, the magnetic field are switched on to 832 G during about 100 ms. The RF sweep as we presented previously is done once the magnetic field is stabilized (step 0), and a wait time of 0.3 s is added before we perform any evaporation. A first intensity ramp (step 1) of the IPG beam allows to transfer the atoms into the crossed dipole trap. Two following linear ramps (step 2 and 3) on the IPG and the ALS power consists the evaporation in the crossed dipole trap. Then the power of the IPG is decreased to minimum in 500 ms and switched totally off for another 100 ms using a TTL signal. A further power decrease of the ALS beam (step 4) allows one to finish the evaporation in the single ALS beam. Before imaging, the atoms are held in the final ALS power value for another 500 ms. Finally, the atoms are imaged at high field.

The presence of the ALS beam provides strong confinement in the axial direction of the IPG beam. Hence at the end when all atoms are in the crossed dipole trap, the phase-space density and the collision rate are particularly high, which benefits the following evaporation. Using these parameters, we estimate an evaporation efficiency $\gamma_{\mathrm{IPG}} = 3.7$.

Evaporation in the crossed dipole trap

Once the atoms are totally transferred into the crossed dipole trap, we decrease simultaneously the power of the two beams linearly. We measure the atom number and the temperature corresponding to different power levels shown in Fig. 4.15.

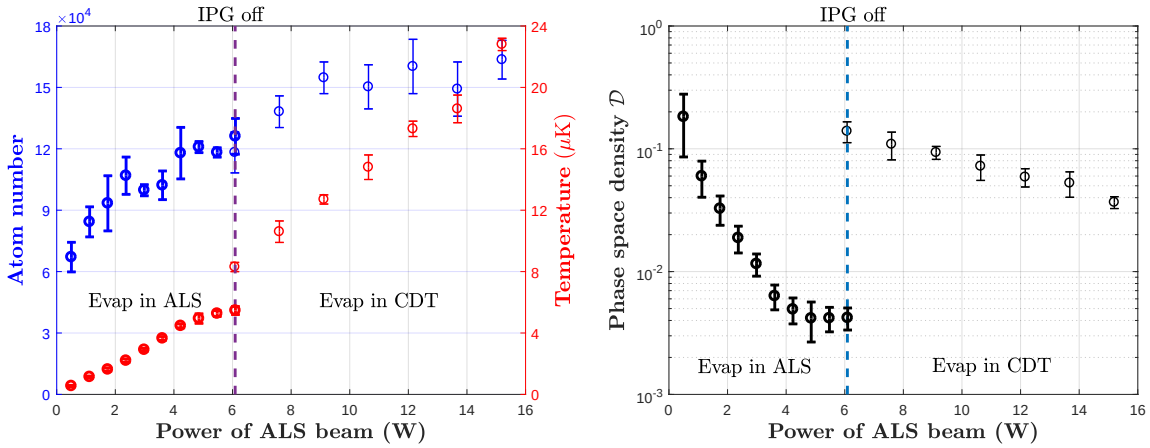

Figure 4.15: Atom number, temperature (left) and PSD (right) evolution in the crossed dipole trap, and later, in the single ALS beam. The evaporation begins in the crossed dipole trap with the ALS beam power at 15.4 W. When both beams are decreased by about 60% of their initial values, we switch off the IPG beam and finish evaporation in a single ALS beam. The phase space density is computed using Eq. (4.11).

From Fig. 4.15 we can see that by decreasing the power of the crossed dipole trap to 40% of its initial values, we gain almost a factor of 3 in temperature while losing only about 30% of the total atoms. The phase space density in this case increases from 2.8×10^{-2} to 1.1×10^{-1}, which is about only one order of magnitude below the degenerate regime ($\sim 10^{0}$).

The evaporation efficiency for this step of evaporation in the crossed dipole trap can be calculated using the aforementioned data to be $\gamma_{\mathrm{CDT}} \approx 4.1$.

Evaporation in single ALS beam

Since the power of the IPG beam is not well controlled, especially in low power, we switched it off during the evaporation and then finish the evaporation in a single ALS beam. The switch-off of the IPG beam is done by ramping the Owis mount to the position corresponding to the minimum intensity during 500 ms and then wait for another 100 ms before performing further evaporation. During the 100 ms hold time, the IPG is switched off totally via a TTL signal to ensure no leakage light is present.

Since we finish the evaporation in a single ALS trap, the trapping in the ALS beam's axial direction must be reinforced by the curvature coils, whose trapping frequency in the horizontal plane is estimated to be around 20 Hz. The duration for ramping off the IPG is chosen to be much larger than the inverse of the minimum trapping frequency, so the operation can be considered as slow.

Parameters	**IPG On**	**IPG Off**
Atom number (per spin)	1.2×10^5	1.2×10^5
Temperature	$8.3\,\mu$K	$5.5\,\mu$K
Phase space density	0.14	4.2×10^{-3}
Collision rate	7.1×10^4	3.2×10^3

Table 4.2: Key parameters before and after switching off the IPG beam.

Further performance of the evaporative cooling in the single ALS beam is also shown in Fig. 4.15. And the key parameters before and after switching off the IPG beam is shown in Table 4.2. When switching off the IPG, we observe a decrease in temperature by slightly less than a factor of two, with no visible atom loss. This means that we perform in this stage a slow and efficient evaporation, in which very few atoms are lost, and we maintain an almost constant $\eta = U_0/k_{\mathrm{B}}T$ (since the ALS beam and the IPG beam have roughly the same trap depth). However, since we lost the trapping in the IPG radial direction and the vertical direction, the phase space density after switching off the IPG has drastically decreased by more than one order of magnitude to 4.2×10^{-3}.

Nevertheless, the evaporation in the single ALS proves to be no less efficient than the evaporation in the crossed dipole trap, since the collision rate in a single ALS beam, although much smaller than that in the crossed dipole trap, still stands at several $10^3\,\mathrm{s}^{-1}$, which ensures the following evaporation in the single dipole beam to be efficient. By decreasing the power of the single ALS beam to about 500 mW, we lose roughly a factor of two in atom number but the temperature decreases by a factor of 10, which leads to nearly fifty-fold increase in the phase space density up to $\mathcal{D} \approx 0.2$. The efficiency of this second stage of evaporation in the single ALS beam has a efficiency of $\gamma_{\mathrm{ALS}} \approx 6.2$.

4.7 Summary

In this chapter we have presented the high power laser setup, dedicated to the loading from a gray molasses in the MOT chamber, the optical transport into the science cell and the evaporative cooling in the science cell.

In particular, we achieve high atom number (at most 7.5×10^6, and more than 4×10^6 on a daily basis) loading in the IPG trap in the MOT chamber and we transport them into the science cell with high efficiency (80%). After balancing the two spin states with a radio-frequency sweep, a first evaporation in the crossed dipole trap and a further evaporation in the single ALS beam

allows to increase the phase space density of the cloud to roughly 0.2.

Further evaporative cooling that allows to obtain a degenerate Fermi gas, and the characterization about such a gas, shall be presented in the next chapter.

Chapter 5

A unitary Fermi superfluid

This chapter describes the last step towards the main goal of this PhD thesis, which is reaching the superfluid state for a strongly-interacting Fermi gas. The work presented here focuses on the emblematic unitary regime where the scattering length a diverges and the system features universal properties. In the following, we provide two complementary proofs of superfluidity. On the one hand, we use thermometry based on the equation of state (EoS) that was already precisely measured [4, 5]. With this method we show that our samples reach temperatures as low as $0.05\,T_{\mathrm{F}}$, well below the critical temperature $T_{\mathrm{c}} = 0.17\,T_{\mathrm{F}}$. On the other hand, we prepare a spin-imbalanced unitary Fermi gas in the phase-separation regime, that is where a superfluid core is surrounded by a halo in the normal phase. By choosing a spin-imbalance sufficiently low to stay below the Clogston-Chandrasekhar limit but large enough to maintain a prominent superfluid region, we were able to reveal the so-called "superfluid plateau" via simultaneous spin-selective imaging.

5.1 Quantitative analysis for probing a degenerate Fermi Gas

5.1.1 Ideal Fermi gas

For an ideal non-interacting Fermi gas, when the thermal energy is much larger than the energy level spacing of the trap, the density of states is approximated by the so-called Thomas-Fermi approximation, which reads:

$$f(\mathbf{r},\mathbf{p}) = \frac{1}{e^{\beta\left(\frac{\mathbf{p}^2}{2m}+V(\mathbf{r})-\mu\right)}+1}, \tag{5.1}$$

where $\mathbf{r}$ (resp. $\mathbf{p}$) is the coordinates in real space (resp. momentum space), and $V(\mathbf{r})$ the external trapping potential and μ the chemical potential at the center of the trap. The parameter $\beta \equiv 1/(k_{\mathrm{B}}T)$.

The real-space density distribution $n(\mathbf{r})$ in such a potential $V(\mathbf{r})$ is obtained by integrating over the whole momentum space

$$n(\mathbf{r}) = \int \frac{\mathrm{d}\mathbf{p}}{(2\pi\hbar)^3} f(\mathbf{r},\mathbf{p}) = -\frac{1}{\lambda_{\mathrm{dB}}^3}\mathrm{Li}_{3/2}\left(-e^{\beta(\mu-V(\mathbf{r}))}\right), \tag{5.2}$$

where λ_{dB} is the thermal de Broglie wavelength and Li_n denotes the polylogarithm of $n-$th order.

Suppose that now the cloud is in a harmonic trap with

$$V(\mathbf{r}) = \frac{1}{2}m\omega_x^2 x^2 + \frac{1}{2}m\omega_y^2 y^2 + \frac{1}{2}m\omega_z^2 z^2, \tag{5.3}$$

the one dimensional density profile $\overline{n}(z)$ can be obtained by integrating[(a)] over the coordinates x and y:

$$\begin{aligned}
\overline{n}(z) &= \int_{-\infty}^{+\infty} \mathrm{d}x \int_{-\infty}^{+\infty} \mathrm{d}y \; n(\mathbf{r}) \\
&= \int_{-\infty}^{+\infty} \mathrm{d}x \int_{-\infty}^{+\infty} \mathrm{d}y \left\{ -\frac{1}{\lambda_{\mathrm{dB}}^3} \mathrm{Li}_{3/2}\left(-e^{\beta(\mu - \frac{1}{2}m\omega_x^2 x^2 - \frac{1}{2}m\omega_y^2 y^2 - \frac{1}{2}m\omega_z^2 z^2)} \right) \right\} \\
&= -\frac{1}{\lambda_{\mathrm{dB}}^3} \frac{2\pi k_{\mathrm{B}} T}{m\omega_x\omega_y} \mathrm{Li}_{5/2}\left(-e^{\beta\mu(z)} \right),
\end{aligned} \tag{5.5}$$

where $\mu(z) = \mu - m\omega_z^2 z^2/2$.

Different definitions of the Fermi temperature The expression Eq. (5.5) is suitable for fitting the one-dimensional doubly integrated density profile of an elongated gas. From the fit we can extract the temperature of the gas T and the parameter $\beta\mu$, which is directly related to the degree of degeneracy T/T_{F}. However, one must distinguish two different definitions of the Fermi temperature T_{F}.

The first definition of T_{F} is based on the highest energy level of an arbitrary potential occupied by an atom at zero temperature. In particular, in the case of harmonic trapping, this energy can be expressed in terms of trapping frequencies $E_{\mathrm{F,HO}} = k_{\mathrm{B}} T_{\mathrm{F,HO}} = \hbar\overline{\omega}(6N)^{1/3}$, with N being the atom number for one spin state. In this regime, the degeneracy parameter T/T_{F} can be readily obtained by integrating Eq. (5.5) over the coordinate z:

$$\left.\frac{T}{T_{\mathrm{F}}}\right|_{\mathrm{HO}} = \left[-6\mathrm{Li}_3(-e^{\beta\mu}) \right]^{-1/3}. \tag{5.6}$$

The second way of defining T_{F} is through the local density of the gas n for each spin state,

$$T_{\mathrm{F}} = \frac{\hbar^2}{2mk_{\mathrm{B}}}(6\pi^2 n)^{2/3}. \tag{5.7}$$

This definition means that for each density n, one can associate a value of T_{F} with it. For a harmonically trapped gas, since the density is not uniform, in the framework of the local density approximation (LDA), the Fermi energy defined in this way is also space-dependent. Since the temperature of the gas, while at equilibrium, is uniform, the degeneracy value T/T_{F} is space-dependent as well. In particular, for a gas at the trap center, the density in 3D, according to Eq. (5.2), is given by

$$n(\mathbf{0}) = -\frac{1}{\lambda_{\mathrm{dB}}^3} \mathrm{Li}_{3/2}\left(-e^{\beta\mu} \right), \tag{5.8}$$

[(a)] The expression

$$\int_{-\infty}^{+\infty} \mathrm{d}\alpha \mathrm{Li}_n\left(z e^{-\alpha^2} \right) = \sqrt{\pi}\mathrm{Li}_{n+1/2}(z) \tag{5.4}$$

is used.

if we assume that $V(\mathbf{0}) = 0$.

With Eq. (5.7) and (5.8), one obtains a local value of T/T_{F} at the center of the trap:

$$\frac{T}{T_{\mathrm{F}}} = \frac{4}{\left[6\sqrt{\pi}\mathrm{Li}_{3/2}(-e^{\beta\mu})\right]^{2/3}}. \tag{5.9}$$

The difference between Eq. (5.6) and Eq. (5.9) is that the former is a *global* quantity, determined by the *global* trap shape and depth, as well as the total atom number, while as the latter is a *local* quantity, which depends on the *local* gas density. Since in our experiment we have an harmonic trap, in order to describe the local thermodynamic quantities and properties, the second definition is more appropriate. In the following, unless explicitly explained otherwise, the T/T_{F} is the local degeneracy value at the center of the trap.

Pressure Note that the pressure of the gas P_0, thanks to the to the Gibbs-Duhem identity, is proportional to the integrated density [119]:

$$P_0(\mu(z), T) = \frac{m\omega_x\omega_y}{2\pi}\overline{n}(z). \tag{5.10}$$

Therefore, the pressure of the gas, using Eq. (5.5), can be expressed as:

$$P_0(\mu(z), T) = -\frac{k_{\mathrm{B}}T}{\lambda_{\mathrm{dB}}^3}\mathrm{Li}_{5/2}\left(-e^{\beta\mu(z)}\right). \tag{5.11}$$

5.1.2 Strongly interacting Fermi gas

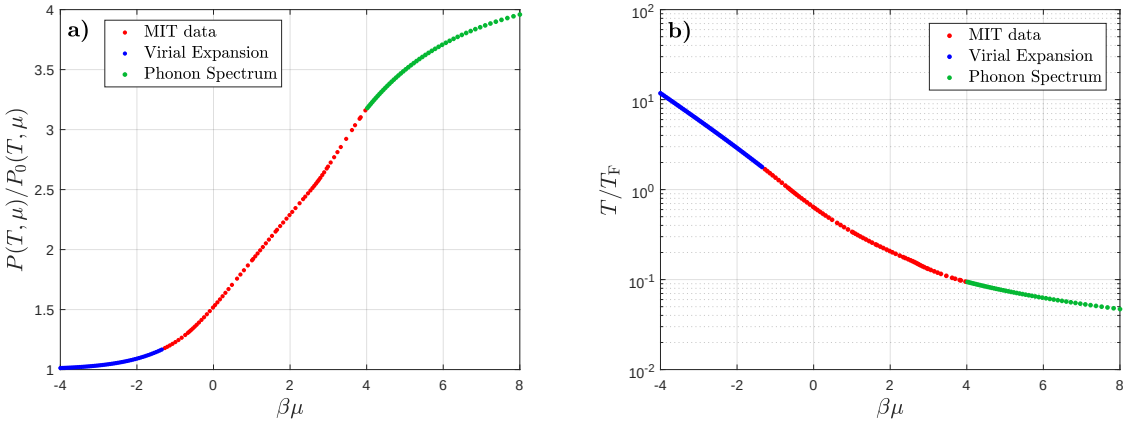

Figure 5.1: a) The dependence of the correction function as a function of $\beta\mu$. The red points are the experimental data from MIT. The blue points are Virial expansion in the high temperature limit to the third order. The dark green points are the extension at low temperature limit using the excitation spectrum (see text for details). b) The dependence of the local value of T/T_{F} as a function of $\beta\mu$, extended using the expansion in the high- and low-temperature limit.

Although the density profile in the strongly interacting regime is modified by the presence of interaction, we can still use the property of a gas at unitarity in order to extract the temperature. Since in the unitary regime, the only relevant energy scale is the Fermi energy, the fit function

can be related to that in the weakly interacting case, multiplied by a "correction function" that depends only on $\beta\mu$. In order words, the density profile of a unitary Fermi gas can be written as:

$$\overline{n}_u(z) = \frac{1}{\lambda_{\mathrm{dB}}^3}\frac{2\pi k_{\mathrm{B}}T}{m\omega_x\omega_y}\left[-\mathrm{Li}_{5/2}\left(-e^{\beta\mu(z)}\right)\right] \times \psi\left[\beta\mu(z)\right]. \tag{5.12}$$

Such a function constitutes the pressure equation of state (EoS) of a unitary Fermi gas, and has been first measured in our group [4] and later more precisely measured at MIT [5]. In particular, for a homogeneous system, for each value of $\beta\mu$, a ratio between the pressure of a unitary Fermi gas and an ideal Fermi gas is determined as shown in the left plot of Fig. 5.1. Since the pressure is directly proportional to the doubly integrated density [119], it essentially gives the ratio between the doubly integrated density of a unitary Fermi gas and an ideal Fermi gas.

Thanks to the thermodynamic relation

$$n = \left.\frac{\partial P}{\partial \mu}\right|_T, \tag{5.13}$$

one can also obtain the density EoS, with which one can extract the relation between T/T_{F} and $\beta\mu$, since

$$\frac{T}{T_{\mathrm{F}}} = \frac{4\pi}{(3\pi^2)^{2/3}}\frac{1}{(n\lambda_{\mathrm{dB}}^3)^{2/3}}. \tag{5.14}$$

The relation between T/T_{F} and $\beta\mu$ is shown in the right plot of Fig. 5.1.

High temperature limit In the high temperature limit, the pressure can be written as a sum of increasing powers of the fugacity:

$$P(\mu, T) = \frac{k_{\mathrm{B}}T}{\lambda_{\mathrm{dB}}^3}\sum_j b_j\left(e^{\beta\mu}\right)^j, \tag{5.15}$$

which is called the Virial expansion, where the coefficients $b_1 = 1$, $b_2 = 3\sqrt{2}/8$ [120] and $b_3 = -0.29095295$ [121] have either been determined analytically or numerically. We extend the MIT data by the third order Virial expansion in the high temperature regime as shown in the blue points in the left plot of Fig. 5.1. They connect very smoothly together. Also we see that the value of P/P_0 approaches 1 when $\beta\mu \to -\infty$, which means that the pressure of a unitary gas and that of an ideal Fermi gas, as we expected, become the same for high temperatures.

The relation between T/T_{F} and $\beta\mu$, in this high temperature regime, can be similarly obtained using Eq. (5.13) and Eq. (5.14). The extension with the MIT data (right plot in Fig. 5.1), as we see, is equally smooth.

Low temperature limit In the limit where $T \ll T_{\mathrm{F}}$, the temperature dependence of the energy of the gas can be approximated by elementary excitations present in the superfluid phase: boson-like Bogoliubov-Anderson phonons and fermion-like Bogoliubov quasi-particles. The energy contributions of these terms can be expressed as follows [122]

$$\epsilon_{\mathrm{ph+qp}}(n, T) = \frac{3}{5}nE_{\mathrm{F}}\left[\xi + \frac{\sqrt{3}\pi^4}{16\xi^{3/2}}\left(\frac{k_{\mathrm{B}}T}{E_{\mathrm{F}}}\right)^4 + \frac{5}{2}\sqrt{\frac{2\pi\Delta^3 k_{\mathrm{B}}T}{E_{\mathrm{F}}^4}}\exp\left(-\frac{\Delta}{k_{\mathrm{B}}T}\right)\right], \tag{5.16}$$

where $\xi = 0.376$ is the Bertsch parameter, E_{F} the Fermi energy for a given density n and Δ the gap of the system

$$\Delta \approx \left(\frac{2}{e}\right)^{7/3} E_{\mathrm{F}} \exp\left(\frac{\pi}{2k_{\mathrm{F}}a}\right). \tag{5.17}$$

In the unitary limit, $\Delta \approx (2/e)^{7/3} E_{\mathrm{F}}$ since $1/k_{\mathrm{F}}a \to 0$.

Knowing the thermodynamics relation for the entropy s and the free energy f,

$$\begin{aligned} s &= \int_0^T \frac{\mathrm{d}T'}{T'} \frac{\partial \epsilon}{\partial T'}, \\ f &= \epsilon - T \cdot s, \end{aligned}$$

where the energy $\epsilon = \epsilon_{\mathrm{ph+qp}}$ given by Eq. (5.16), for given values of T and T/T_{F}, we can calculate the corresponding values of $\beta\mu$ and the pressure P:

$$\beta\mu = \frac{1}{k_{\mathrm{B}}T}\left(\frac{\partial f}{\partial n}\right), \tag{5.18}$$

$$P = \frac{2\epsilon}{3}. \tag{5.19}$$

Using these quantities we can extend the curve P/P_0 as a function of T/T_{F} to the low temperature side, as shown in the green points in Fig. 5.1.

We show in Fig. 5.2 the simulated one dimensional cloud profiles for different values of T/T_{F} at the center of the trap. We observe no obvious difference between the two density profiles when the cloud is far from degenerate. When the temperature is decreased, the density profile of a unitary gas becomes peakier and deviates from the non-interacting case, which is a direct signature of the attractive character of the interactions.

5.2 Experimental procedure and results

Experimentally we follow the same intensity ramps as we presented in the previous chapter to go to lower power values. At each step of the evaporation, we take *in situ* images of the cloud and we extract the temperature T as well as the degeneracy in terms of T/T_{F} at the center of the cloud as shown in Fig. 5.3.

5.2.1 EoS fit vs. TOF measurement of the temperature

In order to confirm the validity of the fit, we compare the measured temperature from the EoS fit to the measured temperature using the time-of-flight expansion (Fig. 5.4), for relatively high powers of the ALS beam as the end of evaporation.

Fig. 5.4 shows that the temperature measured using both methods are globally in very good agreement. Slight discrepancies, however, are seen in higher temperatures. This is because at high temperatures the cloud has longer axial extension and explore the region where the trap is not exactly harmonic. In this regime, the EoS fit is not precise. At low temperatures (close to but above degeneracy), the agreement of the two measurement is excellent.

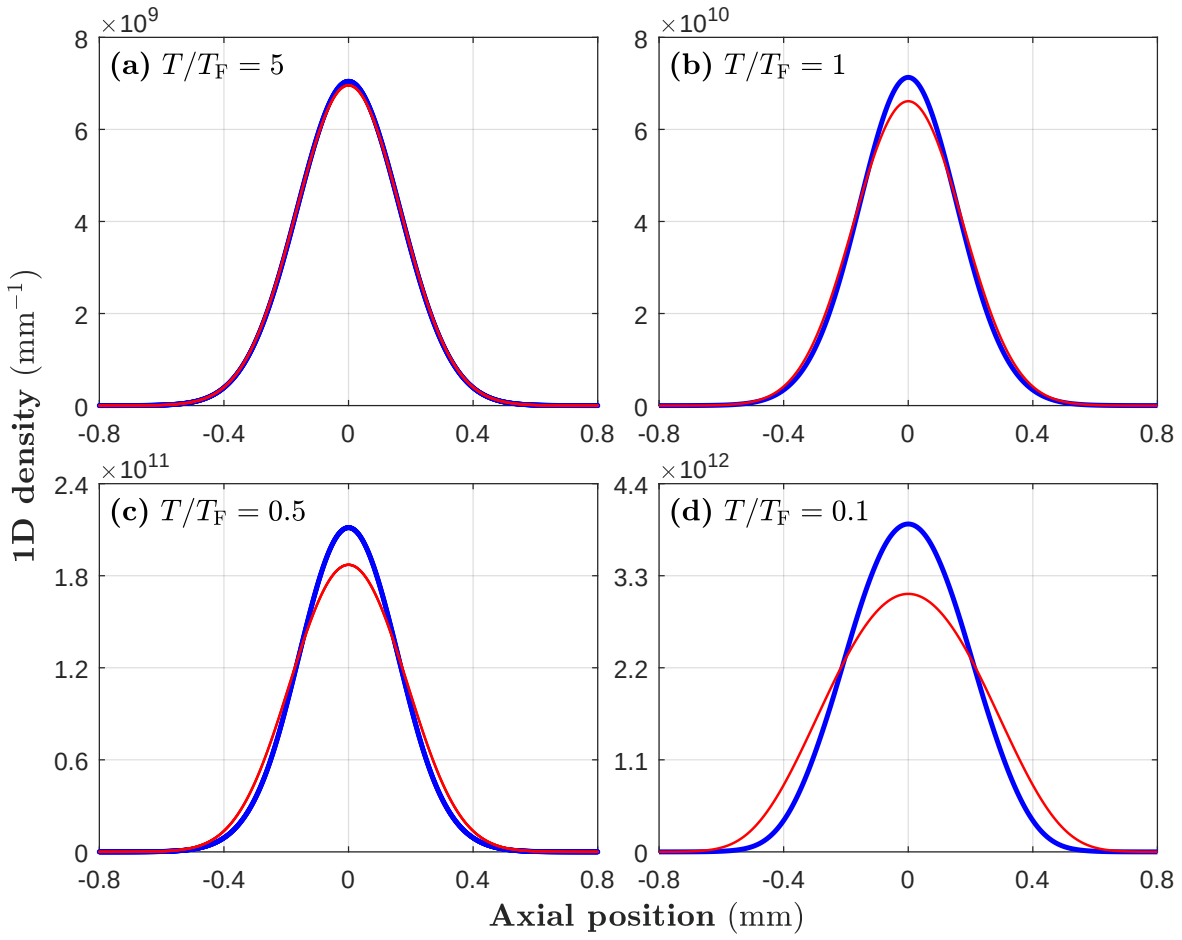

Figure 5.2: The simulated strongly interacting (in blue) 1D cloud profiles using equation 5.12 for different degrees of degeneracy: a) $T/T_F = 5$, b) $T/T_F = 1$, c) $T/T_F = 0.5$ and d) $T/T_F = 0.1$. We also plot (in red) the 1D cloud profiles for an ideal gas, with the same atom number and temperature using Eq. (5.12) for comparison. we see that for an increasingly degenerate Fermi gas, the profiles become narrower than their non-interacting counterparts. The parameters for the trap are chosen as $\omega_x = \omega_y = 2\pi \times 1\,\mathrm{kHz}$, $\omega_z = 2\pi \times 25\,\mathrm{Hz}$.

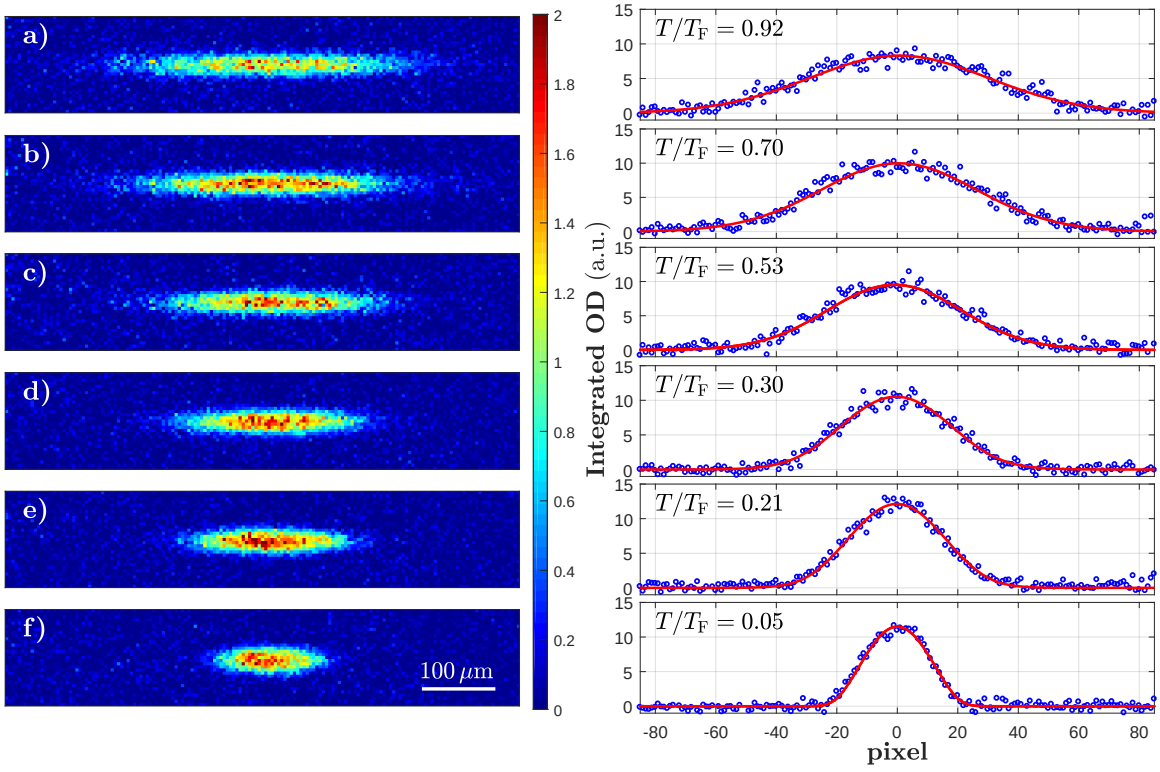

Figure 5.3: Cloud in the ALS trap at different stages of evaporation: a) $P_{\mathrm{ALS}} = 320\,\mathrm{mW}$; b) $P_{\mathrm{ALS}} = 260\,\mathrm{mW}$; c) $P_{\mathrm{ALS}} = 180\,\mathrm{mW}$; d) $P_{\mathrm{ALS}} = 110\,\mathrm{mW}$; e) $P_{\mathrm{ALS}} = 70\,\mathrm{mW}$; f) $P_{\mathrm{ALS}} = 30\,\mathrm{mW}$. The data on the right panel are the doubly integrated density profiles corresponding to the images on the left panel. The red curves are the EoS fits, from which one can deduce the values of T/T_{F} at the center of the trap. We observe the increase in OD at the center of the trap in the course of evaporation. At the end of evaporation we typically end up with $2.4(2)\times10^4$ atoms per spin state with $T/T_{\mathrm{F}} = 0.06(3)$. Image taken in the "Img 2" direction as depicted in Fig. 4.8.

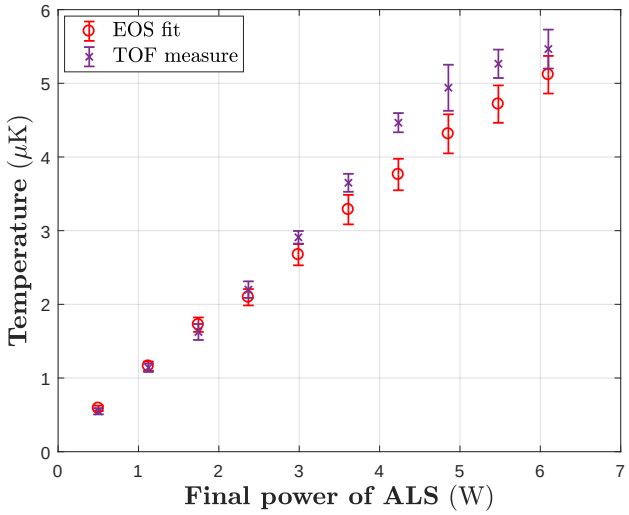

Figure 5.4: Temperature of the cloud measured using the EoS fit (red circle) and the time of flight expansion (purple star). The agreement of the two curves converges at low temperature. For the lowest temperature the corresponding $T/T_{\mathrm{F}} \sim 3$, which means the gas is still in the classical regime.

At even lower temperatures (not shown on Fig. 5.4), we expect the two data to differ again, as the TOF expansion will give a measure of the release energy rather than the temperature itself. In this case, the TOF expansion is no longer a trustworthy way to measure the temperature and one should rely on the EoS fit instead.

5.2.2 Evaporation performance

Following the evaporation in the single ALS beam, when decreasing the beam power to roughly 350 mW we reach the degenerate regime ($T/T_{\mathrm{F}} < 1$). The deeply degenerate regime ($T/T_{\mathrm{F}} < 0.2$) is attained when the power is further decreased to 70 mW. In the end, we decrease the power of the ALS to 30 mW to obtain a deeply degenerate unitary Fermi gas with $T/T_{\mathrm{F}} = 0.06(3)$ for typically $2.4(2) \times 10^4$ atoms per spin state[(b)]. The evolution of atom number, temperature, and degeneracy parameters are shown in Fig. 5.5.

5.3 Fermionic superfluidity

5.3.1 Superfluid transition

Superfluidity in fermionic states of matter is closely linked to pairing. On the two-particle level, pairing implies the existence of a bound-state in the inter-particle potential. However, for a many-body system, pairing can occur without two-particle bound-states, as was first discovered by Cooper [10]. Cooper-pairs, consisting of weakly-bound fermions of opposite spin and momentum, feature a length scale that greatly exceeds the inter-particle spacing.

[(b)]Note that we do not aim for high atom numbers on this experiment, as the samples will be probed under a microcope eventually.

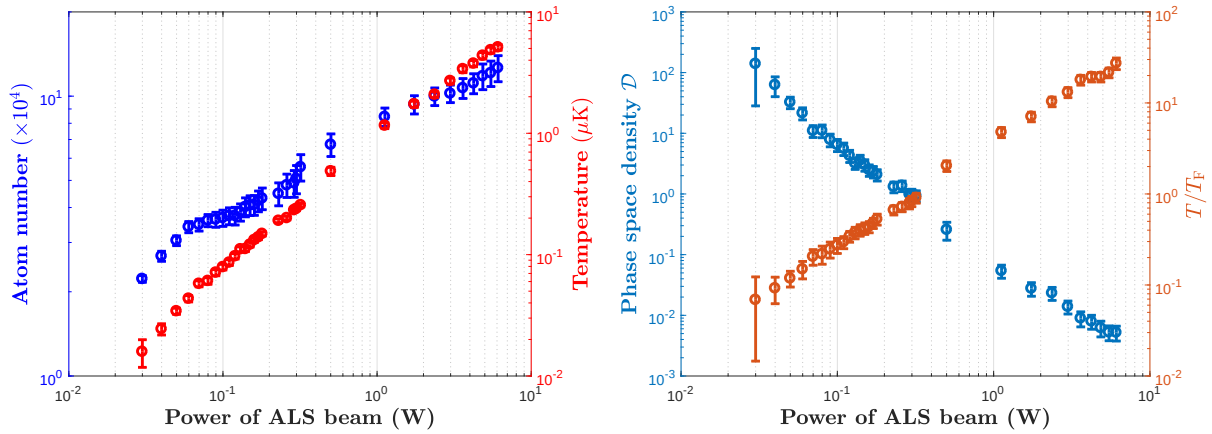

Figure 5.5: Left: The atom number (per spin state) and temperature evolution in the ALS beam till degeneracy. Right: The phase space density and the local T/T_F value measured using EoS fit.

While at zero-temperature, the system always forms a superfluid, irrespective of the underlying nature of the pairs, the signatures of superfluidity vastly differ for the two limits of tightly bound molecules and long-range cooper pairs. Well established techniques for bosonic systems such as the measurement of the condensate fraction through the momentum distribution only work for the molecular fermionic superfluid [38, 40, 123, 124].

In this thesis, most experiments were performed at unitarity, which lies in the crossover regime between the two pairing limits. Therefore, a simple detection of superfluidity through the presence of a condensate peak in the momentum distribution is not possible. In our experiments, we produce routinely atomic gases with $T/T_F = 0.06(3)$ at unitarity, which is well below the known transition of $T_c/T_F = 0.17$ [4, 5]. While the thermometry method employed by us is well-established in the research field and typically yields reliable results, we nevertheless aim at the measurement of an independent signature of condensation, which is synonymous to superfluidity in 3D.

The question of how to identify a condensate fraction in a strongly interacting Fermi gas, nevertheless, is not easy, and was the subject of intense research. In the following, we discuss several methods that have been used in the past.

5.3.2 Experimental methods to probe superfluidity

Rapid ramp

The rapid ramp technique is first developed in the JILA group [42] on ^{40}K and later adapted by the MIT group [41] on ^{6}Li. The basic idea is to prevent the fermion pairs formed at unitarity to dissociate by quickly sweeping towards the BEC side.

This method not only allows one to reveal the momentum distribution at unitarity, but across the whole BEC-BCS crossover region as shown in Fig. 5.6, which reveals the double structure as the signature of a BEC[(c)]. However, this method allows for qualitative evaluation but does

[(c)]Note that this method proves the gas is a molecular BEC, not directly its superfluidity, since Bose-Einstein

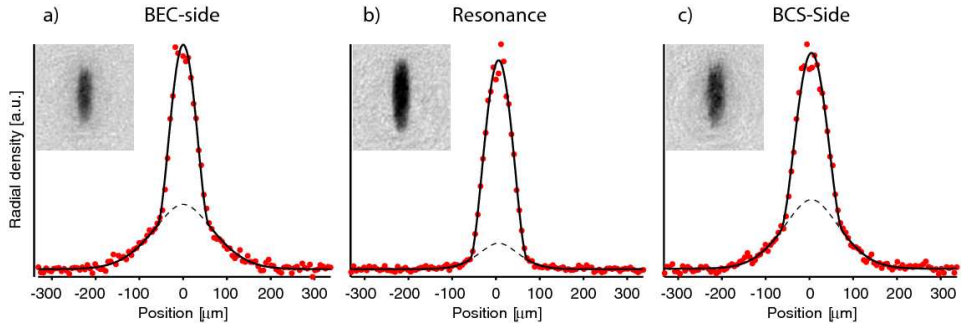

Figure 5.6: The rapid ramp technique that reveals the bimodal distribution of a fermionic pair condensate across the Feshbach resonance. Taken from [125].

not allow for adequate quantitative measurement, since the rapid ramp does not necessarily conserve the condensate fraction before and after the field ramp.

Vortices lattice

Direct observation of superfluidity is the formation of quantized vortices or vortex arrays after stirring the cloud to excite surface excitations, as shown in Fig. 5.7. This is a direct proof of superfluidity since only superfluid with appropriate excitation can host such vortex lattices.

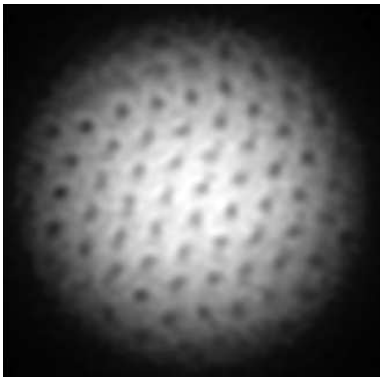

Figure 5.7: Vortex lattice excited in a ultracold Fermi gas at unitarity. Taken from [47].

Spin imbalance

The technique that we present in the following, in the framework of this thesis, involves introducing a population imbalance between the two spin states [126]. In fact, for a sufficiently cold imbalanced Fermi gas, there exists a superfluid core, where the two spin species are fully paired ($n_1 - n_2 = 0$). Using the Gibbs-Duhem relation $n_i = \partial P_i / \partial \mu_i$ (i=1,2), inside the core,

$$\frac{\partial P_1}{\partial \mu_1} - \frac{\partial P_2}{\partial \mu_2} = 0. \tag{5.20}$$

condensate does not always necessarily implies superfluidity. In three dimensional space, however, the two happens at the same time.

Since the pressure P_i is proportional to the integrated density $\overline{n}_i$ and in the axial line

$$\frac{\partial}{\partial \mu_1} = \frac{\partial}{\partial \mu_2} = -\frac{1}{m\omega_z^2 z}\frac{\partial}{\partial z}, \tag{5.21}$$

then combining the above two equations we have

$$\frac{\partial(\overline{n}_2 - \overline{n}_1)}{\partial z} = 0. \tag{5.22}$$

This means that in the central region of a spin-imbalanced superfluid, the difference of the doubly integrated density profiles of the two spin species shows a plateau[(d)].

5.3.3 Implementing spin imbalance

Implementing a spin imbalance in our experiment is very easy, since we can control the spin populations at the beginning of the evaporation with an RF sweep, as presented in the previous chapter. By varying the RF sweep speed, we can thus control the spin imbalance between the two spin states at the end of the evaporation.

Since the evaporation is a non-linear process, the spin imbalance we introduce also affects the efficiency of the whole evaporation. If the gas is too polarized in the beginning, it is possible that it becomes totally polarized during the evaporation before reaching degenerate regime. This means one must carefully choose the RF sweep duration to have a proper spin-imbalance for revealing the existence of a superfluid core.

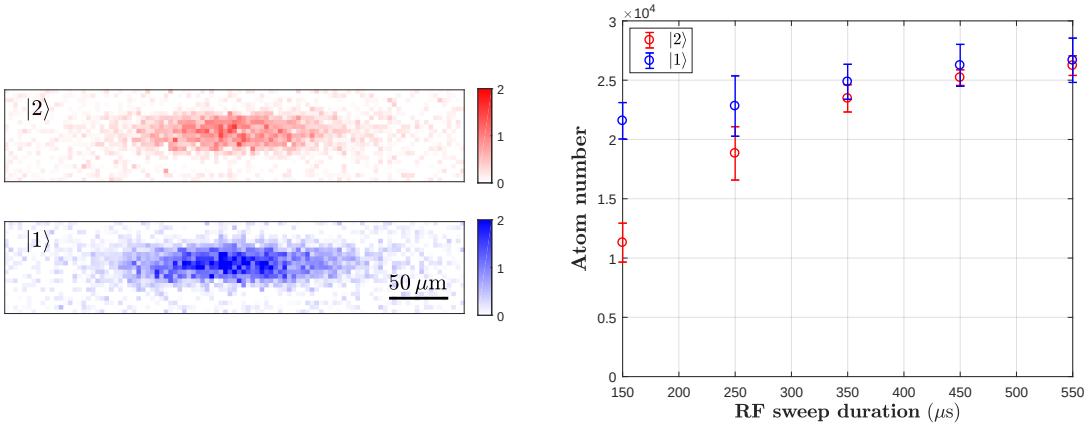

Figure 5.8: Left: Images taken for the two spin states $|1\rangle$ and $|2\rangle$. In this shot there are approximately twice as many atoms in spin state $|1\rangle$ than in spin state $|2\rangle$. Right: Atom numbers for the two spin states at the end of evaporation with $P_{\mathrm{ALS}} = 30\,\mathrm{mW}$, as a function of the RF sweep duration applied at the start of the evaporation.

[(d)]Note that this method is also not a direct proof of superfluidity. This method only shows there are equal number of atoms in the core region, and, as a result, is a proof of pairing. On top of that, it has been shown that only in the region where the spin difference shows a plateau that one can excite vortices [127], which confirms the superfluidity in the region where a plateau in density difference is present.

Double spin imaging

At high field, the detuning between imaging frequencies for the two spin species is about 80 MHz. In order to be able to image the two spin states at high field *in situ*, we use the camera in the double shutter mode. This mode allows the camera to take two successive shots with a minimum of 1 μs time lapse between them. In practice, we take two images with two light pulses resonant with the imaging transition for the two spin species respectively of the same duration 7 μs. The two imaging pulses are lapsed with a interval of 3 μs.

Typical *in situ* images of the double spin species are shown in Fig. 5.8. By controlling the duration of the RF sweep, we can achieve easily almost twice as many atoms in the majority spin state as in the minority spin state at the end of evaporation.

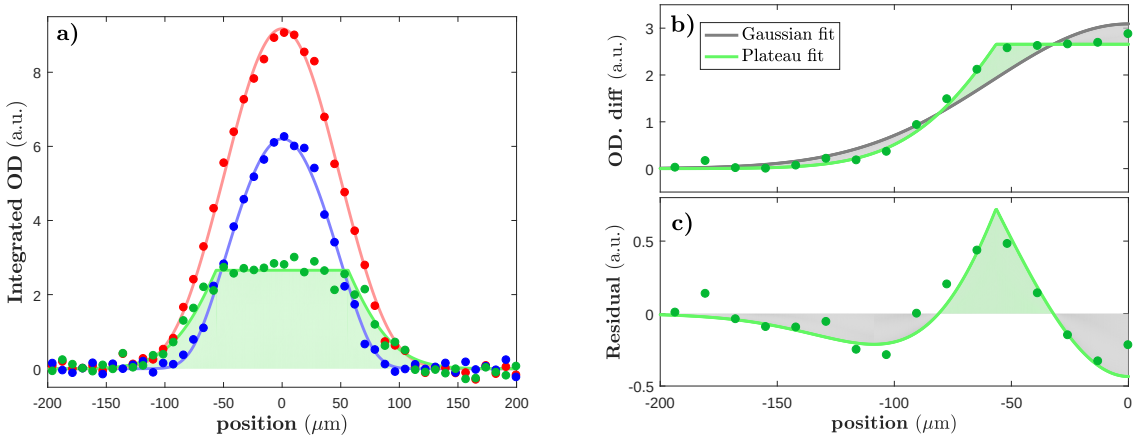

Figure 5.9: a): The difference (green dots) of the doubly integrated density profiles of the two spin species (red and blue) shows a plateau in the central region. The ALS beam power at the end of the evaporation is $P_{\mathrm{ALS}} = 30$ mW. The presented data is an average of 40 identical images in order to decrease the noise level. The plateau in the population difference is clearly present. The lines in the picture are for guide-to-the-eye purposes only. b): More quantitative approaches to be convinced of the presence of a plateau. We fit the population difference (on the left side of the picture) with a gaussian (gray curve) and a gaussian with central plateau (green). The data points follows the green curve clearly much better than the gray curve. c): we compute the residual between the data and the gaussian fit (gray curve in b). We see systematic deviation from the gaussian fit at the center and around the "shoulder" of the plateau. And this deviation can be very well followed by the green curve, which is the difference of the two fit curves in b).

5.3.4 Superfluid plateau

In Fig. 5.9, we show a plateau for the difference in the doubly integrated density profiles at the end of evaporation with $P_{\mathrm{ALS}} = 30$ mW, with the population of the majority species being $N_1 = (2.0 \pm 0.2) \times 10^4$ and the minority species $N_2 = (1.2 \pm 0.1) \times 10^4$. This region where a plateau is present corresponds to the region where the individual atoms form pairs. The link between the density difference plateau and superfluidity was demonstrated at MIT in experiments combining spin imbalance and vortex lattices [127].

More quantitative analysis for the presence of the plateau can be performed by fitting the difference with a simple gaussian and a plateaued gaussian in the center[(e)], respectively. By computing the residual between the data and the gaussian fit, systematic deviation is found as we see in Fig. 5.9 c) and can be well described by the difference of the two fits.

5.4 Summary

In this chapter, we have presented the production of a deeply degenerate Fermi gas in the strongly interacting regime. A quantitative method using the EoS is applied to characterize the degree of degeneracy of the obtained sample. We are able to produce deeply degenerate Fermi gases with $2.4(2) \times 10^4$ atoms per spin state with temperature as low as $0.05\,T_{\mathrm{F}}$.

Furthermore, we have been able to imbalance the spin population of the sample in a well-controlled manner and with it, provide a first proof for superfluidity in such an imbalanced Fermi gas.

[(e)]Note that the wings of the density difference is, in principle, not a simple gaussian. The totally polarized phase being a non-intereacting Fermi gas, its doubly integrated profile can be described by Eq. (5.5). But the density profile of the polaron phase between the superfluid core and the normal phase cannot be simply described by a given expression. The plateaued gaussian fit here is simply for illustrating the existence of a central plateau and should not be used as a quantitative formula.

Chapter 6

Towards single atom imaging of a unitary Fermi gas

In this chapter, we describe the ongoing work towards the study of strongly interacting Fermi gases, using a quantum gas microscope with single atom resolution.

We start with an overview of quantum gas microscopy and its applications. Then we present our design for applying this technique on a bulk system composed of strongly interacting fermions. In particular, we present the hardware including the pinning lattice setup and the high resolution objective. At the end, we explain the principle of Raman sideband cooling - the laser cooling technique in a deep lattice that we intend to apply to achieve the goal of single atom imaging.

6.1 State of the art

In a quantum gas microscope, utracold atoms are pinned in space by an optical lattice, and imaged with a high resolution objective, which gives access to the individual atom position information, at the scale of a single lattice site. This technique was first realized with bosonic ^{87}Rb, and allowed the space-resolved study of the superfluid to Mott insulator transition [58, 59]. It also proved a powerful tool for the study of spatial dynamics and correlations [128]. The single-atom imaging of ultracold fermions, which is more challenging, was realized with fermionic species ^{40}K and ^{6}Li a few years later [60–64]. Once again, it allowed unprecedented access to the physics of fermions in a lattice, allowing the study of equilibrium [31] or out-of-equilibrium [129] properties and the measurement of density and spin correlations [81, 130].

The single atom imaging of individual atoms presents two main challenges. First, the imaging system must be able to resolve the typical lattice spacing, which is of several hundreds of nanometers. Since the atoms are placed in the periodic structure of the lattice, the identification of their position is facilitated, and a resolution of the order of the lattice spacing is sufficient. This nevertheless requires the use of a high-aperture objective.

The second challenge is to collect enough information about the position of the atom without disturbing them. The imaging technique of choice so far has been fluorescence imaging, for which high signal-to-noise ratios can be achieved. However, in order to collect enough fluores-

cence photons while maintaining the atoms in their respective sites in spite of the recoil energy, the fluorescence process must be combined with a laser cooling technique[(a)].

In the following we will present why and how we plan to implement single-atom imaging of atoms in our experimental setup.

6.2 Quantum gas microscope on a bulk Fermi gas

Quantum gas microscopes have only been used so far to study lattice physics of bosons or fermions: before performing imaging, the atoms were already evolving in low-energy bands of an optical lattice (which can be the same as, or different from the one used to pin them in space for imaging). A highly interesting perspective is to extend this technique to the study of a bulk system. Of particular interest here are the strongly interacting Fermi gases we can produce in our setup: a microscope would allow to probe directly the correlations and complex dynamics of this truly N-body problem, where correlations exist between all particles.

The goal of our experiment is then to measure, with a quantum gas microscope, density and spin correlation functions across the BEC-BCS crossover. These correlations are of course difficult to obtain on the bulk. For instance, the measurement of the contact[(b)], has required several attempts and involved a variety of indirect probes [50, 53, 54, 56, 57] before a satisfactory quantitative picture was reached for the unitary gas. With a quantum gas microscope, direct measurements can be obtained, for a whole range of distances. It can, for example, allow direct access to the build-up of correlations across the superfluid transition, or to the spin correlations that should arise in a polarized (imbalanced) Fermi gas, in the so called FFLO phase.

In order to realize such a microscope apparatus, with single-site resolution, we have to achieve three main requirements:

- Atoms are pinned down in position for imaging: this requires a three dimensional optical lattice, which allows us to "project" the atoms on individual sites, and in which we can then perform fluorescence imaging,

- High resolution imaging: this requires a *high-aperture* imaging system, which will typically have a *short depth of focus*. In order to image the atoms, we will have to select a 2D plane of the pinning lattice, in the imaging plane of the objective.

- Fluorescence extraction and cooling: we need to collect fluorescence from the atoms, while cooling them in order to prevent hopping in the lattice.

In the following, we present the current progress towards achieving these requirements.

[(a)] With the rare exception of heavy atoms like Ytterbium [131].

[(b)] The quantity of the contact C is proportional to the short range limit of the density-density correlation function and is defined as

$$\langle n_\uparrow(0) n_\downarrow(r)\rangle \xrightarrow{r\to 0} \frac{C}{16\pi^2 r^2},$$

where r is the distance between two particles with different spins.

6.2.1 Pinning lattice

As explained above, we have to isolate a 2D plane of atoms in the focal plane of the objective, and freeze them in space on this plane. For this reason the pinning lattice is composed of a 2D horizontal lattice setup combined with a 1D vertical lattice setup. The main interest in our design of these setups is to obtain a sufficiently large potential depth $U_{\max}$ and a lattice spacing a compatible with imaging setup.

Two-dimensional pinning lattice setup

With the laser power available (45 W ALS at λ_L =1064 nm), we have considered a number of options about the geometry of the pinning lattice setup. At last, we decided to implement a triangular lattice instead of a standard square lattice, since a triangular lattice setup would allow for a larger lattice depth and a resolution more adaptable to the planned objective. Details of the design and setup of the pinning lattice can be found in [132].

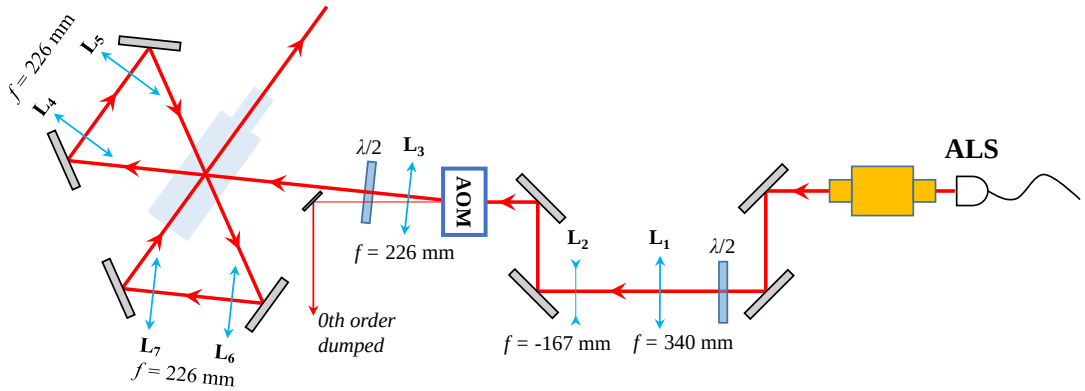

Figure 6.1: The simplified pinning lattice setup.

The setup of the pinning lattice is presented in Fig. 6.1. The laser beam goes through an AOM and can be rapidly switched on and off. The diffracted order of the beam is focused in the science cell with a waist of 70 μm, and reflected twice to create a triangular lattice geometry. Due to practical choices, the angle between the three beams are close to but not exactly 120°. The effective depth of the lattice is $k_B \cdot 2.2$ mK and a lattice spacing of $a = 710$ nm, which is comparable to the resolution of the objective that we will present in section 6.2.2.

Vertical 1D lattice

The depth of the focus for the high resolution objective is typically several μm. This is much smaller than the typical size of the cloud after evaporation, which is on the scale of several tens of μm. Therefore, it is necessary to select one slice of the atoms, at the μm scale, before performing single atom imaging.

The setup intended for this purpose is a vertical 1D lattice, which involves two counter-propagating beams[(c)], leading to a separation of $a_z = \lambda_L/2 \approx 530$ nm. This length determines

[(c)] A scheme where the vertical lattice is realized via two angled beams is also being studied at the moment.

the vertical length scale of a slice of cloud confined in such a lattice, and is smaller than the previously mentioned depth of focus.

In addition, in order to select this single plane of atoms while removing the other planes, we plan to use magnetic gradients provided by the curvature coils or the Feshbach coils, combined with a microwave transfer technique [133].

Additional comments on the lattice filling

For probing a superfluid Fermi gas in the unitary limit, ideally it is desirable to reach temperatures of $T \approx 0.1\,T_{\mathrm{F}}$. In this regime, a compromise has to be made concerning the density of the cloud: On the one hand, a dilute cloud would decrease the chance of having more than one atom per site and hence avoid their loss through light-assisted collisions during imaging [134]. Also, a dilute cloud has the benefit of allowing for several empty sites between two occupied ones, so that the extracted correlation functions are not subject to the discretization introduced by the lattice; On the other hand, since the Fermi temperature is directly linked to density, in order to produce deeply degenerate Fermi gas at $T \approx 0.1\,T_{\mathrm{F}}$ that is dilute, the absolute temperature has to be ultralow, which is not always straightforward to achieve experimentally. Nevertheless, as we will see below, the current performances of the experiment are very promising in this regard.

The Fermi temperature T_{F} of our atomic cloud in the superfluid regime or in the vicinity of the transition, typically ranges from 100 nK to 300 nK at the center of the cloud. With such a Fermi temperature we can compute a density

$$n_0 = \frac{(2mk_{\mathrm{B}}T_{\mathrm{F}})^{3/2}}{3\pi^2\hbar^3},$$

which equals to $n_0 = 0.14\,\mu\mathrm{m}^{-3}$ for $T_{\mathrm{F}} = 100\,\mathrm{nK}$. The corresponding inter-particle distance is then $d = n_0^{-1/3} = 1.95\,\mu\mathrm{m}$.

In each plane, the Wigner-Seitz cell for a triangular lattice is a hexagon and has an area of $A \equiv 2\lambda_{\mathrm{L}}^2/3\sqrt{3}$. The adjacent plane is separated by a_z and has an unit volume of $A \cdot a_z$. Therefore, the average site occupancy is $A \cdot a_z \cdot n = 3\,\%$.

This means that 3% of the total number of atoms will occupy the same lattice site and get lost due to light-assisted collisions during Raman sideband cooling, which is in general acceptable[(d)].

6.2.2 High resolution objective

Specs of the microscopes

The high resolution objective is a custom objective from Special Optics. it has a working distance of 15 mm and an effective focal length (EFL) of 27 mm. The numerical aperture of the objective is NA=0.55.

[(d)] Note that, in this estimate, we ignore the effect of Pauli's principle, which will spread further the atoms of the same spin, and the effect of interactions which will bring closer atoms of opposite spins.

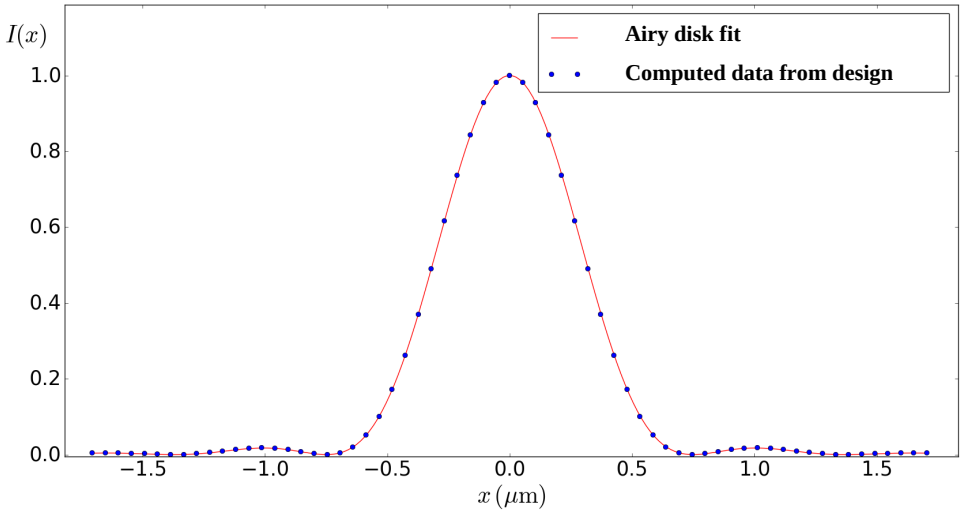

Figure 6.2: Computed point spread function of the objective. The Airy disk fit gives a resolution of $\delta = 0.75\,\mu$m.

The resolution of such a objective is given by the size of the point spread function, with the following mathematical form:

$$I(r) = I_0 \left[\frac{2J_1(\tilde{r})}{\tilde{r}}\right]^2, \tag{6.1}$$

where $\tilde{r} \equiv \pi r/(\lambda N)$ and J_ν is the Bessel function of the first kind. Here r is the radial distance from the optical axis in the focal plane and $N = R/d$, then ratio between the observation distance R and d the aperture diameter. The resolution of the optical system is given by the first zero of such a function, which corresponds to $\tilde{r} \approx 3.8317$, which gives the resolution $\delta = 1.22\lambda N$.

Shown in Fig. 6.2 is the computed point-spread function (PSF) of a point source for the given objective. The fit yields a resolution of $\delta = 0.75\,\mu$m, which is comparable to the pinning lattice spacing, $a = 710\,$nm.

Preliminary test

In a first test setup, we have measured the resolution of the objective using a pinhole, with a diameter of $0.5\,\mu$m.

The measurement is shown in Fig. 6.3. A fit using the diffraction limited Airy disk yields a resolution of $\delta_m = 0.98\,\mu$m. This result is larger than the computed value of $0.75\,\mu$m. The reason for this deviation is probably due to the size of the pinhole, which has a relatively large uncertainty of $0.1\,\mu$m on the diameter due to manufacture process. Furthermore, the focusing lens used in combination with the objective in this test is not in accordance with the desired specifications for our final setup [135]. Further tests of the objective will take place soon in more optimal conditions but the result of this preliminary test is promising.

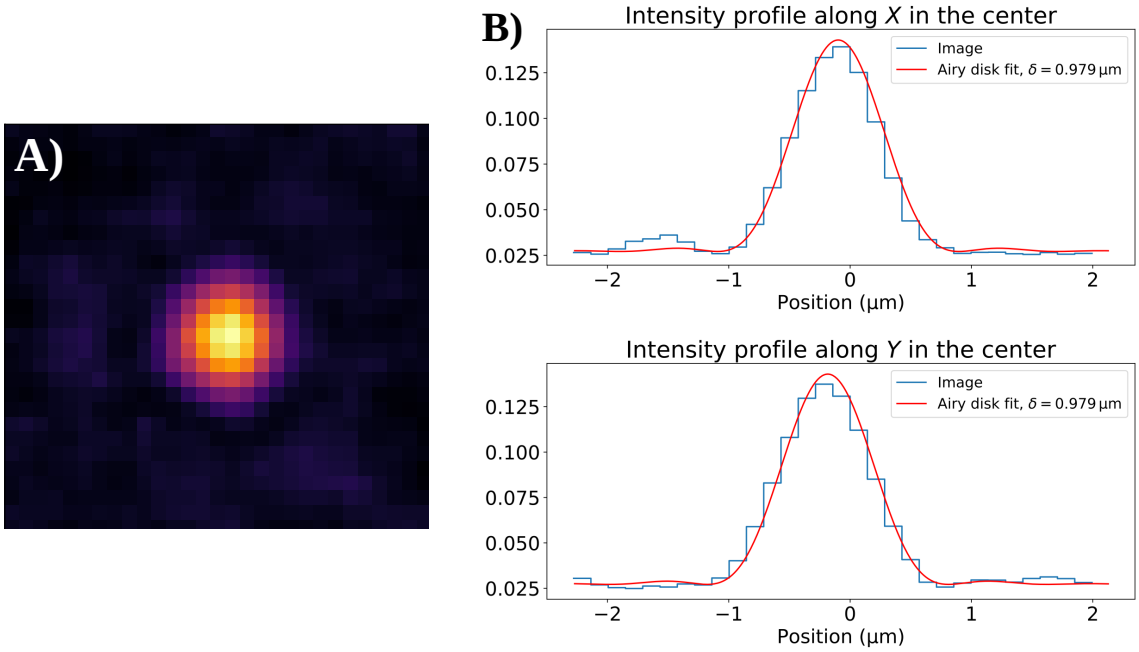

Figure 6.3: A): The image of the pinhole on the camera. B): The intensity profile fit using diffraction limited Airy disk function in the x and y direction. Both fits yield a resolution of $\delta_m = 0.98\,\mu$m.

Choice of the magnification

The magnification of the imaging system directly determines over how many camera pixels the PSF is distributed. On the one hand, it is not desirable to have a PSF which spreads over too many pixels, since then each pixel will have very few photon counts. On the other hand, if the PSF concentrates on only one or two pixels, it is more likely to be mistaken for noise, and the determination of its position is less precise.

Indeed, if we have a point source emitting light and we collect n photons during unit time τ using the objective, the integration of the intensity profile in the observation plane of such a point source should give the optical power P. In other words,

$$\begin{aligned} P = nh\nu/\tau &= \iint_S I(r)\mathrm{d}S \\ &= \int_0^{2\pi} \mathrm{d}\theta \int_0^{\infty} I(r) r \mathrm{d}r, \end{aligned}$$

where $h\nu$ is the energy of a single scattered photon, and $I(r)$ the point spread function introduced before.

The result of the integration gives the relation between the collected optical power P and the intensity I_0 at the center of the point spread function

$$P = \frac{I_0}{\pi}(2\lambda N)^2 = 0.855 I_0 \delta^2. \tag{6.2}$$

If the magnification of the system is M, on the camera plane the point spread function is magnified by a factor M, and the central intensity is accordingly attenuated by a factor M^2. In other words, on the imaging plane,

$$P = 0.855 I_0^{(R)} \times \Delta^2, \tag{6.3}$$

with $\Delta = M\delta$ the resolution on camera and $I_0^{(R)} = I_0/M^2$ the center intensity on the camera.

The number of photons hitting on the pixel with size S_{pix} at the center of the PSF during duration τ is hence

$$n^{(c)} = \frac{I_0^{(R)} S_{\text{pix}} \tau}{h\nu} = \frac{n S_{\text{pix}}}{0.855 M^2 \delta^2}. \tag{6.4}$$

And with this number we can compute the statistical noise at the central pixel of the PSF, which is given by $1/\sqrt{n^{(c)}}$.

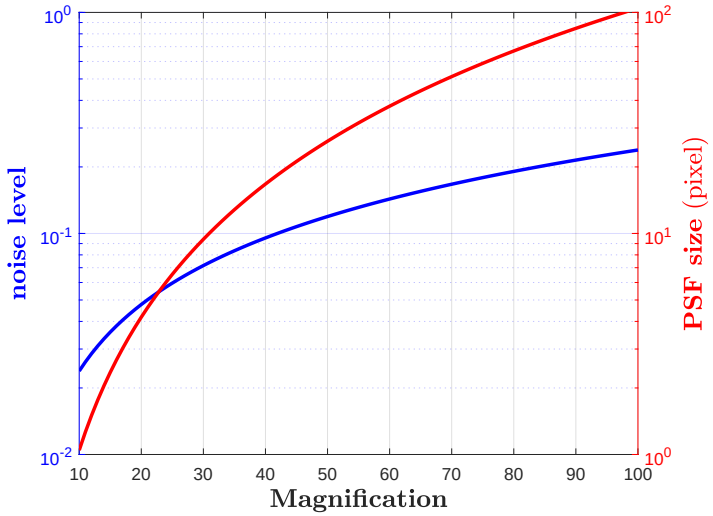

Figure 6.4: The noise level at the center of the PSF and the PSF size as a function of the magnification M, for a duration of fluorescence collection of 1 s and assuming a number of 500 photons collected per atom during this time.

The camera we plan to use[(e)] has a very high quantum efficiency $\eta \approx 0.95$ and a pixel size of $S_{\text{pix}} = 13\,\mu\text{m} \times 13\,\mu\text{m}$. According to already existing quantum gas microscopes [61, 62, 64], the objective typically collects several hundred photons per second per atom. And finally, the resolution of the objective being $\delta = 0.75\,\mu$m, we can plot the noise level (for 1 s of fluorescence collected) and the PSF size in terms of magnification in Fig. 6.4. Here the PSF size is the size of the disk with radius $M\delta$ in terms of pixel numbers.

In practice, apart from the statistical noise, there is also electronic noise and noise induced by stray light[(f)], which is not taken into consideration here. We see from the graph that a reasonable choice of the magnification is around $M = 40$, where the statistical noise is only around 10% and a single PSF spans over 10 to 20 pixels, which means that the PSF occupies 3 to 5 pixels in one dimension.

[(e)] Andor iXon

[(f)] The actual electronic noise for Andor iXon is very low, typically less than 1 count per pixel in the exposition time we consider here. The noise induced by the stray light, however, is *a priori* difficult to quantify.

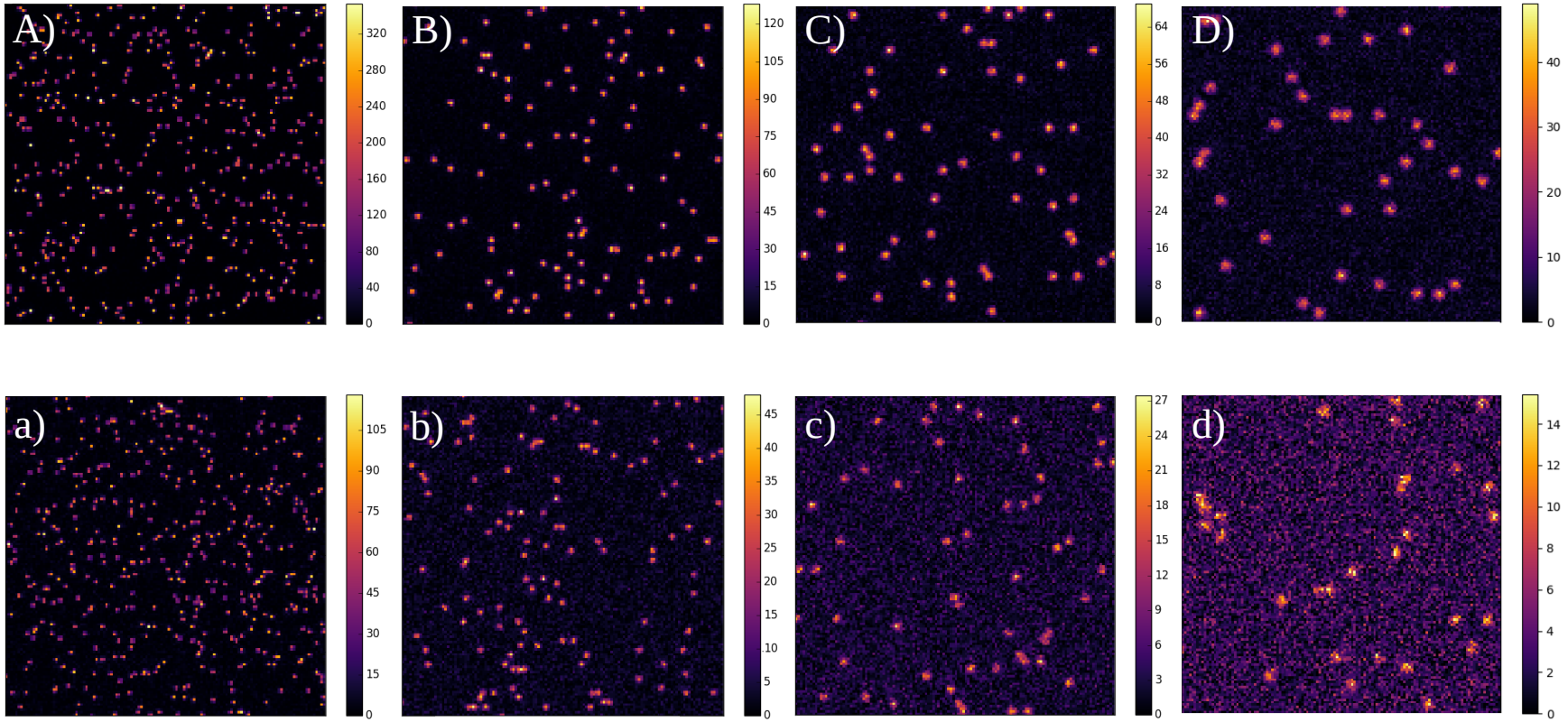

Figure 6.5: Simulated images for different magnifications and number of photons collected per atom. The whole camera chip is composed of 1700×1700 pixels. A)- D): for 500 photons collected per atom, with a magnification of $M = 20$ (A), $M = 40$ (B), $M = 60$ (C) and $M = 80$ (D). a)-d): The same magnification values but for only 150 photons collected per atom. The noise level here is purely the statistical noise due to photon counts. Pictures taken from [135].

A simulation about the quality of the images is presented in Fig. 6.5 with magnification ranging from 20 to 80, with a density given by $n_0 = 0.14\,\mu\text{m}^{-3}$, for 500 photons collected per atom (top row) and 150 photons collected per atom (bottom row), respectively. These images show that for more than 150 photons collected per atom, it is possible to identify single atoms with high fidelity, as is possible by the eye. When the collected photon number decreases, the quality of the image deteriorates especially for large magnifications, as the PSF is spread on more pixels and relative noise is higher (Fig. 6.5 D and d).

6.2.3 Raman sideband cooling

Fluorescence imaging gives excellent signal-to-noise ratio and has proven to be a successful strategy for imaging single atoms in optical lattices. However, the successive scattering of photons by each atom on a lattice site can lead to heating, causing the atom to get in higher lattice bands and eventually leave the trap. Hence some cooling mechanism is necessary during the imaging process.

For the first quantum gas microscopes with Rubidium, polarization gradient molasses cooling was implemented for cooling and imaging ^{87}Rb [58, 59]. However, this method is not suitable for fermions like ^{6}Li and ^{40}K, given the unresolved nature of the hyperfine states. Gray-molasses cooling has been demonstrated to work for ^{6}Li, both in free space and in a dipole trap [111], but not yet been extended to the application of a deep optical lattice.

For the fluorescence imaging of fermions, this has led to the use of two-photon techniques, either Raman sideband cooling [61, 62, 64, 84] or EIT cooling [60, 63]. Since they rely on coherent two-photon processes, far-detuned from the excited state, the unresolved excited state structure is less of a problem.

Raman sideband cooling has been successfully demonstrated for single atom imaging of ^{6}Li at low magnetic field, for the imaging of dilute and dense (Mott insulator) samples alike. However, EIT cooling has been found to be less reliable at high densities [136]. We therefore made the choice to implement Raman sideband cooling for the single-atom imaging in our experiment.

The principle of Raman sideband cooling can be shown in Fig. 6.6. In total, three laser beams are involved in the cooling cycle. Two laser beams with appropriate polarizations couple in a Raman transition the following states: $|g_1\rangle$ with vibrational quanta n, and state $|g_2\rangle$ with vibrational quanta $n-1$. By using a beam with a third frequency to repump the atoms, those in state $|g_2\rangle$ with the quanta $n-1$ can decay back into the state $|g_1\rangle$, with one quantum of vibration removed. In this process the atoms emit light but are also simultaneously cooled. The emitted photon during optical pumping is collected for fluorescence imaging.

An important criterion to know whether the cooling process is efficient is to compare the amount of energy taken away by one cooling cycle and the recoil energy given to the atom when emitting the fluorescence photon. The latter is simply given by $E_{\text{rec}} = \hbar^2 k^2/2m$ with k the wavevector of the scattered photon, and we have $E_{\text{rec}}/\hbar \sim 2\pi \times 70\,\text{kHz}$. The former is given by the energy difference between adjacent lattice bands, which can be approximated by the energy spacing of a harmonic oscillator for the lowest energy bands, and is given by $\hbar\omega_{\text{tr}}$, with ω_{tr} the

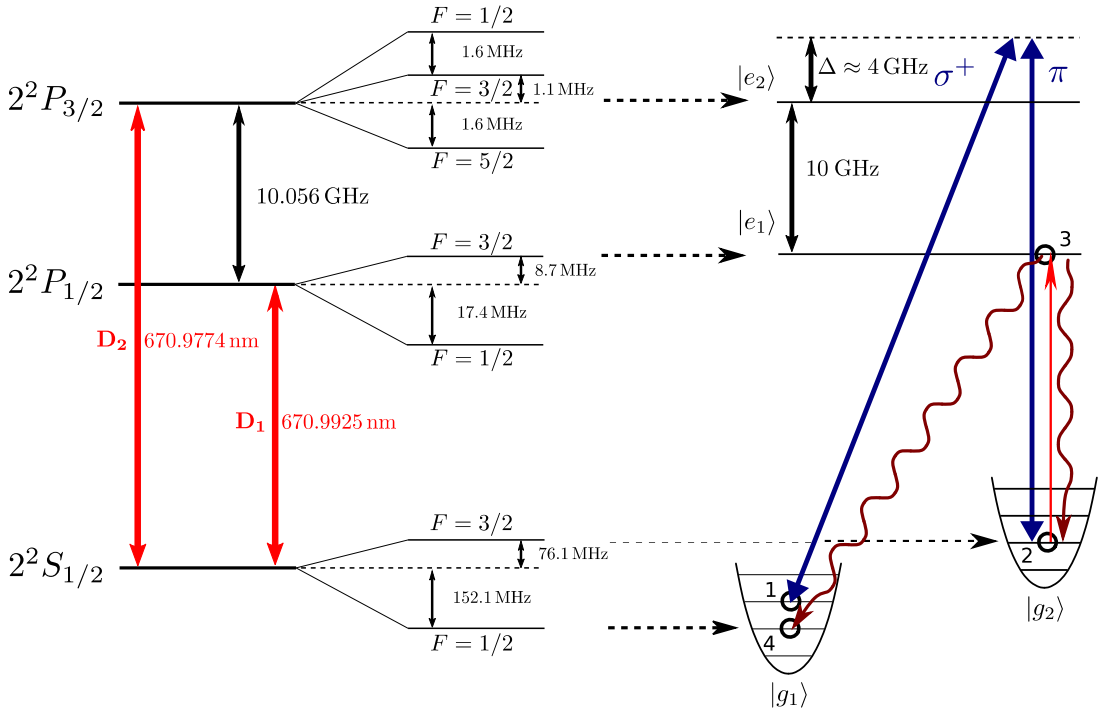

Figure 6.6: The principle of the Raman sideband cooling. The two Raman beams are denoted in blue. The repumper beams are denoted in red.

trapping frequency in a lattice well. For the available power $P = 35\,\mathrm{W}$ and a waist of $70\,\mu\mathrm{m}$, we can achieve an on-site trapping frequency of $\omega_{\mathrm{tr}} = 2\pi \times 1.74\,\mathrm{MHz}$.

A useful parameter is then the Lamb-Dicke parameter

$$\eta \equiv \sqrt{\frac{E_{\mathrm{rec}}}{\hbar\omega_{\mathrm{tr}}}},$$

which compares the two relevant energy scales, or, equivalently, the wavelength of the scattered photon with the extension of the atom wavefunction. In our case we expect a Lamb-Dicke parameter of approximately 0.21, which is the typical value for a fermionic quantum gas microscope [61, 62, 64].

6.3 Summary

In this last chapter we have presented how we plan to use a quantum gas microscope technique in our setup to access information at the single atom level. We have discussed several key points and presented our design choices to achieve this goal, for the pinning lattice, the high-resolution objective and the fluorescence imaging. The incorporation of these elements in the existing setup constitutes the next main experimental goal and should open up new horizons for the study of strongly interacting Fermi gases across the BEC-BCS crossover .

Chapter 7

Conclusion and perspectives

7.1 General conclusion

This thesis presents the design and characterization of a second generation quantum gas experiment dedicated to studying strongly interacting Fermi gases. In the course of the thesis, we have thoroughly described the experimental setup, presented the results of laser cooling on ^{6}Li atoms and the evaporative cooling in a hybrid magnetic-optic trap leading to the creation of a deeply degenerate unitary Fermi gas, well below the superfluid transition temperature.

In chapter 2 and 3, we described the experimental setup for the stage of laser cooling of ^{6}Li atoms. In particular, we presented the design and assembly procedure of the vacuum manifold and the red laser system, as well as other subsystems including the magnetic field generation and computer control of the experiment. Precise measurement of the atomic jet flux is given. Quantitative characterizations of a MOT and gray molasses of ^{6}Li are presented. In the end, we are able to very efficiently decrease the temperature of several 10^8 atoms from 550 °C to 50 μK in a duration of merely 2 s.

In chapter 4 we presented the setup of the high power infrared laser system for evaporatively cooling the ^{6}Li atoms to degeneracy. More specifically, we presented the optical transport dipole trap, capable of loading up to 7.5×10^6 atoms directly from the gray molasses and transporting with an efficiency of up to 80% into the science cell. Although in the dipole trap beam diameter is unexpectedly larger than we planned, we were able to cross this transport trap with another dipole beam and efficiently perform evaporative cooling in the science cell, by means of a well controlled RF sweep to balance the populations of the two spin states, at a magnetic field of 832 G, where lies the relevant Feshbach resonance for these two states. Characterization of the evaporation ramp, including the evolution of the temperature, the atom number and the phase space density at each stage of evaporation, was presented.

In order to characterize more precisely the temperature and more importantly, the degree of degeneracy of the obtained Fermi gas, in chapter 5, we applied a fit protocol based on the previous measurements on the equation of state of a unitary Fermi gas and extract the typical value of T/T_F at the center of the trap. This fit protocol serves as a thermometry in the near-degenerate as well as the degenerate regime. We are able to routinely produce a deeply degenerate Fermi gas of $T/T_\mathrm{F} \approx 0.06$, whose temperature is well below the superfluid transition

temperature. In the end, we showed a direct observation of the so called "superfluid plateau", by carefully choosing the spin imbalance of the two spin states, which reveals the superfluidity of the obtained sample.

In chapter 6 of this thesis, we described the design of the setup for achieving single-atom site-resolved imaging, to study strongly interacting Fermi gas. More specifically, we presented the setup of the pining lattice, the high resolution objective and the simulation of images with different magnification factors, and finally the Raman sideband cooling scheme for imaging and cooling ^{6}Li in an optical lattice.

7.2 Improvements on the current setup

The current experiment setup proves to be very stable on a daily basis. The total duration for producing a degenerate Fermi gas with $T/T_{\mathrm{F}} \approx 0.06$ is 16 s. This allows to have an excellent repetition rate.

During the whole sequence of 16 s, the longest steps in duration are listed in the following table:

Steps	**Duration**
MOT loading	1.5 - 2 s
Optical transport	1.2 s
Evaporation	11 s

Table 7.1: Duration for different steps of the experiment.

The most time-consuming process in the experiment is the evaporative cooling, which accounts for more than half of the total sequence duration. Compared to other experiments working with lithium, such an evaporation is particularly long. The reason for such a long duration of evaporation is two-fold.

On the one hand, the waist of the IPG beam is much larger than what we intended it to be. The increase of the waist not only negatively affects the loading in the MOT chamber from the D_1 gray molasses, but also sets a non-ideal starting point for evaporation. In particular, the collision rate decreases drastically with the size of the waist. Should the waist size be 60 μm as we expected, the collision rate at the beginning of the evaporation would possibly reach $10^3\,\mathrm{s}^{-1}$ and allow for much more efficient evaporative cooling (more details see Appendix C).

On the other hand, a fraction of the evaporation time ($\sim$4 s) is the result of switching from a crossed dipole trap to a single ALS trap, the reason for which is to have an elongated trap along one direction. The density distribution along this elongated direction gives a reliable density profile, suited for thermometry using an EoS fit and observation of superfluid plateau. Unfortunately, the switching operations decreases the collision rate and the phase space density as we reported in chapter 4, and sets back the evaporation progress. In the future, we plan to load a box potential directly from the crossed-dipole trap, in which case the evaporation is

performed solely in the crossed-dipole trap. The duration of the sequence is expected to be several seconds shorter.

Nevertheless, a possible improvement could be to modify the IPG setup to obtain the 60 μm beam waist size as initially planned. The gain in initial collision rate would significantly speed up the evaporation sequence.

7.3 Perspectives

In the following we discuss a series a measurements which could take place on our experiment in a near future.

Spatial dependence of correlations

As discussed in the introduction, very little is known about correlations in the BEC-BCS crossover. This lack of knowledge is especially stunning in the case of the unitary Fermi gas which is an emblematic case of strongly-correlated matter. In practice, no measurement to date allows to assess the degree or the nature of these correlations.

In that regard, the measurement of the EoS provided a first indication as it clearly deviates from mean-field theory. However, the EoS hardly represents a discriminant measure of how strongly-correlated in the system is. For instance, one could argue that the Bertsch parameter predicted by mean-field theories ($\xi_{\mathrm{MF}} = 0.59$) is on the same order of magnitude than the actual value $\xi = 0.37$.

Another important step in the characterization of correlations at unitarity are the recent measurements of the contact C as a function of temperature, through the normal-to-superfluid transition [54, 56]. While being extremely useful[(a)], this measurement only represents a minute segment of information when it comes to characterizing the correlated nature of the unitary gas. Firstly, the contact is only the short-range limit of the density-density correlation $g^{(2)}(r) = \langle n_\uparrow(0) n_\downarrow(r)\rangle$ and does not provide any information on the spatial variation of the latter. Secondly, the aforementioned measurements show that the two-body contact does not seem to be a sensitive probe of the overall correlations in the system. While the transition to the superfluid state is signaled by a sudden increase of C, the relative change between the high temperature value ($T \approx T_{\mathrm{F}}$) and the deep superfluid regime is only on the order of 30%. This suggests that higher order correlations are required to reach a comprehensive description of many-body effects in the unitary gas.

Our newly built experiment offers the possibility to tackle the paramount task of understanding the nature of many-body correlations in the unitary Fermi gas. Using spin-resolved single-atom imaging, we will be able to access a variety of spatial correlations beyond the short range behavior addressed so far, and furthermore, density correlation functions of arbitrary order. This series of measurement will open a new window on the characterization of the strongly correlated Fermi gases and provide a fundamentally new input for many-body theories.

[(a)] In particular, this work provides two insights: (i) settles the debate about the behavior of the two-body contact at the transition and (ii) sorts out the useful theories among the multiple predictions put forward in that context.

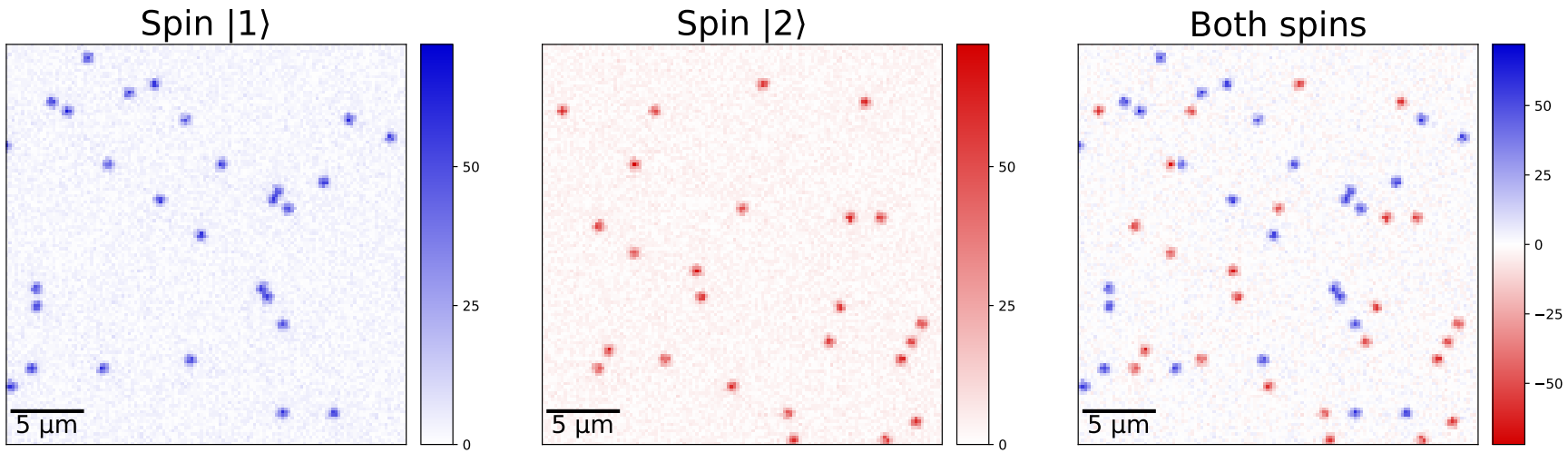

Figure 7.1: Single-atom spin-resolved detection of a dilute cloud (Simulation) [135, 137]. The quantum gas microscope is a powerful tool so far devoted to the study of lattice physics. We propose to apply it to homogeneous gases : after the cloud has been prepared in a given state of matter, we will pin the atoms in a deep optical lattice and expose them to near-resonant light. Shown are the distributions of atoms in both spin states expected for realistic experimental parameters (here, uncorrelated gas for simplicity). Each bright spot signals the presence of an atom with a fidelity >99%. Our simulations have shown that such a detection scheme is compatible with atomic densities targeted in the experiment.

Critical temperature and critical dynamics

As discussed in the introduction, the T_c-line of the balanced Fermi gas throughout the crossover is only known at unitarity [4, 5]. Everywhere else, theoretical predictions exist but rely on numerical methods with uncontrolled error bars.

The ability to measure T_c at unitarity is a direct consequence of universality, which relies on a clean thermodynamic analysis within the LDA framework. In the unitary case, the varying density imposed by the trap yields the tuning of a single parameter: T/T_F. Away from unitarity, T/T_F depends not only on the spatial position but also on the interaction parameter $1/(k_F a)$. This renders the methods used at ENS and MIT non-applicable (or at least introduces severe complications in the analysis).

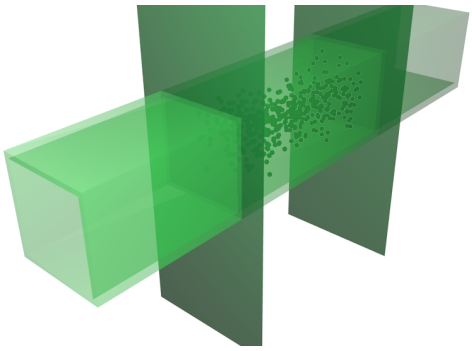

Figure 7.2: 3D render of a box potential. Most experiments performed with ultracold Fermi gases used inhomogeneous traps, typically harmonic potentials. While such potentials were proven to be extremely well suited for some thermodynamic studies, they constitute at the same time the main obstacle to quantitatively access other crucial observables. As a consequence of the trap inhomogeneities, any probe addressing the whole cloud yields a trap-averaged response. Using a box potential, we will first map precisely the T_c line throughout the BEC-BCS crossover. Second, we will measure critical exponents and check whether they agree with the ones of the 3D XY universality class, a common belief which has never been verified experimentally for a strongly correlated Fermi gas.

Here, we propose to use a box-potential to determine the T_c-line throughout the BEC-BCS crossover by measuring the onset of superfluid long-range order. The onset of long-range order is reflected in the momentum distribution $n_P(k)$ of fermion pairs as a sharp peak around $k = 0$. Our strategy to reveal the pair momentum distribution is to use the rapid-ramp technique, introduced at JILA [42] and then investigated further at MIT [41, 138]. The idea of this technique is to rapidly ramp the magnetic field to the BEC regime, and to measure the momentum distribution $n_m(k)$ of the produced tightly bound diatomic molecules. Formally, a model-independent theoretical understanding of the link between $n_P(k)$ and $n_m(k)$ is not available in the literature to date, but our colleague Félix Werner [139] has made important steps in this direction that will allow us to relate the two.

In addition, this will allow us to study the critical dynamics of the superfluid transition and measure the corresponding critical exponents η and ν. This transition is believed to belong to the 3D XY universality class, but this has never been verified experimentally for a strongly-correlated Fermi gas. The first exponent can be extracted from $n_P(k)$ at $T = T_c$, where one

expects

$$n_P(k) \underset{k\to 0}{\sim} \frac{1}{k^{2-\eta}} \tag{7.1}$$

with a critical exponent $\eta \approx 0.038$ for the 3D XY universality class. The second critical exponent can be extracted by varying the temperature around T_c, and measure the width w of $n_P(k)$, which is expected to vanish for $T \to T_\mathrm{c}$ as

$$w \sim 1/\xi \sim |T - T_\mathrm{c}|^\nu \tag{7.2}$$

with a critical exponent $\nu \approx 0.68$, where ξ stands for the correlation length associated with coherence between pairs.

These measurements will also allow us to determine the size of the critical region. One definition of the critical region is the temperature window around T_c where the correlation length ξ is large compared to the typical microscopic length-scale, which is set by the interparticle distance in the strongly correlated regime. An alternative definition of the critical region is the regime where the power-law in Eq. (7.2) holds.

Note that the use of a homogeneous potential is crucial for such studies, as one requires critical correlations and fluctuations to extend over the entire cloud. In conventional harmonic traps, the condition $T = T_\mathrm{c}$ can only be met on a two-dimensional surface within a three-dimensional cloud.

The challenge for these measurements is to perform reliable thermometry, due to the absence of spatial density variations in the trap. A way to solve this problem is to have one or two regions at the edges of the box with spatially varying potential to serve for thermometry, but from which the pairs would not be probed. Another longer term option would be to introduce a weakly interacting Bose gas of ^{7}Li in thermal equilibrium with the homogeneous Fermi gas to serve as a thermometer. In the case of a weakly interacting Bose gas, thermometry is readily accessible from time-of-flight density profiles.

Figure 7.3: Lab in April, 2016.

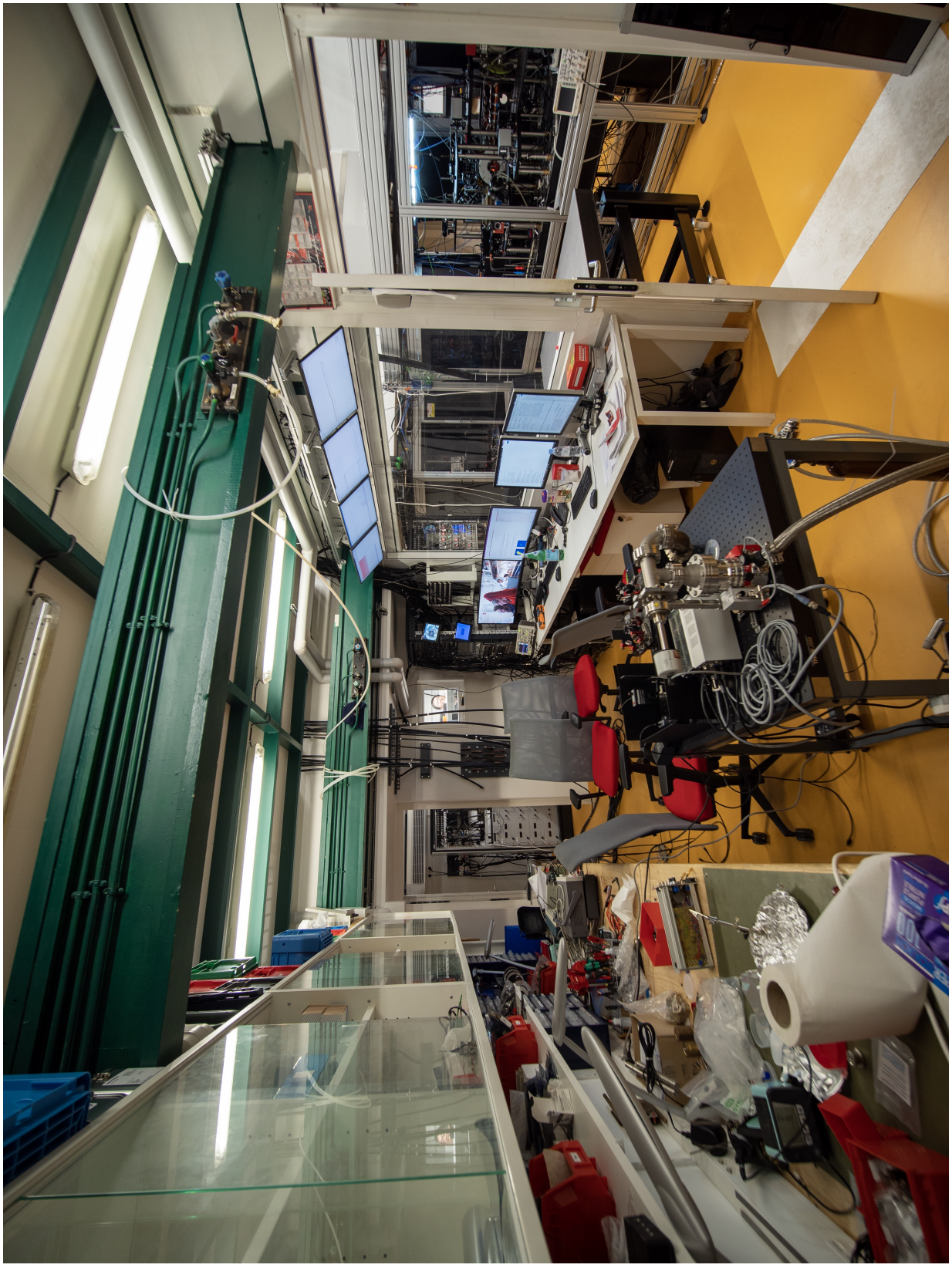

Figure 7.4: The control room. Picture taken in November, 2019 (Can you find the Easter egg in the picture?).

Figure 7.5: The main experiment room. Picture taken in November, 2019.

Figure 7.6: Laser table.

Appendix A

Fermi energy

The Fermi energy sets the characteristic energy scale for the system.

A.1 Homogeneous Fermi gases

Consider a homogeneous system of fixed volume V in d dimensions at temperature $T = 0$, the total atom number can be obtained by integrating over the momentum eigenstates that go up to the Fermi momentum k_{F}, which sets the limit between the occupied momentum states and unoccupied ones. In other words,

$$N = \int_0^{|\vec{k}| \leq k_{\mathrm{F}}} \mathrm{d}^d k \frac{V}{(2\pi)^d}. \tag{A.1}$$

Using the dispersion relation for free particles $E = \hbar^2 k^2/(2m)$, the above equation can be rewritten as an integral over energy up to E_{F}. This allows to obtain the relation between the Fermi energy and the atom number density $n \equiv N/V$ [140]

$$E_{\mathrm{F}} = \frac{\hbar^2}{2m} \times \begin{cases} (3\pi^2 n)^{2/3} & (d = 3) \\ (2\pi n) & (d = 2) \\ (\pi n)^2 & (d = 1) \end{cases} \tag{A.2}$$

This means that for a homogeneous system, the Fermi energy is directly related to the density of the system. Note that here n designates the density of two spin states with equal atom numbers. If n designates the density of a single component Fermi gas, the Fermi temperature, for example in 3D, is given by $E_{\mathrm{F}} = \hbar^2 (6\pi^2 n)^{2/3}/(2m)$.

A.2 Harmonically trapped Fermi gases

In more realistic experimental conditions, the gases are trapped not in a homogeneous box potential, but in an harmonic potential. In this particular case, the total number N can be obtained, like previously, as an integral over all energies up to the Fermi energy E_{F}, divided by

the number of states per energy interval [140]. In d dimensions,

$$N = \left(\prod_{i=1}^{d} \frac{1}{\hbar\omega_i}\right) \int_0^{E_\mathrm{F}} \mathrm{d}\epsilon_1 \int_0^{E_\mathrm{F}-\epsilon_1} \mathrm{d}\epsilon_2 \cdots \int_0^{E_\mathrm{F}-\sum_{j=1}^{d-1}\epsilon_j} \mathrm{d}\epsilon_d. \tag{A.3}$$

The Fermi energy and the particle number is then given by

$$E_\mathrm{F} = \hbar\overline{\omega}(d!N)^{1/d}, \tag{A.4}$$

where the geometric mean of the trap frequencies $\overline{\omega} \equiv (\prod_{i=1}^{d} \omega_i)^{1/d}$.

A.3 Energy scales

The most cited systems for comparison with the cold atom experiments are the metals and the neutron stars. The electrons in metals having a density of 10^{23} to $10^{24}\,\mathrm{cm}^{-3}$, the corresponding Fermi temperature is on the order of 10^4 K. The neutron density in a neutron star being as high as $10^{38}\,\mathrm{cm}^{-3}$, the Fermi Fermi temperature in this case mounts to 10^{11} K. This temperature is typically larger than the core temperature and several orders of magnitude higher than the surface temperature. As a result, for these systems, they are all deeply quantum degenerate.

The ultracold atomic samples we created in the lab are very difficult to compete in terms of quantum degeneracy with these aforementioned systems. The typical dilute deeply degenerate gases have a density of the order of $10^{12}\,\mathrm{cm}^{-3}$, the typical Fermi temperature in experimental conditions is on the order of μK. Up to date, experiments on ultracold Fermi gases can reach temperatures as low as several tens of nK, which is several percent of the Fermi temperature. Yet, these samples are still much less degenerate than the degenerate Fermi systems existing in nature.

The interest of studying ultracold Fermi gases lies in the interactions between particles that one can engineer. The onset of fermionic superfluidity for conventional superconductors, for example, occurs at several orders of magnitude lower than T_F, and makes the observation of superfluidity in such systems difficult. In contrast, the superfluid critical temperature in strongly interacting Fermi gases lies around $0.17\,T_\mathrm{F}$, and is accessible in practice. Indeed, superfluidity in such systems have been observed and has led to many interesting studies.

Appendix B

Tapered amplifier characterization

B.1 Tapered amplifiers

Tapered amplifiers (TAs) are diode lasers without the end facets that allows to amplify the laser power. It needs a seeding light, and it amplifies the light while preserving the polarization and seeding wavelength. For these properties, it is widely used in cold atom experiments for laser cooling.

In our experiments, we use two TA chips housed in a homemade mount. For TA chips operating around 671 nm, with a maximum seeding power 25 mW, the TA chip allows a maximum output power of 500 mW for a driving current of $800-900$ mA depending on the chip. This power is largely sufficient for laser cooling of Lithium. However, the spatial output mode is often less than optimal, so that the coupling efficiency for such output light may rarely exceed 40%. Nevertheless, the power available for the Zeeman and the MOT light are still enough and we in practice work in reduced current regime with a driving current of 600 mA to 700 mA. Since one of the known problems with these TA chips, when working at nominal driving current, is that they decrease in output power after years of use. The output power of the TAs is known to decrease from 500 mW to 300 mW.

B.2 Old tapered amplifiers

Tapered amplifiers can become dead or obsolete, if the output power is far below its nominal output. In this case, it needs to be replaced. However, it is not always obvious at which point an aging TA chip needs replacement. Since "dead" TA chips emit fluorescence light just as the normal one and does not necessarily decrease abruptly the output power much below the nominal output power.

In figure B.1 we show the output power curve as a function of the driving current for four different TA chips. We see that for a new TA chip, the dependence curve of power vs. current is continuous and monotonously increasing. Whereas for an aging TA chip, or a dead TA chip, the output power fluctuates when the driving current increases and at the maximum driving current, it cannot be able to output the nominal power.

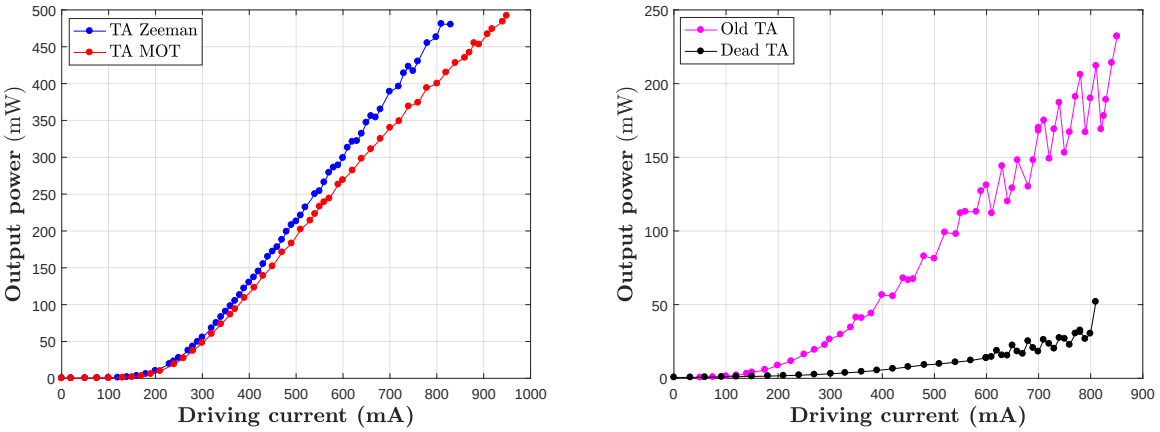

Figure B.1: Output power as a function of the driving current for TA chips. Left: Newly mounted TA chips used for providing the Zeeman slower light and the MOT light. Right: The same characteristics curve for an aging TA and a dead TA. Apart from the maximum output power, the power vs. current curve for an aged/ dead TA clearly shows clearly more fluctuations, unlike the curve for a new TA, the current is found to be monotonously increasing.

Thus one of the ways to identify if an TA chip is aging is to measure the power vs. current curve and see if there is such fluctuating behaviors on the output power.

Appendix C

Dependence of the collision rate on the waist size

The choice of the waist value for the transport trap is very important. On the one hand, this value determines the trap depth and hence the trap loading in the main chamber from the D_1 molasses. On the other hand, this waist value also determines the trapping frequencies and hence the collision rate once the atoms are in the science cell, which, as a result, affects the efficiency of evaporation.

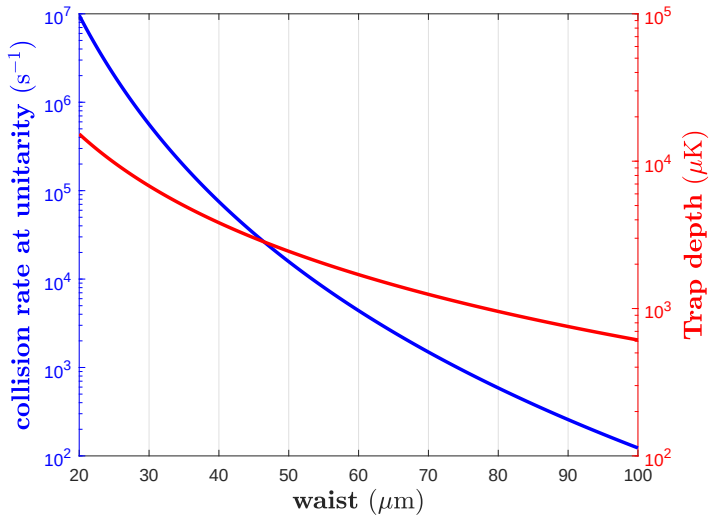

Figure C.1: The dependence of the trap depth (right axis) and the estimated collision rate before performing evaporation (left axis) with 5×10^6 atoms per spin state at temperature of $150\,\mu$K.

The collision rate at unitarity is given by the following expression [118]

$$\Gamma_{\text{coll}} = \frac{2N\hbar^2\overline{\omega}^3}{\pi(k_{\text{B}}T)^2}. \tag{C.1}$$

, where $\overline{\omega}$ is the geometric mean of the trapping frequencies, and in the case of a cylindrically symmetric trap $\overline{\omega} = (\omega_r^2\omega_z)^{1/3}$.

With expressions 4.3 and 4.4, we can express the collision rate as follows

$$\Gamma_{\text{coll}} = \frac{\sqrt{2}N\hbar^2\lambda_{\text{OT}}}{(\pi k_{\text{B}}T)^2}\left(\frac{4\beta}{m}\right)^{3/2}\frac{1}{w_0^7}, \tag{C.2}$$

where $\beta \equiv 6c^2\Gamma P/[(\omega^2-\omega_0^2)\omega_0^2]$.

The expression C.2 shows that the collision rate, for a given temperature T, atom number N and given optical power P is strongly dependent on the size of the waist to the power of seven.

In C.1 we plot the depth of the optical dipole trap as a function of the beam waist, as well as the estimated collision rate at unitarity before evaporation for a standard value of number of atoms loaded in the dipole trap (5×10^6) and for a typical the temperature after loading ($150\,\mu$K).

At the experimentally measured waist size of $88.7\,\mu$m, the collision rate is as we estimated in chapter 4, around $300\,\text{s}^{-1}$. Whereas if the waist were $60\,\mu$m, the collision rate, for the same atom number and the same temperature, will be around $4500\,\text{s}^{-1}$. In reality, when the waist changes, looking at expression C.2, only the atom number N, the cloud temperature T will change accordingly.

In practice, for a optical dipole trap with smaller waist, it is difficult to predict whether the atom number loaded in the dipole trap will decrease or increase, since the capture volume decreases whereas the trap also becomes deeper. But it is unlikely that the atom number varies as strongly as w_0^7. Temperature-wise however, since the trap is more tightly confined, it is probable that the atoms are hotter when loaded into a waist with smaller size.

In the end, the atom number in the trap might decrease, the temperature of the cloud in the trap is likely higher, but since the collision rate varies linearly to the atom number and is inversely proportional to the temperature, it is unlikely that the decrease of the waist size from $90\,\mu$m to $60\,\mu$m makes the ratio of N/T^2 vary as w_0^{-7}. In other words, the collision rate for decreasing the waist is likely to increase when decreasing waist from the current $90\,\mu$m to $60\,\mu$m.

Appendix D

Technical details for fitting the temperature using EoS fit

In order to be able to use the EoS fit to extract reliably the temperature and the degree of degeneracy of the cloud, many parameters related to the trap and the detection has to be characterized carefully.

Firstly, trap needs to be well characterized. The radial trapping frequencies can be deduced from the laser beam power and the measured waist, the axial trapping frequency, can only be well characterized by measuring the oscillation of the cloud in the axial direction.

Secondly, the imaging system needs to be reliable and well under control. In particular, the magnification needs to be well measured. The imaging light needs to be perfectly σ^+. And moreover, the cloud needs to be at focus so that there would not be any blurring on the border of the cloud.

We give more details in the following on how we address these issues.

D.1 Magnetic curvature measurement

The measurement of the magnetic trap frequency is performed by deliberately misalign the IPG from the center of the magnetic field center. By abruptly switching off the IPG beam, the atoms expand in the ALS beam and also oscillates in the ALS axial direction.

Precise measurement on the oscillation frequency can be extracted from the center-of mass position at different time. The measured frequency is the combined frequency of the magnetic trap and the axial trapping frequency of the ALS beam. We have measured with several different power values and oscillation amplitudes, the extracted magnetic trapping frequency all agree with each other and $f_{\mathrm{mag}} = 23.4 \pm 0.1\,\mathrm{Hz}$.

D.2 Magnification calibration

The magnification of the camera has also to be carefully calibrated. Since we are looking in the vertical direction, we cannot simply use the gravity to calibrate the free fall of a cold cloud.

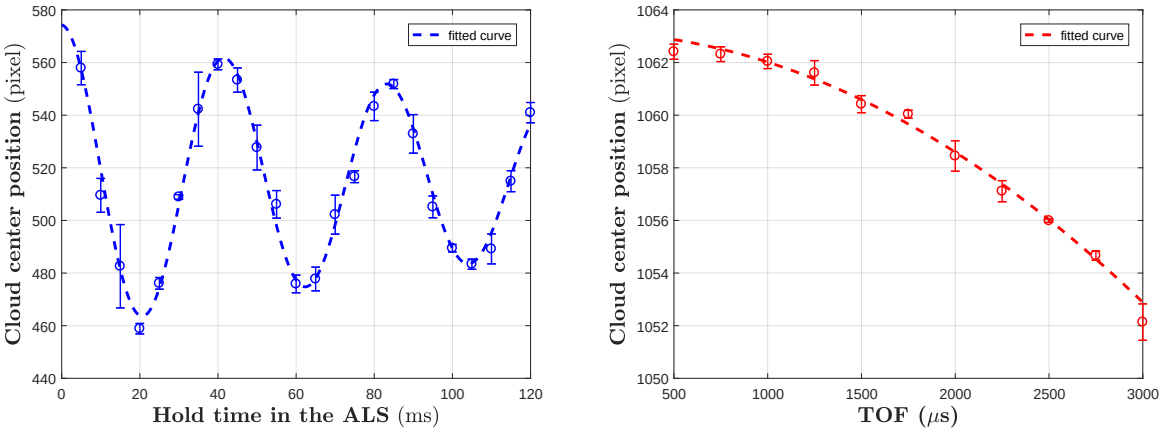

Figure D.1: Left: The center-of-mass oscillation of the cloud in the ALS beam of power $P_{\mathrm{ALS}} = 160\,\mathrm{mW}$. The axial trapping frequency due to the optical trap is then $f_{\mathrm{ALS}} = 5.0\,\mathrm{Hz}$. The measured oscillation frequency is $f_{\mathrm{osc}} = 24.0 \pm 0.1\,\mathrm{Hz}$. The magnetic trapping frequency is hence $f_{\mathrm{mag}} = \sqrt{(f_{\mathrm{osc}}^2 - f_{\mathrm{ALS}}^2)} = 23.4 \pm 0.1\,\mathrm{Hz}$. The damping is due to the fact that the amplitude of the oscillation is large and it begins to experience the non-harmonic part of the optical trap. Right: The calibration of the magnification using the free fall of a cloud in the vertical direction. The fitted curve gives a magnification of $M = 1.49 \pm 0.05$.

We have to calibrate the free fall of the cloud on another camera observing in the horizontal direction, then we move the ALS beam by a given quantity in the horizontal direction and we therefore deduce the magnification on this vertical camera.

The free fall measurement is performed with a cold cloud with temperature of roughly $500\,\mathrm{nK}$. The cloud is released at low field and we record the center position of the cloud as shown in figure D.1. The magnification on the horizontal camera is $M_{\mathrm{hor}} = 1.49 \pm 0.05$. The magnification on the camera looking in the vertical direction can be determined using the above method to be $M_{\mathrm{vert}} = 1.48 \pm 0.06$.

Such an error on the magnification allows us to have a relative error on T/T_{F} of less than 4%.

D.3 Global factor in the fit

In reality, the physical quantity we extract from the images is the optical density. In one dimension,

$$OD_{\mathrm{1D}} = \overline{n}_1 \times \frac{\sigma_0}{\Delta p}, \tag{D.1}$$

where $\overline{n}_1$ is the doubly integrated density profile, Δp the size of a pixel at the level of the atoms and σ_0 the on resonance cross section defined as

$$\sigma_0 = \frac{\hbar\omega\Gamma}{2I_{\mathrm{sat}}}, \tag{D.2}$$

since we have σ^+ light.

The quality of the σ^+ light is ensured by first a cube and then a quarterwaveplate before shooting on the atoms (no optical elements between the quarterwaveplate and the atoms). The positioning of the quarterwaveplate is optimized on the signal of the images taken through absorption.

The result D.1 is exact and in principal no further global factor is needed in the fit. However, should the light for some reason is not perfectly σ^+ and the cross section is somehow smaller than σ_0, we would then underestimate the atom number and hence have an error on the estimated T/T_{F}.

In order to check the consistency, we need to have a relatively low noise on the doubly integrated density profiles. In practice we average over 40 images with the same atom numbers and the final evaporation depth, we fit the averaged profile with the function introduced in chapter 5, with a global multiplicative factor κ, and we found this global factor $\kappa = 1.1 \pm 0.2$.

In practice, this factor cannot be larger than 1, the result, is consistent with the expected value $\kappa = 1$.

Bibliography

[1] A. Fert, *Nobel Lecture: Origin, development, and future of spintronics*, Reviews of Modern Physics **80** (2008), 4, 1517.

[2] P. A. Grünberg, *Nobel Lecture: From spin waves to giant magnetoresistance and beyond*, Reviews of Modern Physics **80** (2008), 4, 1531.

[3] I. Bloch, J. Dalibard and W. Zwerger, *Many-body physics with ultracold gases*, Reviews of Modern Physics **80** (2008), 3, 885.

[4] S. Nascimbène, N. Navon, K. J. Jiang, F. Chevy and C. Salomon, *Exploring the thermodynamics of a universal Fermi gas*, Nature **463** (2010), 7284, 1057.

[5] M. J. H. Ku, A. T. Sommer, L. W. Cheuk and M. W. Zwierlein, *Revealing the Superfluid Lambda Transition in the Universal Thermodynamics of a Unitary Fermi Gas*, Science **335** (2012), 6068, 563.

[6] W. Pauli, *Über den Zusammenhang des Abschlusses der Elektronengruppen im Atom mit der Komplexstruktur der Spektren*, Zeitschrift für Physik **31** (1925), 1, 765.

[7] H. Feshbach, *Unified theory of nuclear reactions*, Annals of Physics **5** (1958), 4, 357.

[8] H. Feshbach, *A unified theory of nuclear reactions. II*, Annals of Physics **19** (1962), 2, 287.

[9] J. Bardeen, L. N. Cooper and J. R. Schrieffer, *Theory of Superconductivity*, Physical Review **108** (1957), 5, 1175.

[10] L. N. Cooper, *Bound Electron Pairs in a Degenerate Fermi Gas*, Physical Review **104** (1956), 4, 1189.

[11] K. B. Davis, M. O. Mewes, M. R. Andrews, N. J. van Druten, D. S. Durfee, D. M. Kurn and W. Ketterle, *Bose-Einstein Condensation in a Gas of Sodium Atoms*, Physical Review Letters **75** (1995), 22, 3969.

[12] M. H. Anderson, J. R. Ensher, M. R. Matthews, C. E. Wieman and E. A. Cornell, *Observation of Bose-Einstein Condensation in a Dilute Atomic Vapor*, Science **269** (1995), 5221, 198.

[13] W. Zwerger (editor) *The BCS-BEC Crossover and the Unitary Fermi Gas*, Lecture Notes in Physics, Springer-Verlag, Berlin Heidelberg (2012).

[14] G. Bertsch, *in Proceedings of the Tenth International Conference on Recent Progress in Many-Body Theories*, World Scientific, Singapore (2000).

[15] G. A. Baker, *The mbx challenge competition: A neutron matter model*, International Journal of Modern Physics B **15** (2001), 10n11, 1314.

[16] F. Werner and Y. Castin, *Unitary gas in an isotropic harmonic trap: Symmetry properties and applications*, Physical Review A **74** (2006), 5, 053604.

[17] S. Tan, *Energetics of a strongly correlated Fermi gas*, Annals of Physics **323** (2008), 12, 2952.

[18] S. Tan, *Generalized virial theorem and pressure relation for a strongly correlated Fermi gas*, Annals of Physics **323** (2008), 12, 2987.

[19] B. Kiziltan, *Reassessing the Fundamentals: On the Evolution, Ages and Masses of Neutron Stars*, Universal-Publishers (2011).

[20] NASA, *NASA's Nuclear Spectroscopic Telescope Array: Illusions in the Cosmic Clouds*.

[21] B. S. Chandrasekhar, *A note on the maximum critical field of high-field superconductors*, Applied Physics Letters **1** (1962), 1, 7.

[22] A. M. Clogston, *Upper Limit for the Critical Field in Hard Superconductors*, Physical Review Letters **9** (1962), 6, 266.

[23] P. Fulde and R. A. Ferrell, *Superconductivity in a Strong Spin-Exchange Field*, Physical Review **135** (1964), 3A, A550.

[24] A. I. Larkin and Y. N. Ovchinnikov, *Nonuniform state of superconductors*, Zh.Eksp.Teor.Fiz. **47** (1964), 1136.

[25] W. Meissner and R. Ochsenfeld, *Ein neuer Effekt bei Eintritt der Supraleitfähigkeit*, Naturwissenschaften **21** (1933), 44, 787.

[26] C. Capan, A. Bianchi, R. Movshovich, A. D. Christianson, A. Malinowski, M. F. Hundley, A. Lacerda, P. G. Pagliuso and J. L. Sarrao, *Anisotropy of thermal conductivity and possible signature of the Fulde-Ferrell-Larkin-Ovchinnikov state in $CeCoIn_5$*, Physical Review B **70** (2004), 13, 134513.

[27] B. DeMarco and D. S. Jin, *Onset of Fermi Degeneracy in a Trapped Atomic Gas*, Science **285** (1999), 5434, 1703.

[28] U. Schneider, L. Hackermüller, S. Will, T. Best, I. Bloch, T. A. Costi, R. W. Helmes, D. Rasch and A. Rosch, *Metallic and Insulating Phases of Repulsively Interacting Fermions in a 3D Optical Lattice*, Science **322** (2008), 5907, 1520.

[29] R. Jördens, N. Strohmaier, K. Günter, H. Moritz and T. Esslinger, *A Mott insulator of fermionic atoms in an optical lattice*, Nature **455** (2008), 7210, 204.

[30] L. W. Cheuk, M. A. Nichols, K. R. Lawrence, M. Okan, H. Zhang and M. W. Zwierlein, *Observation of 2D Fermionic Mott Insulators of ^{40}K with Single-Site Resolution*, Physical Review Letters **116** (2016), 23, 235301.

[31] D. Greif, M. F. Parsons, A. Mazurenko, C. S. Chiu, S. Blatt, F. Huber, G. Ji and M. Greiner, *Site-resolved imaging of a fermionic Mott insulator*, Science **351** (2016), 6276, 953.

[32] A. Mazurenko, C. S. Chiu, G. Ji, M. F. Parsons, M. Kanász-Nagy, R. Schmidt, F. Grusdt, E. Demler, D. Greif and M. Greiner, *A cold-atom Fermi–Hubbard antiferromagnet*, Nature **545** (2017), 7655, 462.

[33] K. Dieckmann, C. A. Stan, S. Gupta, Z. Hadzibabic, C. H. Schunck and W. Ketterle, *Decay of an Ultracold Fermionic Lithium Gas near a Feshbach Resonance*, Physical Review Letters **89** (2002), 20, 203201.

[34] T. Loftus, C. A. Regal, C. Ticknor, J. L. Bohn and D. S. Jin, *Resonant Control of Elastic Collisions in an Optically Trapped Fermi Gas of Atoms*, Physical Review Letters **88** (2002), 17, 173201.

[35] K. M. O'Hara, S. L. Hemmer, S. R. Granade, M. E. Gehm, J. E. Thomas, V. Venturi, E. Tiesinga and C. J. Williams, *Measurement of the zero crossing in a Feshbach resonance of fermionic ^6Li*, Physical Review A **66** (2002), 4, 041401.

[36] S. Jochim, M. Bartenstein, G. Hendl, J. H. Denschlag, R. Grimm, A. Mosk and M. Weidemüller, *Magnetic Field Control of Elastic Scattering in a Cold Gas of Fermionic Lithium Atoms*, Physical Review Letters **89** (2002), 27, 273202.

[37] K. M. O'Hara, S. L. Hemmer, M. E. Gehm, S. R. Granade and J. E. Thomas, *Observation of a Strongly Interacting Degenerate Fermi Gas of Atoms*, Science **298** (2002), 5601, 2179.

[38] T. Bourdel, L. Khaykovich, J. Cubizolles, J. Zhang, F. Chevy, M. Teichmann, L. Tarruell, S. J. J. M. F. Kokkelmans and C. Salomon, *Experimental Study of the BEC-BCS Crossover Region in Lithium 6*, Physical Review Letters **93** (2004), 5, 050401.

[39] M. Greiner, C. A. Regal and D. S. Jin, *Emergence of a molecular Bose–Einstein condensate from a Fermi gas*, Nature **426** (2003), 6966, 537.

[40] M. Bartenstein, A. Altmeyer, S. Riedl, S. Jochim, C. Chin, J. H. Denschlag and R. Grimm, *Crossover from a Molecular Bose-Einstein Condensate to a Degenerate Fermi Gas*, Physical Review Letters **92** (2004), 12, 120401.

[41] M. W. Zwierlein, C. A. Stan, C. H. Schunck, S. M. F. Raupach, A. J. Kerman and W. Ketterle, *Condensation of Pairs of Fermionic Atoms near a Feshbach Resonance*, Physical Review Letters **92** (2004), 12, 120403.

[42] C. A. Regal, M. Greiner and D. S. Jin, *Observation of Resonance Condensation of Fermionic Atom Pairs*, Physical Review Letters **92** (2004), 4, 040403.

[43] J. Kinast, A. Turlapov, J. E. Thomas, Q. Chen, J. Stajic and K. Levin, *Heat Capacity of a Strongly Interacting Fermi Gas*, Science **307** (2005), 5713, 1296.

[44] J. Kinast, S. L. Hemmer, M. E. Gehm, A. Turlapov and J. E. Thomas, *Evidence for Superfluidity in a Resonantly Interacting Fermi Gas*, Physical Review Letters **92** (2004), 15, 150402.

[45] M. Bartenstein, A. Altmeyer, S. Riedl, S. Jochim, C. Chin, J. H. Denschlag and R. Grimm, *Collective Excitations of a Degenerate Gas at the BEC-BCS Crossover*, Physical Review Letters **92** (2004), 20, 203201.

[46] C. Chin, M. Bartenstein, A. Altmeyer, S. Riedl, S. Jochim, J. H. Denschlag and R. Grimm, *Observation of the Pairing Gap in a Strongly Interacting Fermi Gas*, Science **305** (2004), 5687, 1128.

[47] M. W. Zwierlein, J. R. Abo-Shaeer, A. Schirotzek, C. H. Schunck and W. Ketterle, *Vortices and superfluidity in a strongly interacting Fermi gas*, Nature **435** (2005), 7045, 1047.

[48] G. Valtolina, A. Burchianti, A. Amico, E. Neri, K. Xhani, J. A. Seman, A. Trombettoni, A. Smerzi, M. Zaccanti, M. Inguscio and G. Roati, *Josephson effect in fermionic superfluids across the BEC-BCS crossover*, Science **350** (2015), 6267, 1505.

[49] M. Horikoshi, S. Nakajima, M. Ueda and T. Mukaiyama, *Measurement of Universal Thermodynamic Functions for a Unitary Fermi Gas*, Science **327** (2010), 5964, 442.

[50] N. Navon, S. Nascimbène, F. Chevy and C. Salomon, *The Equation of State of a Low-Temperature Fermi Gas with Tunable Interactions*, Science **328** (2010), 5979, 729.

[51] S. Tan, *Large momentum part of a strongly correlated Fermi gas*, Annals of Physics **323** (2008), 12, 2971.

[52] J. T. Stewart, J. P. Gaebler, T. E. Drake and D. S. Jin, *Verification of Universal Relations in a Strongly Interacting Fermi Gas*, Physical Review Letters **104** (2010), 23, 235301.

[53] Y. Sagi, T. E. Drake, R. Paudel and D. S. Jin, *Measurement of the Homogeneous Contact of a Unitary Fermi Gas*, Physical Review Letters **109** (2012), 22, 220402.

[54] B. Mukherjee, P. B. Patel, Z. Yan, R. J. Fletcher, J. Struck and M. W. Zwierlein, *Spectral Response and Contact of the Unitary Fermi Gas*, Physical Review Letters **122** (2019), 20, 203402.

[55] E. D. Kuhnle, S. Hoinka, P. Dyke, H. Hu, P. Hannaford and C. J. Vale, *Temperature Dependence of the Universal Contact Parameter in a Unitary Fermi Gas*, Physical Review Letters **106** (2011), 17, 170402.

[56] C. Carcy, S. Hoinka, M. G. Lingham, P. Dyke, C. C. N. Kuhn, H. Hu and C. J. Vale, *Contact and Sum Rules in a Near-Uniform Fermi Gas at Unitarity*, Physical Review Letters **122** (2019), 20, 203401.

[57] S. Laurent, M. Pierce, M. Delehaye, T. Yefsah, F. Chevy and C. Salomon, *Connecting Few-Body Inelastic Decay to Quantum Correlations in a Many-Body System: A Weakly Coupled Impurity in a Resonant Fermi Gas*, Physical Review Letters **118** (2017), 10, 103403.

[58] W. S. Bakr, J. I. Gillen, A. Peng, S. Fölling and M. Greiner, *A quantum gas microscope for detecting single atoms in a Hubbard-regime optical lattice*, Nature **462** (2009), 7269, 74.

[59] J. F. Sherson, C. Weitenberg, M. Endres, M. Cheneau, I. Bloch and S. Kuhr, *Single-atom-resolved fluorescence imaging of an atomic Mott insulator*, Nature **467** (2010), 7311, 68.

[60] E. Haller, J. Hudson, A. Kelly, D. A. Cotta, B. Peaudecerf, G. D. Bruce and S. Kuhr, *Single-atom imaging of fermions in a quantum-gas microscope*, Nature Physics **11** (2015), 9, 738.

[61] L. W. Cheuk, M. A. Nichols, M. Okan, T. Gersdorf, V. V. Ramasesh, W. S. Bakr, T. Lompe and M. W. Zwierlein, *Quantum-Gas Microscope for Fermionic Atoms*, Physical Review Letters **114** (2015), 19, 193001.

[62] M. F. Parsons, F. Huber, A. Mazurenko, C. S. Chiu, W. Setiawan, K. Wooley-Brown, S. Blatt and M. Greiner, *Site-Resolved Imaging of Fermionic ^{6}Li in an Optical Lattice*, Physical Review Letters **114** (2015), 21, 213002.

[63] G. J. A. Edge, R. Anderson, D. Jervis, D. C. McKay, R. Day, S. Trotzky and J. H. Thywissen, *Imaging and addressing of individual fermionic atoms in an optical lattice*, Physical Review A **92** (2015), 6, 063406.

[64] A. Omran, M. Boll, T. A. Hilker, K. Kleinlein, G. Salomon, I. Bloch and C. Gross, *Microscopic Observation of Pauli Blocking in Degenerate Fermionic Lattice Gases*, Physical Review Letters **115** (2015), 26, 263001.

[65] A. L. Gaunt, T. F. Schmidutz, I. Gotlibovych, R. P. Smith and Z. Hadzibabic, *Bose-Einstein Condensation of Atoms in a Uniform Potential*, Physical Review Letters **110** (2013), 20, 200406.

[66] L. Chomaz, L. Corman, T. Bienaimé, R. Desbuquois, C. Weitenberg, S. Nascimbène, J. Beugnon and J. Dalibard, *Emergence of coherence via transverse condensation in a uniform quasi-two-dimensional Bose gas*, Nature Communications **6** (2015), 1, 1.

[67] B. Mukherjee, Z. Yan, P. B. Patel, Z. Hadzibabic, T. Yefsah, J. Struck and M. W. Zwierlein, *Homogeneous Atomic Fermi Gases*, Physical Review Letters **118** (2017), 12, 123401.

[68] K. Hueck, N. Luick, L. Sobirey, J. Siegl, T. Lompe and H. Moritz, *Two-Dimensional Homogeneous Fermi Gases*, Physical Review Letters **120** (2018), 6, 060402.

[69] T. Fukuhara, A. Kantian, M. Endres, M. Cheneau, P. Schauß, S. Hild, D. Bellem, U. Schollwöck, T. Giamarchi, C. Gross, I. Bloch and S. Kuhr, *Quantum dynamics of a mobile spin impurity*, Nature Physics **9** (2013), 4, 235.

[70] S. Hild, T. Fukuhara, P. Schauß, J. Zeiher, M. Knap, E. Demler, I. Bloch and C. Gross, *Far-from-Equilibrium Spin Transport in Heisenberg Quantum Magnets*, Physical Review Letters **113** (2014), 14, 147205.

[71] P. M. Preiss, R. Ma, M. E. Tai, A. Lukin, M. Rispoli, P. Zupancic, Y. Lahini, R. Islam and M. Greiner, *Strongly correlated quantum walks in optical lattices*, Science **347** (2015), 6227, 1229.

[72] T. Fukuhara, P. Schauß, M. Endres, S. Hild, M. Cheneau, I. Bloch and C. Gross, *Microscopic observation of magnon bound states and their dynamics*, Nature **502** (2013), 7469, 76.

[73] J. Simon, W. S. Bakr, R. Ma, M. E. Tai, P. M. Preiss and M. Greiner, *Quantum simulation of antiferromagnetic spin chains in an optical lattice*, Nature **472** (2011), 7343, 307.

[74] P. Schauß, M. Cheneau, M. Endres, T. Fukuhara, S. Hild, A. Omran, T. Pohl, C. Gross, S. Kuhr and I. Bloch, *Observation of spatially ordered structures in a two-dimensional Rydberg gas*, Nature **491** (2012), 7422, 87.

[75] P. Schauß, J. Zeiher, T. Fukuhara, S. Hild, M. Cheneau, T. Macrì, T. Pohl, I. Bloch and C. Gross, *Crystallization in Ising quantum magnets*, Science **347** (2015), 6229, 1455.

[76] J. Zeiher, P. Schauß, S. Hild, T. Macrì, I. Bloch and C. Gross, *Microscopic Characterization of Scalable Coherent Rydberg Superatoms*, Physical Review X **5** (2015), 3, 031015.

[77] T. Fukuhara, S. Hild, J. Zeiher, P. Schauß, I. Bloch, M. Endres and C. Gross, *Spatially Resolved Detection of a Spin-Entanglement Wave in a Bose-Hubbard Chain*, Physical Review Letters **115** (2015), 3, 035302.

[78] R. Islam, R. Ma, P. M. Preiss, M. Eric Tai, A. Lukin, M. Rispoli and M. Greiner, *Measuring entanglement entropy in a quantum many-body system*, Nature **528** (2015), 7580, 77.

[79] M. Boll, T. A. Hilker, G. Salomon, A. Omran, J. Nespolo, L. Pollet, I. Bloch and C. Gross, *Spin- and density-resolved microscopy of antiferromagnetic correlations in Fermi-Hubbard chains*, Science **353** (2016), 6305, 1257.

[80] T. A. Hilker, G. Salomon, F. Grusdt, A. Omran, M. Boll, E. Demler, I. Bloch and C. Gross, *Revealing hidden antiferromagnetic correlations in doped Hubbard chains via string correlators*, Science **357** (2017), 6350, 484.

[81] G. Salomon, J. Koepsell, J. Vijayan, T. A. Hilker, J. Nespolo, L. Pollet, I. Bloch and C. Gross, *Direct observation of incommensurate magnetism in Hubbard chains*, Nature **565** (2019), 7737, 56.

[82] A. Lukin, M. Rispoli, R. Schittko, M. E. Tai, A. M. Kaufman, S. Choi, V. Khemani, J. Léonard and M. Greiner, *Probing entanglement in a many-body–localized system*, Science **364** (2019), 6437, 256.

[83] P. T. Brown, D. Mitra, E. Guardado-Sanchez, P. Schauß, S. S. Kondov, E. Khatami, T. Paiva, N. Trivedi, D. A. Huse and W. S. Bakr, *Spin-imbalance in a 2D Fermi-Hubbard system*, Science **357** (2017), 6358, 1385.

[84] D. Mitra, P. T. Brown, E. Guardado-Sanchez, S. S. Kondov, T. Devakul, D. A. Huse, P. Schauß and W. S. Bakr, *Quantum gas microscopy of an attractive Fermi–Hubbard system*, Nature Physics **14** (2018), 2, 173.

[85] P. T. Brown, D. Mitra, E. Guardado-Sanchez, R. Nourafkan, A. Reymbaut, C.-D. Hébert, S. Bergeron, A.-M. S. Tremblay, J. Kokalj, D. A. Huse, P. Schauß and W. S. Bakr, *Bad metallic transport in a cold atom Fermi-Hubbard system*, Science **363** (2019), 6425, 379.

[86] M. E. Gehm, *Properties of ^{6}Li* (2003).

[87] L. Tarruell, *Superfluidité dans un gaz de fermions ultrafroids*, Ph.D. thesis, Université Pierre et Marie Curie (2008).

[88] T. Salez, *Towards quantum degenerate atomic Fermi mixtures*, Ph.D. thesis, Université Pierre et Marie Curie (2011).

[89] C. Weitenberg, *Private communication*.

[90] U. Eismann, A. Bergschneider, F. Sievers, N. Kretzschmar, C. Salomon and F. Chevy, *2.1-watts intracavity-frequency-doubled all-solid-state light source at 671 nm for laser cooling of lithium*, Optics Express **21** (2013), 7, 9091.

[91] N. Kretzschmar, *Experiments with Ultracold Fermi Gases : Quantum Degeneracy of Potassium-40 and All-solid-state Laser Sources for Lithium*, Ph.D. thesis, École Normale Supérieure (2015).

[92] F. Sievers, N. Kretzschmar, D. R. Fernandes, D. Suchet, M. Rabinovic, S. Wu, C. V. Parker, L. Khaykovich, C. Salomon and F. Chevy, *Simultaneous sub-Doppler laser cooling of fermionic ^{6}Li and ^{40}K on the D_1 line: Theory and experiment*, Physical Review A **91** (2015), 2, 023426.

[93] D. Kunlun, *Laser frequency offset lock for Raman sideband cooling and site-resolved imaging of Li6 atoms in a pinning lattice*, Master thesis, École Polytechnique Fédérale de Lausanne (2018).

[94] D. J. McCarron, S. A. King and S. L. Cornish, *Modulation transfer spectroscopy in atomic rubidium*, Measurement Science and Technology **19** (2008), 10, 105601.

[95] W. D. Phillips and H. Metcalf, *Laser Deceleration of an Atomic Beam*, Physical Review Letters **48** (1982), 9, 596.

[96] A. G. Truscott, K. E. Strecker, W. I. McAlexander, G. B. Partridge and R. G. Hulet, *Observation of Fermi Pressure in a Gas of Trapped Atoms*, Science **291** (2001), 5513, 2570.

[97] F. Schreck, L. Khaykovich, K. L. Corwin, G. Ferrari, T. Bourdel, J. Cubizolles and C. Salomon, *Quasipure Bose-Einstein Condensate Immersed in a Fermi Sea*, Physical Review Letters **87** (2001), 8, 080403.

[98] Z. Hadzibabic, C. A. Stan, K. Dieckmann, S. Gupta, M. W. Zwierlein, A. Görlitz and W. Ketterle, *Two-Species Mixture of Quantum Degenerate Bose and Fermi Gases*, Physical Review Letters **88** (2002), 16, 160401.

[99] S. Jochim, M. Bartenstein, A. Altmeyer, G. Hendl, S. Riedl, C. Chin, J. H. Denschlag and R. Grimm, *Bose-Einstein Condensation of Molecules*, Science **302** (2003), 5653, 2101.

[100] A. Mosk, S. Jochim, H. Moritz, T. Elsässer, M. Weidemüller and R. Grimm, *Resonator-enhanced optical dipole trap for fermionic lithium atoms*, Optics Letters **26** (2001), 23, 1837.

[101] A. Keshet, *A next-generation apparatus for lithium optical lattice experiments*, Ph.D. thesis, Massachusetts Institute of Technology (2012).

[102] M. Rabinovic, *Quasithermalization of fermions in a quadrupole potential and evaporative cooling of ^{40}K to quantum degeneracy*, Ph.D. thesis, École Normale Supérieure (2017).

[103] G. Ferrari, *Piégeage simultané des isotopes fermionique et bosonique du lithium, étude théorique de la relaxation collisionelle dans un gaz de Fermi dégénéré*, Ph.D. thesis, Université Pierre et Marie Curie (2000).

[104] D. R. Fernandes, F. Sievers, N. Kretzschmar, S. Wu, C. Salomon and F. Chevy, *Sub-Doppler Laser Cooling of Fermionic ^{40}K Atoms in Three-Dimensional Gray Optical Molasses*, EPL (Europhysics Letters) **100** (2012), 6, 63001.

[105] A. T. Grier, I. Ferrier-Barbut, B. S. Rem, M. Delehaye, L. Khaykovich, F. Chevy and C. Salomon, *Λ-enhanced sub-Doppler cooling of lithium atoms in D_1 gray molasses*, Physical Review A **87** (2013), 6, 063411.

[106] G. Salomon, L. Fouché, P. Wang, A. Aspect, P. Bouyer and T. Bourdel, *Gray-molasses cooling of ^{39}K to a high phase-space density*, EPL (Europhysics Letters) **104** (2013), 6, 63002.

[107] G. Valtolina, *Superfluid and spin dynamics of strongly interacting atomic Fermi gases*, Ph.D. thesis, Scuola Normale Superiore di Pisa (2016).

[108] G. Colzi, *A new apparatus to simulate fundamental interactions with ultracold atoms*, Ph.D. thesis, University of Trento (2018).

[109] D. R. Fernandes, *Trapping and cooling of fermionic alkali atoms to quantum degeneracy. Sub-Doppler cooling of Potassium-40 and Lithium-6 in gray molasses*, Ph.D. thesis, Université Pierre et Marie Curie (2014).

[110] F. Sievers, *Ultracold Fermi mixtures and simultaneous sub-Doppler laser cooling of fermionic ^{6}Li and ^{40}K*, Ph.D. thesis, Université Pierre et Marie Curie (2014).

[111] A. Burchianti, G. Valtolina, J. A. Seman, E. Pace, M. De Pas, M. Inguscio, M. Zaccanti and G. Roati, *Efficient all-optical production of large ^{6}Li quantum gases using D_1 gray-molasses cooling*, Physical Review A **90** (2014), 4, 043408.

[112] R. Grimm, M. Weidemüller and Y. B. Ovchinnikov, *Optical Dipole Traps for Neutral Atoms*, Advances In Atomic, Molecular, and Optical Physics **42** (2000), 95.

[113] D. Dreon, *Designing and building an ultracold Dysprosium experiment : A new framework for light-spin interaction*, Ph.D. thesis, École Normale Supérieure (2017).

[114] T. A. Savard, K. M. O'Hara and J. E. Thomas, *Laser-noise-induced heating in far-off resonance optical traps*, Physical Review A **56** (1997), 2, R1095.

[115] S. Stringari, *Dynamics of Bose-Einstein condensed gases in highly deformed traps*, Physical Review A **58** (1998), 3, 2385.

[116] L. D. Landau, *Zur Theorie der Energieübertragung. II*, Physikalische Zeitschrift der Sowjetunion **2** (1932), 46.

[117] C. Zener and R. H. Fowler, *Non-adiabatic crossing of energy levels*, Proceedings of the Royal Society of London. Series A, Containing Papers of a Mathematical and Physical Character **137** (1932), 833, 696.

[118] M. E. Gehm, S. L. Hemmer, K. M. O'Hara and J. E. Thomas, *Unitarity-limited elastic collision rate in a harmonically trapped Fermi gas*, Physical Review A **68** (2003), 1, 011603.

[119] S. Nascimbène, *Thermodynamics of ultracold Fermi gases*, Ph.D. thesis, Université Pierre et Marie Curie (2010).

[120] E. Beth and G. E. Uhlenbeck, *The quantum theory of the non-ideal gas. II. Behaviour at low temperatures*, Physica **4** (1937), 10, 915.

[121] X.-J. Liu, H. Hu and P. D. Drummond, *Virial Expansion for a Strongly Correlated Fermi Gas*, Physical Review Letters **102** (2009), 16, 160401.

[122] A. Bulgac, J. E. Drut and P. Magierski, *Spin 1/2 Fermions in the Unitary Regime: A Superfluid of a New Type*, Physical Review Letters **96** (2006), 9, 090404.

[123] M. W. Zwierlein, C. A. Stan, C. H. Schunck, S. M. F. Raupach, S. Gupta, Z. Hadzibabic and W. Ketterle, *Observation of Bose-Einstein Condensation of Molecules*, Physical Review Letters **91** (2003), 25, 250401.

[124] G. B. Partridge, W. Li, R. I. Kamar, Y.-a. Liao and R. G. Hulet, *Pairing and Phase Separation in a Polarized Fermi Gas*, Science **311** (2006), 5760, 503.

[125] W. Ketterle and M. W. Zwierlein, *Making, probing and understanding ultracold Fermi gases*, La Rivista del Nuovo Cimento **31** (2008), 506, 247.

[126] I. Ferrier-Barbut, *Mixtures of Bose and Fermi Superfluids*, Ph.D. thesis, École Normale Supérieure (2014).

[127] M. W. Zwierlein, A. Schirotzek, C. H. Schunck and W. Ketterle, *Fermionic Superfluidity with Imbalanced Spin Populations*, Science **311** (2006), 5760, 492.

[128] M. Cheneau, P. Barmettler, D. Poletti, M. Endres, P. Schauß, T. Fukuhara, C. Gross, I. Bloch, C. Kollath and S. Kuhr, *Light-cone-like spreading of correlations in a quantum many-body system*, Nature **481** (2012), 7382, 484.

[129] J.-y. Choi, S. Hild, J. Zeiher, P. Schauß, A. Rubio-Abadal, T. Yefsah, V. Khemani, D. A. Huse, I. Bloch and C. Gross, *Exploring the many-body localization transition in two dimensions*, Science **352** (2016), 6293, 1547.

[130] L. W. Cheuk, M. A. Nichols, K. R. Lawrence, M. Okan, H. Zhang, E. Khatami, N. Trivedi, T. Paiva, M. Rigol and M. W. Zwierlein, *Observation of spatial charge and spin correlations in the 2D Fermi-Hubbard model*, Science **353** (2016), 6305, 1260.

[131] M. Miranda, R. Inoue, Y. Okuyama, A. Nakamoto and M. Kozuma, *Site-resolved imaging of ytterbium atoms in a two-dimensional optical lattice*, Physical Review A **91** (2015), 6, 063414.

[132] Y. H. Kiefer, *Pinning Lattice for Single Site Imaging of Ultracold Lithium Atoms*, Masterarbeit, University of Hamburg (2018).

[133] B. Peaudecerf, M. Andia, M. Brown, E. Haller and S. Kuhr, *Microwave preparation of two-dimensional fermionic spin mixtures*, New Journal of Physics **21** (2019), 1, 013020.

[134] A. Fuhrmanek, R. Bourgain, Y. R. P. Sortais and A. Browaeys, *Light-assisted collisions between a few cold atoms in a microscopic dipole trap*, Physical Review A **85** (2012), 6, 062708.

[135] J. Verstraten, *Developing Single-Atom Imaging of the Unitary Fermi Gas in an Optical Lattice*, Internship report, École Normale Supérieure (2019).

[136] B. Peaudecerf, *Private communication*.

[137] J. Verstraten, *Private communication*.

[138] M. W. Zwierlein, C. H. Schunck, C. A. Stan, S. M. F. Raupach and W. Ketterle, *Formation Dynamics of a Fermion Pair Condensate*, Physical Review Letters **94** (2005), 18, 180401.

[139] F. Werner, *Private communication*.

[140] N. W. Ashcroft and N. Mermin, *Solid State Physics*, Brooks/Cole, New York, new edition (1976).

Danksagung

Die Durchführung dieser Doktorarbeit und aller damit verbundenen Projekte wäre ohne die tatkräftige Unterstützung vieler aktiver, hilfsbereiter und leidenschaftlicher Mitmenschen überhaupt nicht vorstellbar gewesen. Ich schätze mich sehr glücklich Teil einer Arbeitsgruppe gewesen zu sein, innerhalb derer nicht nur fachliches Wissen, sondern auch viel Zwischenmenschlichkeit zum Tragen kam. Hiermit möchte ich mich bei den folgenden Personen namentlich bedanken:

An erster Stelle möchte ich meinem Doktorvater Dr. Christophe Salomon danken, der mich mit der Ausgestaltung und Umsetzung eines neuen Experiments zu einem solch komplexen und herausfordernden Themas betraut hat. Er hat mir bei dieser Arbeit sehr viele Freiheiten eingeräumt und mir großes Vertrauen entgegengebracht, sowie mir gezeigt meiner physikalischen Intuition zu folgen, um die täglichen Probleme im Labor zu lösen; Mein Dank gilt auch Prof. Dr. Frédéric Chevy, der mich von Beginn an als Co-Doktorvater betreut hat. Ich bin ihnen sehr dankbar, mir die Realisierung der vorliegenden Doktorarbeit ermöglicht zu haben.

Auch bei den Mitgliedern der Prüfungskommission möchte ich mich bedanken, für ihre Zeit und Mühen, die sie in meine Doktorarbeit investiert haben: Prof. Dr. Stefan Kuhr und Dr. Giacomo Roati als Gutachtern, Dr. Leticia Tarruell und Prof. Dr. Bruno Laburthe-Tolra als Prüfern.

Ein besonderer Dank gilt unserem Teamleiter Tarik Yefsah, der sich außerordentlich für das Experiment eingesetzt hat. Ohne seine effiziente Organisation und tägliche Unterstützung an allen physikalischen und technischen Details des Experiments wären der Fortschritt sicherlich viel langsamer vonstattengegangen.

Außerdem möchte ich natürlich dem gesamten Team meinen Dank aussprechen. Hierbei möchte ich vor allem Bruno Peaudecerf, Julian Struck und Jean-Michel Rabinovic[(a)] nennen: Obwohl Bruno erst während des letzten Jahres meiner Arbeit unsere Gruppe verstärkt hat, hat er sich sehr schnell mit dem Experiment vertraut gemacht und hat sich daraufhin u.a. um den Großteil der Datenanalyse gekümmert. Ohne Brunos Hilfe hätte sich meine Promotionsdauer sicherlich signifikant verlängert; Julian hat im ersten Jahr seiner Zeit in der Gruppe am Aufbau des Experiments mitgearbeitet und u.a. die Transport-Dipolfalle entwickelt. Während dieser Zeit hat er unzählige wertvolle und hilfreiche Vorschläge eingebracht, von denen ich viel lernen konnte. Insbesondere bin ich stets beeindruckt von Julians tiefen Verständnis in zahlreichen physikalischen sowie technischen Bereichen der Atomphysik. Zudem verfügt er über die bemerkenswerte Fähigkeit, immer eine praktische und realisierbare Lösung für bestimmte

[(a)] auch bekannt als Mihail Rabinovic.

Problem in kurzer Zeit zu finden; Jean-Michel hat nach seiner eigenen Doktorarbeit am "Fermix" Experiment für ein paar Monaten in unserem Labor als Postdoc gearbeitet. Seine Elektronik-Fachkenntnisse, insbesondere die Entwicklung der Optokoppler-Karten, hat uns sehr geholfen. Zusätzlich habe ich seine spezielle Art des schwarzen Humors sehr genossen.

Meinen Mitdoktoranden, Kunlun Dai und Joris Verstraten danke ich ebenfalls für eine kurze, aber sehr fruchtbare Zusammenarbeit. Obwohl sich beide erst am Ende meiner Doktorarbeit unserer Gruppe angeschlossen haben, freue ich mich sehr, dass sie das Experiment während des Zusammenschreibens meiner Doktorarbeit übernommen haben und ich wünsche ihnen alles Gute für das künftige Vorankommen.

Allen Mitgliedern von "Lithium" und "Fermix", insbesondere Sébastien Laurent, Matthieu Pierce und Gentle Dash, sowie Thomas Reimann, Cédric Enesa, Markus Bohlen, Clément de Daniloff und Marin Tarrault, sei für das freundschaftliche Klima und die geistreichen Diskussionen ausdrücklich gedankt. Insbesondere blicke ich gerne auf die zahllosen gemeinsamen Burger-Nächte im Pub O'Prince zurück, die mich im Laufe der Jahre von einem Quartalssäufer zu einem echten Alkoholiker gemacht haben.

Für das gewissenhafte Korrekturlesen meiner Doktorarbeit und für zusätzliche Anmerkungen zum Text und Abbildungen danke ich Tarik, Bruno und Julian.

Dem Technischen Personal und dem Verwaltungspersonal bin ich für die Unterstützung bei vielen verschiedenen Aspekten sehr dankbar. Dabei möchte ich die folgenden Menschen besonders hervorheben: Didier Courtiade, Catherine Gripe und Célia Ruschinzik für die Renovierung unserer Laborräume und die Einrichtung unzähliger Anlagen. Toufik el Atmani und Lionel Pérennès für die hervorragenden Elektronikkarten und für die Unterhaltung verschiedener Geräte; Jean-Michel Isac, Arnaud Leclercq, Nabil Garroum, Mathieu Sardin und die anderen Mechanikern für die zahllosen Spezialanfertigungen mechanischer Bauteile; Thierry Tardieu, Stéphanie Dubois und Audrey Gohlke für die Unterstützung bei unendlichen administrativen Dingen.

Mehr als anderen gilt mein Dank meiner Eltern für ihre bedingungslose Unterstützung, stetes Verständnis und unvergleichbare Geduld, ungeachtet meiner jahrelangen Abwesenheit. Der Dank dafür kann niemals im Wort gefasst werden.

ABSTRACT

This thesis reports on the construction of a new generation quantum gas experiment aiming to study strongly interacting Fermi gases of ^{6}Li. A detailed description of the design and implementation, as well as characterization of the apparatus is presented. We have realized a large magneto-optical trap of ^{6}Li followed by a gray molasses, to efficiently cool the atoms to sub-Doppler temperatures, which yield excellent starting conditions for loading into an optical dipole trap. An optical transport with high efficiency as well as evaporative cooling at unitarity leads to the production of an ultracold Fermi gas of ^{6}Li in a total sequence duration of 16 s.
Combined with the utilization of single-atom imaging and tailored potentials, this newly built machine paves the way towards novel experiments on ultracold Fermi gases, such as the measurement of spin-dependent correlation functions or the quest for exotic spin-imbalanced superfluid phases.

KEYWORDS

Ultracold Gases – Strongly Interacting Fermions – Superfluidity – Single Atom Imaging

RÉSUMÉ

Cette thèse expose la construction d'une expérience de gaz quantiques de nouvelle génération, ayant pour objectif d'étudier les gaz de Fermi de ^{6}Li en interaction forte. Une description détaillée du design et de la mise en œuvre, ainsi que la caractérisation du montage sont présentées. Nous avons réalisé un grand piège magnéto-optique de ^{6}Li, suivi par une mélasse grise, afin de refroidir efficacement les atomes à des températures sub-Doppler, ce qui constitue un excellent point de départ pour le chargement dans un piège dipolaire optique. Un transport optique avec une haute efficacité conjointement à un refroidissement évaporatif à l'unitarité permet la production d'un gaz de Fermi ultrafroid de ^{6}Li à la fin d'une séquence d'une durée totale de 16 s.
Combinée avec l'utilisation de l'imagerie à atome unique et de potentiels sur-mesure, cette nouvelle machine ouvre la voie à des expériences nouvelles sur les gaz de Fermi ultrafroids, comme par exemple la mesure des fonctions de corrélation dépendant du spin, ou la recherche des phases exotiques de superfluides à déséquilibre de spin.

MOTS CLÉS

Gaz Ultrafroids – Fermions en Interaction Forte – Superfluidité – Imagerie à Atome Unique